Technological Improvements for Linear Ion Trap Experiments

by

Brendin Thomas Chow

B.Sc., Thompson Rivers University, 2014

Thesis Submitted in Partial Fulfillment of the
Requirements for the Degree of
Master of Science

in the
Department of Physics
Faculty of Science

© Brendin Thomas Chow 2017
SIMON FRASER UNIVERSITY
Summer 2017

All rights reserved.
However, in accordance with the *Copyright Act of Canada*, this work may be reproduced without authorization under the conditions for "Fair Dealing." Therefore, limited reproduction of this work for the purposes of private study, research, education, satire, parody, criticism, review and news reporting is likely to be in accordance with the law, particularly if cited appropriately.

Approval

Name:	**Brendin Thomas Chow**
Degree:	**Master of Science (Physics)**
Title:	***Technological Improvements for Linear Ion Trap Experiments***
Examining Committee:	**Chair:** Dr. Eldon Emberly Professor

Dr. Paul C. Haljan
Senior Supervisor
Associate Professor

Dr. Jeffrey McGuirk
Supervisor
Associate Professor

Dr. David Broun
Internal Examiner
Associate Professor
Department of Physics

Date Defended: 26 May 2017

Abstract

Laser-cooled, trapped ions are a highly controlled experimental system that allows one to engineer novel quantum states of both fundamental and practical interest. For a string of ions in a linear radio frequency (RF) Paul trap, the linear-zigzag structural phase transition is an intriguing system to investigate quantum dynamics near the critical point of a prototype second-order phase transition, including the preparation of superposition states of different structural configurations. This thesis focuses on two technological improvements required for studying the linear-zigzag structural phase transition in the quantum regime. The first is the development of a compact and cost-effective RF synthesizer setup to provide multiple modulation sources for the laser manipulation of ion strings. The functionality and limitations of a prototype design, based on Direct Digital Synthesizer (DDS) development boards with a microcontroller interface, are evaluated and future improvements are identified. The second part of this thesis focuses on the stabilization of the secular trap frequencies in a linear Paul trap, which is necessary to obtain a stable critical point for the studies of the linear-zigzag transition. To this end, this thesis presents the implementation of a Ramsey spectroscopic technique to measure the secular frequencies and presents the preliminary results from the stability tests.

Keywords: Direct Digital Synthesis; Linear RF Paul Trap; Secular Trap Frequency Stabilization

Dedication

To my mom and dad, and their continuing love and support.

Acknowledgements

I would not be where I am today without the people that surround me and the people who have always supported me from day one.

First and foremost I would like to thank my senior supervisor Dr. Paul Haljan for all of his guidance and support. The number of long hours he put into guiding me towards my goals is endless and deeply appreciated. He made the lab environment very easy to work in and provided me with the knowledge I needed to complete my masters studies. His contribution to my education will never be forgotten.

I would also like to thank my supervising committee member Dr. Jeffrey McGuirk whose input was always greatly appreciated.

I would like to thank those of the Haljan group both current and past who provided amazing companionship during the long hours in the lab. I would especially like to thank Jie Zhang who was always willing to answer my questions and help me out with things I did not quite understand.

I would like to thank all of my high school teachers who really got me motivated and excited to pursue a career in the sciences. Mr. Whitmore, Mr. Poelzer, Mr. Comita and Mr. Epp; you all played a vital role in getting me to choose science as a life career and I can never thank you enough for making science fun.

Next I would like to thank my friends, both my fellow graduate students at SFU Physics and my friends back home or scattered around the world. Without your support and encouragement I doubt I could have completed this degree with the amount of sanity I still posses.

Finally but most importantly I would like to thank my family for all of their love and support. My parents have always pushed me and encouraged me to be the best that I can possibly be. Without all of their support I would not be where I am today. My whole family have been avid believers in my work and have always believed I would achieve something great. I don't think I am there quite yet, but I know they will always support me no matter what I do.

Thank you.

Table of Contents

List of Tables

List of Figures

Chapter 1

Introduction

Ion traps are highly controllable systems that have found many applications including mass spectrometry, precision spectroscopy, atomic clocks and quantum information processing [73]. A yet further application of ion traps, which is the motivation of this thesis, is exploring the dynamics of prototype phase transitions [32, 54]. A versatile form of ion trap, which is common to several of the above applications, is the linear radio frequency (RF) Paul trap. The linear ion-trap design comes from the "racetrack" configurations used by Drees and Paul for the short-term confinement of plasmas in the 1960's [17]. Linear RF Paul traps, which were first explored at JPL [55] and NIST [57] for multi-ion atomic clocks, are now well known for their use in ion-based quantum information processing and quantum simulations [8, 75, 1, 73, 32], but they are also a convenient ion-trap setup for studying mesoscopic phase transitions between structures of ion crystals.

The dynamics of the crystallization and the formation of different structures of ion crystals in ion traps have been investigated since the 1950's [43]. With the advent of laser cooling, which allowed the crystallization of spatially localized atomic ions to be realized [49, 16, 74], interest grew in applying trapped ions for studying "few-body phase transitions;" in particular, those between different structural arrangements of ion crystals [72, 6, 20]. In a linear RF Paul trap with sufficiently strong transverse confinement, laser cooled ions form a 1-D linear crystal structure that lies along the trap axis. However, if the transverse confinement is relaxed compared to the axial confinement, a 2-D zigzag structure emerges with the ions displacing along the axis that is weakened [57, 61, 19, 25]. There has been considerable attention, both theoretical and experimental, related to the linear-zigzag transition. (For a recent review see [54] and [22] and the references therein). The interesting properties of the linear-zigzag transition along with the high controllability that can be realized with trapped ions has led to several proposals in recent years to explore different aspects of the transition in both the classical and quantum regime [59, 43, 11, 35, 2, 3, 27]. A theoretical proposal related to the dynamics of the intrinsic quantum double-well near the linear-zigzag critical point [59] is the long-term motivation for the work in this thesis. We are interested to see if

the double well can be controlled sufficiently well to create quantum superpositions of the two possible symmetry-broken configurations, so called *zig* and *zag* (see Chp. 2), arising from the second-order nature of the phase transition, and to investigate the decoherence of these states with ion number [22].

The technical requirements to observe the double-well dynamics in the quantum regime were evaluated by my predecessor and the preliminary experiments towards this goal were performed [22]. Some technological improvements to the experiment are needed to go further, specifically, an increase in the number of RF sources available for laser-modulation-based manipulation of ions, and an increase in the stability of the trapping potential. For experiments with strings of N ions − be it for the linear-zigzag studies or more generally for future research directions − there is a need for many RF sources to ground-state cool and manipulate even a subset of the $3N$ collective vibrational modes. However, stand-alone RF synthesizers tend to be quite costly and take up a significant amount of laboratory space. A solution that has shown to be convenient and inexpensive is to build a system from off-the-shelf components utilizing a synthesizing technique known as Direct Digital Synthesis (DDS). Direct digital synthesizers are agile, compact, and relatively inexpensive options for RF-intensive experiments and are popular choices for engineering and atomic, molecular and optical (AMO) physics applications [37, 76, 7, 18, 44, 48, 36]. We have assembled a prototype system from commonly available components and development boards, and have made preliminary tests of the system's RF output characteristics against a commercially available synthesizer. While the RF performance appears to be adequate for our purposes, the interface using a LabView-programmed Arduino microcontroller has been found, as will be discussed, to be inconvenient for a final system to be integrated with the main experiment.

As previously stated, our group currently aims to explore the linear-zigzag transition in the quantum regime, and in particular to investigate the intrinsic double-well dynamics and tunnel splitting effect in the lowest energy levels of the double well. To allow for this exploration it was previously determined that the trapping potentials would have to be stabilized (see [22] for greater detail). The ion trap potentials, which near the trap center are to a good approximation 3-D harmonic, are characterized by three *secular trap frequencies*. An initial target of 10 ppm stability in the secular trap frequencies was set as an initial goal to achieve stable trapping potentials to have tunneling oscillations with reasonable fidelity in a string of four ions. The first technical improvement made was to servo the input power to the RF resonator feeding the ion trap, but this was found to be insufficient to stabilize fully the secular trap frequencies in the transverse direction [22]. By way of improvement here, a scheme adapted from [33] has been used to sample and servo the RF voltage closer to the trap. A servo of the DC voltages controlling the axial ion trapping potential has also been implemented, and preliminary assessments of the trapping potential's stability using a single trapped ion will be reported. The results of the preliminary assessment, for an ion

trap with secular frequencies of 0.9 MHz and 0.3 MHz in the transverse and axial directions respectively, were a transverse stability of 65 ppm over 80 minutes with a standard deviation of 15 ppm, and an axial stability limited by a linear drift of 70 ppm/hr.

After this introduction, Chapter 2 of the thesis begins with a review of the theory of ion trapping, driven two-level systems, and two-photon optical Raman transitions as background for the subsequent discussions. The chapter concludes with a more detailed review of the linear-zigzag transition for ions in a linear RF Paul trap, including prior theoretical and experimental work and motivations underlying this thesis. Chapter 3 briefly discusses portions of the experimental setup relevant to this thesis work including the Raman laser setup, microwave generation, and ion-trap voltage system. The main results of the thesis are contained in Chapters 4 and 5. Chapter 4 provides a discussion of the multichannel RF synthesizer design that was implemented and how it compares to other designs currently being used elsewhere. This is followed by details of several system tests that were performed, and future steps for the project. Chapter 5 provides the theory and methodology of the Raman Ramsey spectroscopy that was employed to assess the stability of the ion-trap potential of our linear RF Paul trap. The results are then given for the stability measurements made before and after modifications to the setup that are outlined in Chapter 3. Finally, the conclusions of this thesis are presented in Chapter 6.

Chapter 2

Ion Trap Background and Theory

2.1 Introduction

This chapter provides the background to understand the measurement techniques and the results presented in this thesis. First, a theoretical model of a linear RF Paul trap is presented including the definitions of key parameters such as the secular trap frequencies. Next, there is a brief discussion on the Ytterbium ion and the key atomic transitions used for this thesis work. Raman sideband spectroscopy is used for assessing the stability of the secular frequencies; thus, a discussion of the Rabi two-level problem and its extension to two-photon stimulated Raman transitions will be discussed. Finally, the chapter concludes with a discussion of the linear-zigzag transition for trapped ions. Two technical requirements to allow the group to explore the linear-zigzag transition in the quantum regime are highlighted as motivation for the work in this thesis.

2.2 Ion-Trap Model

This thesis work utilizes a linear RF Paul trap with a design as already discussed in [21, 22]. The trap is constructed using four tungsten rods and two tungsten end-cap needles (see Fig. 2.1). The four rods have a diameter of 0.48 mm with a trap-axis to rod-surface distance of $R_o = 0.66$ mm and an end-cap spacing of $2z_o = 2.5$ mm. In the following, a simplified version of the electric potentials from the linear RF Paul trap and the resulting pseudo-potential will first be presented for clarity, and then a more complete version including numerically determined geometry factors will be given. The electric potential can be approximated near the trap axis as [75]

$$\Phi \cong \frac{(V_0 \cos(\Omega_T t) + U_{Rod})}{2}\left[1 + \frac{(x^2 - y^2)}{R^2}\right], \tag{2.1}$$

where R is an effective radius close in value to the ion-electrode distance R_o.

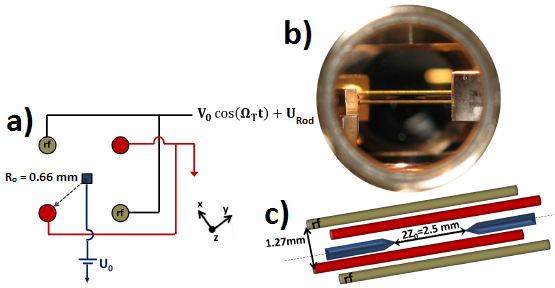

Figure 2.1: Simplified version of the linear RF Paul trap used for this thesis work [22]. a) shows a simple connection setup for the rod and endcap electrodes from a view down the trapping axis. The olive-green shaded rods are connected to an RF and DC voltage; $V_0\cos(\Omega_T t) + U_{Rod}$. The red-shaded rods are connected to ground. The blue square node is one of the endcaps connected to the DC voltage U_0. b) shows a side view of the linear Paul trap inside the vacuum chamber. See Chp. 3 for a complete trap voltage setup. c) shows the trap geometry from a side-angle view.

The two end-cap needles are connected to a DC voltage, U_0, which creates a confining potential for the ions in the $\hat{z}$ (axial) direction. The end caps provide a static electric potential that is described for points near the trap center by

$$\Phi_s = \kappa U_0 \left[z^2 - \frac{1}{2}(x^2 + y^2) \right], \tag{2.2}$$

where κ is a geometrical factor. Both Eqn. 2.1 and Eqn. 2.2 are simplified in that they do not factor in "real-world" issues like trap asymmetries, stray external fields, anharmonicities and RF leakage into the axial direction.

From the classical equations of motion for a single ion with mass M and charge Q in the potentials given in Eqns. 2.1 and 2.2, the position of a single ion can be obtained in the pseudo-potential approximation to be [73]

$$x_i(t) \approx x_{0i}\cos(\omega_i t + \phi_i)\left[1 + \frac{q_i}{2}\cos(\Omega_T \cdot t)\right], \tag{2.3}$$

where the secular trap frequency in the i^{th} direction is defined as

$$\omega_i \cong \frac{1}{2}\Omega_T \sqrt{a_i + \frac{1}{2}{q_i}^2}, \tag{2.4}$$

and a_i and q_i are given by

$$a_x = \frac{4Q}{M{\Omega_T}^2}\left(\frac{U_{rod}}{R^2} - \frac{\kappa U_0}{{Z_0}^2}\right);\ a_y = -\frac{4Q}{M{\Omega_T}^2}\left(\frac{U_{rod}}{R^2} + \frac{\kappa U_0}{{Z_0}^2}\right);\ a_z = \frac{8Q\kappa U_0}{M{\Omega_T}^2{Z_0}^2}; \tag{2.5}$$

$$q_x = -q_y = \frac{2QV_0}{M{\Omega_T}^2 R^2};\ q_z \approxeq 0.$$

Equation 2.3 reveals two different oscillatory motions for an ion. The first motion is the low-frequency secular motion describing the oscillations in a harmonic pseudopotential characterized by the secular trap frequency, ω_i. For our setup the secular trap frequency is $\omega_z/2\pi \simeq 0.32$ MHz axially and $\omega_{x,y}/2\pi \simeq 0.91$ MHz transversely. The second oscillatory motion is high-frequency motion that oscillates with the trap frequency Ω_T ($\Omega_T/2\pi \approx 17$ MHz for our setup). This motion is known as micromotion with an amplitude (given by $\frac{x_{0i}q_i}{2}$) that is smaller than the secular motion amplitude (given by x_{0i}) since $q_i \ll 1$ is assumed in the pseudopotential approximation. Micromotion only vanishes at the RF null (corresponding to a line along the axial direction in an ideal linear trap). In practice the trap center can be shifted from the RF null by stray DC electric fields and gives rise to excess micromotion, which leads to detrimental effects in for example Doppler cooling. However, by detecting micromotion [5], we can apply a DC shift in the rod voltages to overlap the trap center transversely with the RF null.

Recent detailed numerical simulations of our linear trap [28] provide the following next-order harmonic expansion for the electric potential arising from the rod voltages:

$$\Phi \approx \left(\frac{V_o\cos(\Omega_T t) + U_{rod}}{2}\right)\left[const + C_{22}\frac{(x^2-y^2)}{{R_o}^2} + C_{20}\frac{(r^2-2z^2)}{{R_o}^2}\right], \tag{2.6}$$

where C_{22} and C_{20} are constants that depend on the trap geometry and have been determined numerically to be

$$C_{22} = 0.889; \qquad C_{20} = 0.0106 \ll C_{22}. \tag{2.7}$$

In the second term in Eqn. 2.6, C_{22} would be unity for an ideal transverse quadrupole while its actual value in Eqn. 2.7 leads to the effective radius R introduced above. The third term in Eqn. 2.6 is responsible for the transverse fields (both RF and DC) leaking into the axial direction and thereby influencing the axial secular frequency. This term is also responsible for lifting the degeneracy between the x and y secular frequencies. From Eqn. 2.6, Eqns. 2.5 are rewritten as:

$$\begin{gathered} a_x = \frac{4Q}{M{\Omega_T}^2}\left(\frac{C_{22}(1+\epsilon)U_{rod}}{{R_o}^2} - \frac{\kappa U_0}{{Z_0}^2}\right);\ a_y = -\frac{4Q}{M{\Omega_T}^2}\left(\frac{C_{22}(1-\epsilon)U_{rod}}{{R_o}^2} + \frac{\kappa U_0}{{Z_0}^2}\right); \\ a_z = \frac{8Q\kappa}{M{\Omega_T}^2{Z_0}^2}\left(U_o - \frac{U_{rod}}{2}\right); \end{gathered} \tag{2.8}$$

$$q_x = \frac{2C_{22}(1+\epsilon)QV_0}{M{\Omega_T}^2R^2};\ q_y = -\frac{2C_{22}(1-\epsilon)QV_0}{M{\Omega_T}^2R^2};\ q_z = -\frac{2\kappa QV_o}{M{\Omega_T}^2{Z_o}^2},$$

where $\epsilon = \frac{C_{20}}{C_{22}}$ characterizes the $x-y$ symmetry breaking, and $\frac{\kappa}{{Z_o}^2} \equiv \frac{2C'_{20}}{{R_o}^2}$ with $C'_{20} \approx C_{20}$ allows for the evaluation of the axial geometry factor κ introduced in Eqn. 2.2. The Eqns. 2.8 allow for an understanding of the sensitivity of the secular frequencies to various parameters

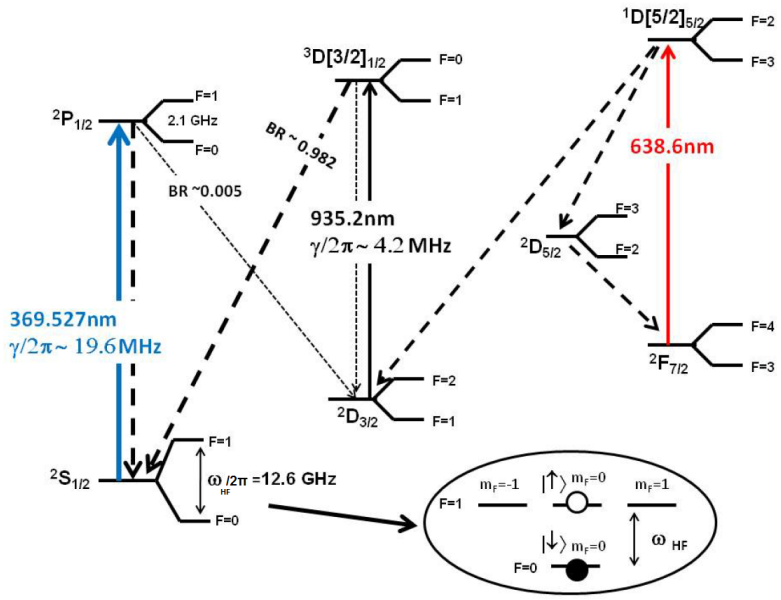

Figure 2.2: Relevant atomic energy levels of $^{171}Yb^+$ [21]. A zoom-in of the ground-state hyperfine manifold is shown. The various optical transitions are shown as well as the different branching ratios (BR) between levels.

- voltages, Ω_T, R, Z_o - and ultimately an estimation of the effect of variations in the parameters on the stability of the intrinsic double well near the linear-zigzag critical point (see Sec. 2.7).

2.3 Ytterbium Ion

Ion traps are utilized for a number of purposes like atomic clocks and quantum information applications, and various ion species are in use. The ion that is used for this thesis is $^{171}Yb^+$. $^{171}Yb^+$ has a single active electron, which allows it to have a relatively simple energy level structure (see Fig. 2.2). Due to its nuclear spin of $I = \frac{1}{2}$, it also has a simple hyperfine structure. The hyperfine "clock" states $|\downarrow\rangle \equiv {}^2S_{1/2}\,|F = 0, m_F = 0\rangle$ and $|\uparrow\rangle \equiv {}^2S_{1/2}\,|F = 1, m_F = 0\rangle$ in the ground-state hyperfine manifold (Fig. 2.2) have reduced magnetic-field sensitivity at low fields, and for this reason we make use of these states for microwave and optical Raman spectroscopy in this thesis. (They are also used as a hyperfine ion-qubit in quantum information applications.) The separation of the $|\downarrow\rangle$ and $|\uparrow\rangle$ states is 12.6 GHz.

There are three relevant optically driven transitions shown in Fig. 2.2. The ${}^2S_{1/2} - {}^2P_{1/2}$ transition at 369.527 nm with a linewidth of $\gamma/2\pi = 19.6$ MHz is used for fluorescence state detection, laser cooling, and off-resonant coupling to drive two-photon Raman transitions between $|\downarrow\rangle$ and $|\uparrow\rangle$. The next transition is ${}^2D_{3/2} - {}^3D[3/2]_{1/2}$ used for repumping. Occasionally during fluorescence the ion will transition to the low-lying state of ${}^2D_{3/2}$ with a

branching ratio of $\alpha = 0.005$ [50], which will require repumping the ion into the $^2S_{1/2} - ^2P_{1/2}$ fluorescence transition. This repumping is performed by driving the $^2D_{3/2} - ^3D[3/2]_{1/2}$ transition (935.2 nm, $\gamma/2\pi = 4.2$ MHz) with a branching ratio from $^3D[3/2]_{1/2}$ to the ground state of $\beta = 0.982$ [38]. The last transition that we are concerned about is another repump one, $^2F_{7/2} - ^1D[5/2]_{5/2}$, where the energy level $^2F_{7/2}$ is long-lived and metastable. The ion can get "knocked" to this state from the low lying D-states by background gas collisions [4]. To repump the ion back to the fluorescence transition, a 638-nm laser is needed.

2.4 Driven Two-Level System: Rabi Rotations

As the technology and measurements in this thesis deal with coherent operations and spectroscopy involving the $|\uparrow\rangle$ and $|\downarrow\rangle$ states, we briefly summarize the theory of a driven two-level system, following the presentation in [45]. In the next section and of particular relevance to this thesis, we will extend the discussion to the case of spin-motion states with Raman coupling.

A two-level system consists of a ground state $|g\rangle$ and an excited state $|e\rangle$. These levels are separated by an energy $\hbar\omega_o$ where $\hbar\omega_o = E_e - E_g$ and $E_e > E_g$. We can write the wavefunction of a two-level system as

$$|\psi\rangle = C_g e^{-i\frac{E_g t}{\hbar}} |g\rangle + C_e e^{-i\frac{E_e t}{\hbar}} |e\rangle , \tag{2.9}$$

where C_g and C_e are amplitudes in the interaction picture and satisfy the normalization relation $|C_g|^2 + |C_e|^2 = 1$. The time-dependent Schrödinger equation is written in general as

$$i\hbar \frac{dC_j(t)}{dt} = \sum_k C_k(t) H'_{jk}(t) e^{i\omega_{jk}t}, \tag{2.10}$$

where C_j and C_k are the amplitudes of two states and H'_{jk} is the interaction between states $|j\rangle$ and $|k\rangle$. From Eqn. 2.10, the time evolution of C_g and C_e can be written as

$$\begin{aligned} \dot{C}_g(t) &= -i\frac{H'_{ge}(t)}{\hbar} e^{-i\omega_o t} C_e(t) \\ \dot{C}_e(t) &= -i\frac{H'_{eg}(t)}{\hbar} e^{i\omega_o t} C_g(t), \end{aligned} \tag{2.11}$$

where ω_o is the atomic resonance frequency as defined above. The coupling interaction due to an applied driving field with oscillation frequency ω can be expressed in general as

$$\hat{H}' = \hbar\Omega \cos(\omega t) \left[|e\rangle \langle g| + |g\rangle \langle e| \right], \tag{2.12}$$

where Ω is the Rabi frequency. Equation 2.12 in particular includes the case of microwave coupling, $H' = \vec{\mu} \cdot \vec{B}$, between spin states $|\downarrow\rangle$ and $|\uparrow\rangle$. From Eqn. 2.12 and by applying the rotating-wave approximation [45], Eqn. 2.11 can be rewritten as

$$\begin{aligned} \dot{C}_g(t) &= -i\frac{\Omega^*}{2}e^{i\delta t}C_e(t) \\ \dot{C}_e(t) &= -i\frac{\Omega}{2}e^{-i\delta t}C_g(t), \end{aligned} \tag{2.13}$$

where $\delta = \omega - \omega_o$ is the detuning. The solution to Eqn. 2.13 (i.e. the solution in the interaction picture) is

$$\begin{bmatrix} C_g(t) \\ C_e(t) \end{bmatrix} = \begin{bmatrix} \left(\cos\frac{\theta}{2} - i\frac{\delta}{\Omega'}\sin\frac{\theta}{2}\right)e^{i\delta\frac{t}{2}} & -i\frac{\Omega^*}{\Omega'}\sin\frac{\theta}{2}e^{i\delta\frac{t}{2}} \\ -i\frac{\Omega}{\Omega'}\sin\frac{\theta}{2}e^{-i\delta\frac{t}{2}} & \left(\cos\frac{\theta}{2} + i\frac{\delta}{\Omega'}\sin\frac{\theta}{2}\right)e^{-i\delta\frac{t}{2}} \end{bmatrix} \begin{bmatrix} C_g(0) \\ C_e(0) \end{bmatrix}, \tag{2.14}$$

where $\theta \equiv \Omega' t$ and $\Omega' = \sqrt{|\Omega|^2 + \delta}$ is the generalized Rabi frequency. Equation 2.14 can be expressed in a more convenient reference frame (often called the "laser rotating frame" in the case of a laser interaction) in which the phasor of the driving field is stationary in time. In this reference frame the wavefunction from Eqn. 2.9 is written as

$$|\psi\rangle = C'_g\,|g\rangle + C'_e e^{-i\omega t}\,|e\rangle\,, \tag{2.15}$$

with connections to C_g and C_e as follows:

$$\begin{aligned} C_g &= C'_g \\ C_e &= e^{-i\delta t}C'_e, \end{aligned} \tag{2.16}$$

where C'_g and C'_e are the amplitudes for the ground state and the excited state in the frame rotating with the driving field, respectively. Therefore in this frame, the solution to Eqn. 2.13 is

$$\begin{bmatrix} C'_g(t) \\ C'_e(t) \end{bmatrix} = e^{i\delta\frac{t}{2}} \begin{bmatrix} \cos\frac{\theta}{2} - i\frac{\delta}{\Omega'}\sin\frac{\theta}{2} & -i\frac{\Omega^*}{\Omega'}\sin\frac{\theta}{2} \\ -i\frac{\Omega}{\Omega'}\sin\frac{\theta}{2} & \cos\frac{\theta}{2} + i\frac{\delta}{\Omega'}\sin\frac{\theta}{2} \end{bmatrix} \begin{bmatrix} C'_g(0) \\ C'_e(0) \end{bmatrix}, \tag{2.17}$$

where $\Omega = |\Omega|\,e^{i\phi}$. Thus, except for an irrelevant overall phase factor, the phase evolution terms have been removed. For the case of resonance ($\delta = 0$), the matrix in Eqn. 2.17 represents a spin-1/2 Pauli rotation by angle θ along the x or y direction on the Bloch sphere depending on the value of ϕ.

2.4.1 Two-Photon Stimulated Raman Transitions

In this thesis we make use of stimulated two-photon optical Raman transitions [75] to probe the secular frequencies of a trapped ion. This involves coupling the internal spin of the ion and the harmonic oscillator states $|n\rangle$ associated with the ion's vibrational motion in the trap. This spin-motion coupling scales with the wave packet size x_o and the wavelength, λ of an incident electromagnetic wave as x_o/λ. For trapped ion experiments we need a strong spin-motion coupling to manipulate the ion for operations such as ground-state cooling. For $^{171}Yb^+$, the wave packet size, x_o, is $\sim$ 5 nm in the vibrational ground state at a 1-MHz secular frequency. Furthermore for $^{171}Yb^+$, the spin states are separated by 12.6 GHz; thus, for a single-photon transition we would need a microwave field, which for lane-wave illumination causes the spin-motion coupling to become negligibly small due to the long wavelength. One common way to get around this issue of weak spin-motion coupling is by using stimulated optical Raman transitions [75].[1] Figure 2.3 shows a two-photon stimulated Raman transition where states $|\downarrow, n\rangle$ and $|\uparrow, n'\rangle$ are coupled by two laser fields via the intermediate excited $^2P_{1/2}$ state. To a good approximation for $\Delta_R \gg \gamma$, where Δ_R is the detuning and γ is the natural linewidth of the transition, the intermediate state can be adiabatically eliminated and the transition from $|\downarrow, n\rangle \rightarrow |\uparrow, n'\rangle$ can be treated as an effective two-level system as described in the previous section.

When one wishes to describe a motion-sensitive Raman transition[2] there are three types: carrier, red sideband, and blue sideband. The carrier transition is one where the motional state of the ion is left unchanged but the spin state is flipped: $|\downarrow, n\rangle \rightarrow |\uparrow, n\rangle$. The first red sideband transition ($|\downarrow, n\rangle \rightarrow |\uparrow, n-1\rangle$) will decrease the motional state of the ion while flipping the spin state, while the first blue sideband transition ($|\downarrow, n\rangle \rightarrow |\uparrow, n+1\rangle$) will increase the motional state of the ion while also flipping the spin state. The Rabi frequency for a carrier transition between motional ground states ($|\downarrow, n=0\rangle \rightarrow |\uparrow, n'=0\rangle$) is

$$\Omega = \frac{\Omega_1^* \Omega_2}{2\Delta_R}, \tag{2.18}$$

where Ω_1 and Ω_2 are the resonant Rabi frequencies for a single-photon transition, due to the first and second Raman laser beams respectively. In general, the Rabi frequency for a given Raman transition is given by $\Omega_{n,n'}$ which has a complicated dependency on the motional states n and n' [75]. In the simplified case of the Lamb-Dicke limit ($\sqrt{\Delta k^2 \langle x^2 \rangle} \ll 1$ where Δk is the Raman wavevector difference and $\langle x^2 \rangle^{\frac{1}{2}}$ is the ion's wavepacket size) the Rabi frequency of the first blue sideband transition is approximately

$$\Omega_{n,n+1} = \eta\Omega\sqrt{n+1}, \tag{2.19}$$

[1] Other possibilities involving microwaves make use of near-field microwave gradients [51] or a combination of microwaves and magnetic field gradients [68].

[2] A motion-insensitive Raman transition involving only a spin coupling is also possible. See [75].

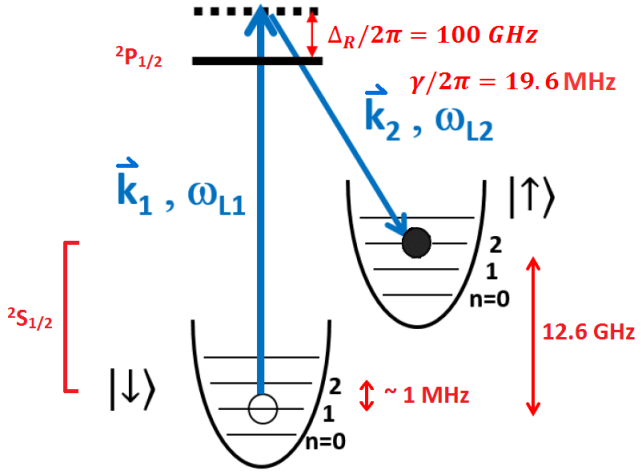

Figure 2.3: A stimulated two-photon Raman transition (first blue sideband). The linewidth γ of the upper state is given as well as the laser detuning Δ_R. The values $\left\{\vec{k_1},\ \omega_{L1}\right\}$ and $\left\{\vec{k_2},\ \omega_{L2}\right\}$ correspond to two different laser fields.

and for the first red sideband transition it is

$$\Omega_{n,n-1} = \eta\Omega\sqrt{n-1}, \tag{2.20}$$

where η is the Lamb-Dicke parameter [75]. The Lamb-Dicke parameter is defined as $\eta = \Delta k x_o$ where x_o is the rms spread of the ion's ground-state wavefunction.

There are two phenomena that are worth mentioning in the context of optical Raman transitions. Firstly, even though the intermediate level is adiabatically eliminated, residual spontaneous emission can limit coherence of a two-photon transition. The second phenomenon is the differential ac Stark shift of $|\downarrow\rangle$ and $|\uparrow\rangle$ due to the coupling to the intermediate state, which leads to a shift in the Raman resonance. In our experiment, the ac Stark effect causes a shift in the resonance by $\sim 7-10$ kHz, which leads to some slight complication in the sideband spectroscopy measurements to be discussed in Chp. 5.

2.5 Linear-Zigzag Transition

The linear-zigzag transition [6, 57, 61, 19] is one of several structural phase transitions that occur for trapped ion crystals when the confining potential or ion density is varied. Only a brief summary is provided here of the linear-zigzag transition as motivation for this thesis work, with a more extensive discussion and more extensive set of references to be found in [22]. We consider the specific case of an ion string in a linear RF Paul trap and a variation in the confining strength of the trap. The relationship between the axial confinement (provided

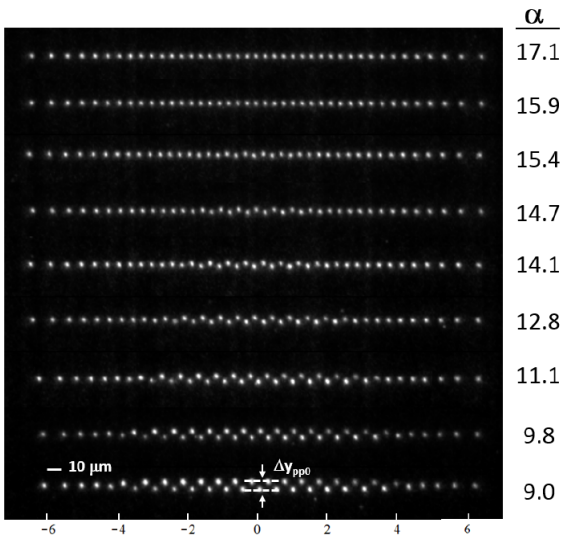

Figure 2.4: Images of a Yb^+ ion crystal showing the transition between a 1-D linear string and the 2-D zigzag structure [22].

by the end-cap needles) and the transverse confinement (provided by the rods) is given by the trap anisotropy α defined as

$$\alpha \equiv \frac{\omega_y}{\omega_z}. \tag{2.21}$$

For strong transverse confinement ($\alpha \gg 1$), several laser-cooled ions align into a linear string. When the transverse confinement is reduced, at some critical trap anisotropy (α_c) the linear structure is no longer energetically favourable for an ion crystal and the crystal goes through a phase transition to a 2-D zigzag configuration [57]. The transition also corresponds to a point of mechanical instability where the transverse zigzag vibrational mode frequency approaches zero for an ion crystal [25, 26]. Figure 2.4 shows how the 1-D structure of 41 $^{174}Yb^+$ ions transitions into the 2-D structure as the trap anisotropy is decreased. This 2-D structure is in the y-z plane where $\hat{z}$ is the axial trap direction and $\hat{y}$ is the transverse direction that was weakened. The two possible orientations of the structure, called "zig" and "zag," correspond to the cases where the odd- or even-numbered ions counting from the left are displaced upwards in Fig. 2.4. The "zig" state is defined as the configuration where the odd ions shift upwards, while the "zag" state is defined as the configuration where the even ions shift upwards. As can be seen in Fig. 2.4, the central ions displace first since the Coulomb pressure is highest in the middle of the 1-D linear structure. As the transverse confinement is further weakened, the outer ions begin to displace and join the 2-D zigzag configuration. At yet lower alpha, further structural transitions will occur [6].

There has been considerable attention both theoretical and experimental related to the linear-zigzag transition. For example, theoretically it has been shown to be a continuous

(i.e. second order) phase transition in the thermodynamic limit [53, 26], and the quantum linear-zigzag transition has been shown to be equivalent to a one-dimensional transverse field Ising model [64, 65]. The interesting properties of the linear-zigzag transition along with the high controllability that can be realized with trapped ions has led to several proposals to explore different aspects of the transition in both classical and quantum regimes [26, 59, 63, 35, 29, 12, 2, 60] (for a review, see [54]). One proposal related to kink nucleation [12] motivated a recent experiment performed in our group, and another proposal related to quantum double-well dynamics near the linear-zigzag critical point [59] is the motivation for the technical developments discussed in this thesis.

2.6 Recent Experiments Involving the Linear-Zigzag Transition at SFU

Previous work related to the linear-zigzag transition carried out by our group is given in detail in [22, 23, 40, 24]; however, a brief summary is provided here. Recent efforts have focused on studying the dynamics of the linear-zigzag transition near the critical point. The investigation of the Kibble-Zurek Mechanism (KZM), specifically measurements of the spontaneous nucleation of topological kink-defects as a function of quench rate across the linear-zigzag transition were made and found to be in good agreement with simulation results [23]. Three other groups also looked at kink-defect formation [46] and power-law scaling with quench rate [56, 71]. Explorations beyond the KZM tests in our group saw a look into the formation dynamics of two different types of kinks: discrete and extended [23]. The above studies were done at Doppler-cooled temperatures and involved dynamics in the classical regime. The first steps were subsequently taken by our group towards exploring dynamics near the linear-zigzag transition in the quantum regime at ultralow temperature [22], following the proposal in [59]. In particular, the initial goal was to see if it is feasible to prepare and study quantum superpositions of the two broken-symmetry states, the zig and zag configurations, by controlling the tunneling oscillations in the intrinsic double well near the critical point. To this end, deterministic state preparation of the zig or zag structure was demonstrated, and a preliminary characterization of the asymmetry in the double-well potential was done. For the purpose of efficient ground-state cooling, a successful demonstration of 3-D Sisyphus cooling was also shown to bring the mean phonon number for all vibrational modes of a four-ion crystal down close to $\bar{n} \approx 1$ [24]. Following ground-state cooling of the zigzag vibrational mode, an assessment of heating rates of the zigzag mode on both the linear side and the zigzag side of the transition were performed in order to understand decoherence effects near the critical point. To probe the decoherence due to heating closer to the critical point where tunneling becomes significant, a higher level of stability was found to be needed for the secular trap frequencies. This is the motivation for the part of this thesis work presented in Chp. 5.

2.7 Technological Improvements Required for the Quantum Regime

As noted above, the current goal of our group is to explore the linear-zizag transition in the quantum regime. The technical requirements to observe the intrinsic double-well quantum dynamics near the critical point, including tunneling, were investigated in detail in [22]. This thesis addresses two requirements in particular. First, we need a high degree of control and stability of the linear Paul trap potential due to the sensitivity of the tunneling frequency near the critical point. Second, an increase in the number of available RF synthesizer channels is needed to drive acoustic-optic modulators for laser cooling and state manipulation of the trapped ions. We summarize these needs in the following as a prelude to the subsequent thesis chapters:

RF synthesizer capacity: For a string of N ions there are $3N$ vibrational modes. Even if an experiment, such as the ones envisioned with the linear-zigzag transition, requires control of only a subset of all the modes, a number of RF sources is still needed. RF synthesizers are expensive and bulky, which makes having a large number of them impractical for our experiment. Direct digital synthesis is an RF generation scheme that allows for agile, cost-effective and compact synthesizers to be designed and constructed. Our synthesizer will need to be able to store many output profiles, with each profile having its own frequency, phase and amplitude, to satisfy the need to manipulate a number of vibrational modes. Furthermore, the synthesizer should be sufficiently agile to allow for the microsecond switching needed for different pulse sequences within an experiment. To construct an agile, multichannel direct digital synthesizer for our experiment, we have designed a system that utilizes off-the-shelf components, and has design similarities with homemade systems used in other AMO groups and engineering projects. This development is the topic of Chp. 4.

Ion-trap potential stability: For four ions in our linear Paul trap with $\omega_{x,y}/2\pi \approx 0.85$ MHz and $\omega_z/2\pi \approx 0.37$ MHz, it is shown in [22] that a stability of 10 ppm in the control parameter α (or a few Hertz in the transverse and axial secular frequencies) is required to obtain $\sim 20\%$ stability of the tunneling frequency. This 10 ppm level in the trap potential stability can probably be relaxed for the preliminary goal of heating assessments of the zigzag mode close to the critical point as discussed in the previous section. An understanding of the technical implications to reach such stability in the ion-trap potential can be gained from Eqn. 2.4, which provides the various dependencies of the secular trap frequencies on electrode spacing (i.e. mechanical stability), RF trap frequency, and various voltages. For the voltages, a stability of 10 ppm for the secular frequencies corresponds to a stability of 0.3 mV for DC rod voltages of ~ 1 V, 2 mV for the end-cap bias of 100 V, and 7 mV for an RF voltage of 700-V amplitude. The RF stabilization in particular is technically challenging due to the

multi-element RF setup that includes a quarter-wave resonator (with its own mechanical and temperature sensitivities) delivering high voltage to the ion trap. Prior experiments in our ion trap laboratory [22] found that drifts in the linear-zigzag critical point were correlated to the lab temperature, and servo'ing the RF power level into the resonator was tried but found to be insufficient to eliminate the drifts. The servo provided a factor-of-four improvement in transverse trap potential stability, but temperature-related sensitivities, likely due to the resonator itself, were still an issue. A stability at the level of 400 ppm was typical over 10 minutes to hour timescales; however, as stable as 40 ppm (30 Hz) transverse stability over 5 minutes was found to be possible when laboratory temperature variations were smaller. The next step considered here is to sample and servo the RF voltage after the resonator, which requires some care in not loading the resonator. Recently and for separate purposes related to quantum spin simulations with ion strings, a group in Maryland achieved an uncertainty of ± 10 ppm or ± 10 Hz in the transverse secular frequency of 1 MHz [33] by sampling and servoing the RF voltage after the resonator. We have adopted their techniques in our experimental setup as part of our goal of achieving a sufficiently stable trap potential. Preliminary stability results for our linear Paul trap is the topic of Chp. 5.

Chapter 3

Experimental Setup

3.1 Introduction

This chapter will give a brief explanation of relevant experimental setup used for this thesis. A much more detailed explanation of all the lasers used and other experimental setup is provided in my predecessor's theses [21, 22]. In anticipation of measurements of the trap potential's stability in Chp. 5, this chapter will first cover the basics of the RF and DC voltage supplies for creating the transverse and axial trapping potentials, and additional circuitry needed for stabilizing the voltages. The implementation of the stabilization circuitry is not part of this thesis and the details will be presented elsewhere [77]. Finally, the setup for the microwave generation system and the Raman beams will be summarized to provide the necessary context for the synthesizer project in Chp. 4 and the secular frequency measurements in Chp. 5.

3.2 Voltage Control Setup for the Linear Paul Trap

Figure 3.1 shows a basic block diagram of the rod and end-cap voltage setups used in the experiment to drive the linear RF Paul trap. The transverse trap potential from the rods is composed of two parts: a DC component and an RF component. The DC component is supplied by a National Instruments analog output card (PCI-6733). This card is controlled by a LabView program that allows for the DC voltages on the rods to be varied (typically $0 - 3$ V) for a number of reasons including the minimization of micromotion and for the ramping needed to induce the linear-zigzag transition. The PCI card is connected to a BNC breakout board (NI BNC-2110) which feeds a set of current-boosting amplifiers (for ramping purposes). The amplifier outputs are sent to ports on the helical RF resonator and added to the RF voltages on the trap rods through low-pass Bessel filters [22], which also provide RF grounding.

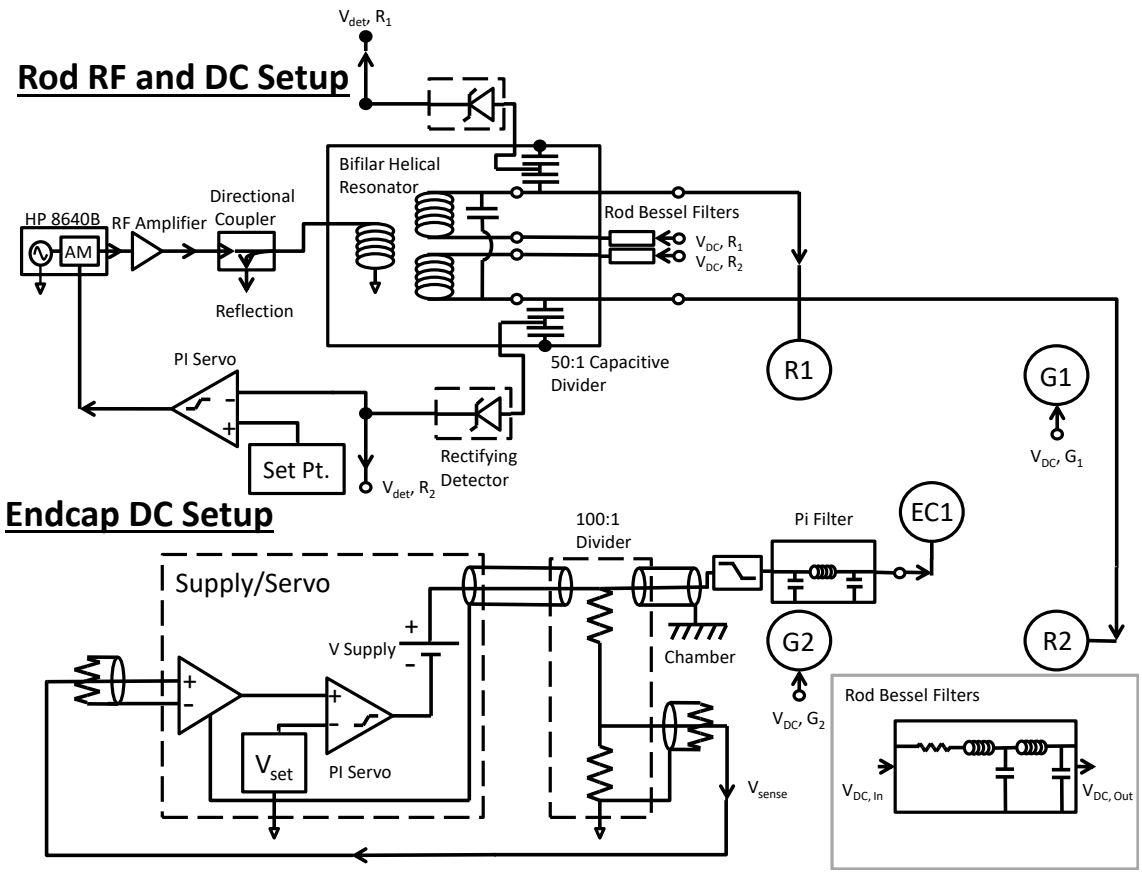

Figure 3.1: A simple block diagram of the RF and endcap voltage setups connected to the four trap rods $R1$, $R2$, $G1$, $G2$ and endcaps $EC1$ and $EC2$ ($EC2$ not shown). Note that the bifilar helical resonator is drawn only schematically.

The RF component of the transverse potential originates with an HP 8640B RF generator. This supplies a sinusoidal RF output at ~ 17 MHz (for the current helical resonator) at a power of ~ -14.0 dBm. This RF signal is sent to a ENI 325LA RF amplifier, which increases the power to ~ 5 W (~ 37 dBm). The amplified RF signal is sent through a directional coupler to the helical resonator [66], which steps up the RF voltage and provides impedance matching to the ion trap. The helical resonator used for this thesis is a twin coil design. This design was chosen over a more commonly used single-coil resonator because the twin coil allows the DC voltages on each rod to be individually adjusted. An upgraded resonator was added to the experiment to allow RF voltage sampling closer to the trap [77] in similar fashion to [33]. The RF voltage along with the DC component are then sent through a vacuum feed-through where they are connected to the four rods of the ion trap, giving a typical transverse secular trap frequency of ~ 0.9 MHz. The output of the helical resonator is stabilized using a servo (New Focus LB1005) that applies the correction to the AM input of the HP RF generator (as shown in Fig. 3.1). The sampling voltage for the servo is obtained by a capacitive voltage divider at the output of one of the two coils

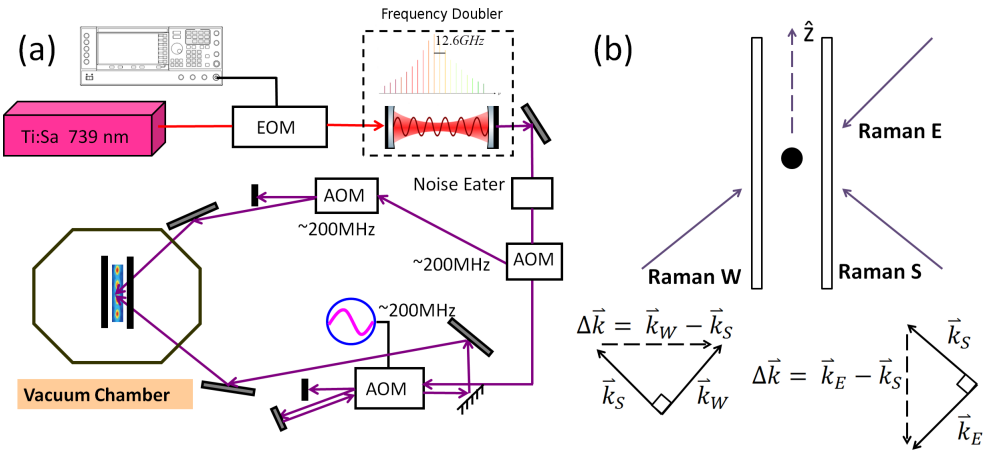

Figure 3.2: Figure (a) is a simple diagram of the Raman beam setup used in the experiment. Figure (b) shows the wavevector differences for coupling to the trapped ion motion along different directions.

of the helical resonator and a temperature-compensated rectifying detector [33], giving a typical sense output of 2 V. The set-point voltage is provided by a precision voltage supply (AD5791).

The axial potential is provided by a DC voltage applied to both end caps. The DC voltage is supplied by an Agilent E3612A DC power supply. The typical end-cap supply voltage for this thesis is ~ 78 V giving an axial secular trap frequency of ~ 0.3 MHz. The DC voltage is passed through a low-pass RC filter (time constant ~ 1 ms) and a π-filter for RF grounding near the vacuum feedthrough. The DC power supply is servo'ed to stabilize the output. The output voltage is sampled before the filters using a 100:1 precision voltage divider (sense voltage is ~ 0.78 V), which is fed into a homemade servo. The set-point voltage is provided by a temperature-stabilized voltage reference internal to the servo.

3.3 Microwave Source

Microwaves are used in the experiment to perform coherent spin operations on the $|\uparrow\rangle \rightarrow |\downarrow\rangle$ hyperfine transition at 12.6 GHz. At the heart of the microwave system is an HP 8671B microwave synthesizer, which feeds a Transistor-Transistor Logic (TTL) switch controlled by the experiment control computer. This TTL switch output is sent to a microwave amplifier connected to a microwave horn that sits underneath the ion trap. The microwave synthesizer is phase locked to an external 10−MHz reference, either an ovenized reference oscillator or a GPS-conditioned Rubidium standard.

3.4 Raman Beam Setup

Figure 3.2(a) shows a simplified diagram of the Raman laser beam setup used in our experiment. A 739-nm, stabilized Titanium-Sapphire laser is frequency doubled to 369.5 nm and split off into three beam paths (one path not shown) that are called *Raman South*, *Raman West* and *Raman East*. A 6.3-GHz electro-optic modulator (EOM) before the frequency doubler is used to generate a frequency comb in the Raman beams for bridging the 12.6-GHz hyperfine transition. Two pairs of beams, south and west, and south and east, create Raman wavevector differences to couple to ion motion along the transverse ($\hat{x}-\hat{y}$) and axial ($\hat{z}$) directions in the trap, respectively (see Fig. 3.2(b)). Each beam is modulated by an acoustic-opto modulator (AOM), which is fed from externally referenced RF synthesizers, for switching, and in the case of Raman South, for frequency tuning purposes. The Raman South beam uses a double-pass AOM configuration to suppress beam pointing changes during frequency scans. There is a bank of four synthesizers connected to the Raman South AOM for various needs such as the motional spectroscopy considered in Chp. 5. In anticipation of future experiments with several ions, for example those involving the linear-zigzag transition of up to ~ 10 ions, there is a need for more frequencies to perform operations like spectroscopy and cooling. This need motivates the development of a DDS system, to be discussed in Chp. 4, similar in design to other trapped ion groups [48, 36, 62, 52].

Chapter 4

Developing a Multi-Channel Direct Digital Synthesizer

4.1 Introduction

This chapter begins with an outline of the requirements for Raman RF control, which will motivate the need for a DDS (Direct Digital Synthesizer). A discussion of commercially available solutions will be discussed as well as prior work done by others to create viable DDS solutions. The prior synthesizer design pursued by the Haljan group will be discussed, which will be followed by a discussion of the synthesizer design pursued in this thesis. Construction of the synthesizer and the control interface will be discussed and some performance results of the AD9910 DDS evaluation board on which the synthesizer is based will also be shown. Finally, this chapter will conclude with key issues in the design and future steps for the project.

4.2 Technical Requirements

Signal generators are a key component for ion-trap experiments. In our experiment, RF generators are used to operate the acoustic-optic modulators (AOMs) and electro-optic modulators (EOMs) necessary to provide various operations from laser cooling to state manipulation. In particular, an RF-source-intensive aspect of the experiment are the optical Raman transitions required for sideband cooling, thermometry and other coherent operations involving ion spin and motion. For experiments with strings of N ions, including the proposed linear-zigzag investigations discussed above or quantum simulation and information processing applications, the need to cool and manipulate several of the $3N$ vibrational modes requires a system capable of generating multiple frequencies with controllable amplitude and phase. For example, a four-ion experiment of the linear-zigzag transition is expected to require ten synthesizer profiles. Of these profiles six would be

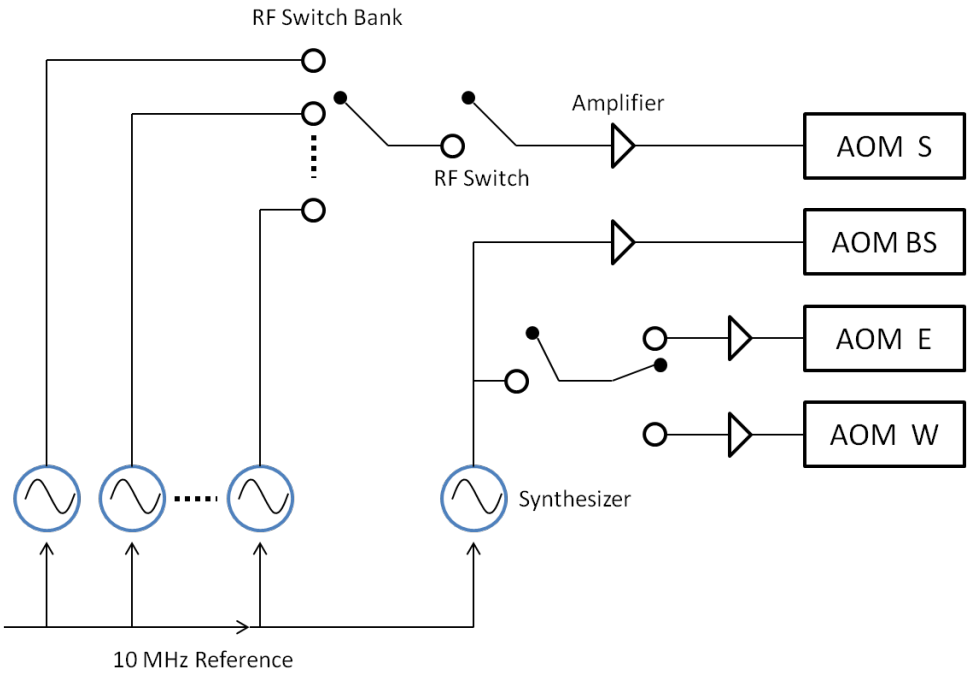

Figure 4.1: Simple diagram of the Raman AOM control setup.

needed for Raman sideband cooling and thermometry, while the remaining four would be used for spectroscopy and state manipulation close to the linear-zigzag transition. Future experiments in quantum simulation and quantum computing applications could require an even greater number of synthesizer profiles depending on the complexity of the desired experiment. Thus, a popular solution that reduces costs by eliminating a need to buy a large number of expensive generators and that provides the flexibility needed are direct digital synthesizers (DDSs). In order to motivate the DDS design pursued, we first discuss the current optical Raman setup and its RF requirements.

Figure 4.1 shows a simplified diagram of the Raman AOM setup currently used in the experiment. A set of synthesizers produce sinusoidal outputs that are routed using RF switches and are then amplified before reaching the AOMs. The beam-splitter (BS) AOM is responsible for splitting the Raman laser source into Raman West/East and Raman South beams (Sec. 3.4), and requires a constant 200-MHz signal to operate. The RF setup already in place for the BS AOM is sufficient as is. The synthesizer setup for the Raman East and West AOMs has fairly limited requirements since they operate at a fixed frequency of 200 MHz and only require some limited amplitude switching. This can be handled by the current RF sources and switch bank used in the experiment. The most demanding requirement comes from the Raman South AOM's RF input, which requires multiple sinusoidal profiles, each corresponding to a different frequency, amplitude and phase, for different operations such as coherent spin and motion manipulation, sideband cooling, and thermometry of collective vibrational modes. The timing requirements for switching between Raman

South profiles include microsecond switching within experiment pulse sequences and slower changes between experiments when scanning frequencies.

Currently, each profile is handled by a single synthesizer that passes its output to the TTL controlled RF switch bank for fast switching. The TTL signals are provided by a digital output card that is controlled by the experiment control program. The slow programming of the individual synthesizers is done by GPIB. At present, there are five synthesizers for just the Raman setup. More demanding experiments will require more profiles and therefore will require more synthesizers. Since increasing the number of synthesizers in the experiment is not a viable solution, an agile synthesizer with multiple profiles that takes advantage of DDS technology is a necessary upgrade for the experiment setup.

There are several possibilities to implement such an upgrade. The source for the Raman South AOM could in principle be replaced by a single DDS device that switches between internally stored profiles based on input triggers. One requirement for frequency shifting in this case is that the source needs to be phase coherent (so that phase is preserved when returning to a profile) rather than phase continuous. It is worth noting that an Arbitrary Waveform Generator (AWG) can achieve phase coherent switching, where the appropriate phase offset is calculated based on prior frequency (and phase) history prior to switching. However, this may suffer from potential memory limitations of the synthesizer and is not very convenient in implementation, especially if the frequency of one operation in a sequence is being scanned. A commercially available product exists from Photonics Technologies that fits the requirements for our needs [42]. Alternatively, a combination of synthesizers with profile memory is also possible. In this scenario, some of the synthesizers would be used for switching between various frequencies for tasks where phase is not relevant, and some of the synthesizers at fixed frequencies would be dedicated to switching between various phase profiles. There are various commercially available synthesizers from companies like Spinecore and Furaxa that have profile memory. However, homebuilt systems based around inexpensive DDS development boards have been a popular choice for many setups including those in Atomic, Molecular, Optical (AMO) experimental groups, as will be discussed in the next section.

4.3 Previous Work at SFU and Elsewhere

This DDS project follows a prior implementation with a similar design in the NIST Boulder ion group [36], and many other implementations for a variety of other purposes [52, 37, 48, 44, 18, 7, 76]. The previous synthesizer design in our group revolved around the Analog Devices AD9959 evaluation board [39]. Some of the attractive properties of the AD9959 included four-channel output and multiple frequency profiles. The DDS board was serially interfaced using a scheme called *Serial Peripheral Interface* (SPI), which will be discussed further in Sec. 4.7.1, with a National Instruments USB SPI controller (NI USB 8451), which

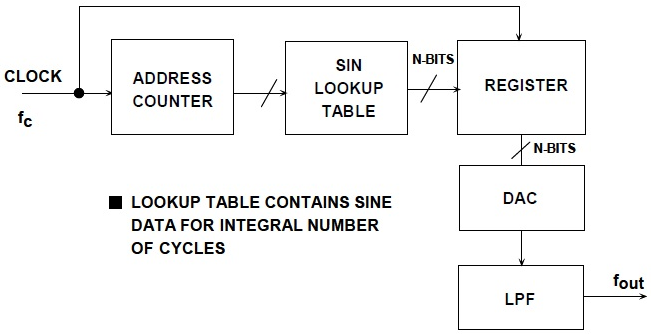

Figure 4.2: A simple block diagram of a Direct Digital Synthesizer (DDS). Reprinted with permission from [70]. Copyright (2009), Analog Devices Inc.

acted as the bridge between the AD9959 and the LabView program responsible for operating it. A system was constructed and some preliminary measurements of spurious features, output power as a function of output frequency, and phase noise were completed. One of the problems was that the device lacked the capability of being able to set the amplitude. Essentially the amplitude was always the maximum possible output value that the AD9959 chip could manage. This is not convenient since some RF signals need their amplitude to be adjusted during the setup of an experiment. The other major problem was the AD9959 was designed to operate with a 500-MHz clock frequency. Due to how a DDS operates (explained in more detail in Sec. 4.4), the output bandwidth is approximately half the clock frequency. Thus 250 MHz is the limit for the AD9959 to operate but noticeable spurious features associated with image frequencies start appearing at ~ 180 MHz. Since the RF frequencies required by the experiment are ~ 200 MHz, the AD9959 would have difficulty filtering the image frequencies at 200 MHz. Furthermore, the output of the evaluation board suffers from the roll-off of the output filter. Therefore a change to a different DDS chip, the AD9910, was needed to resolve the above issues, and a discussion of the work in this direction forms the rest of this chapter. The scope of the work done focused on five main topics: the Arduino interface between the control computer and the DDS development board, programming of the Arduino, RF performance of the AD9910 evaluation board, phase synchronization of multiple DDS boards, and interfacing the synthesizer with the main experiment program.

4.4 Direct Digital Synthesis Theory

A simple block diagram of a DDS is shown in Fig. 4.2. A DDS requires a stable system clock to drive the address counter. Sometimes there is a need for an external reference clock, which allows for the system clock to be phase locked with other devices and can improve phase noise characteristics. Any instability in the reference clock leads to phase noise on the DDS output signal [70], so choosing a stable reference is a requirement for the DDS

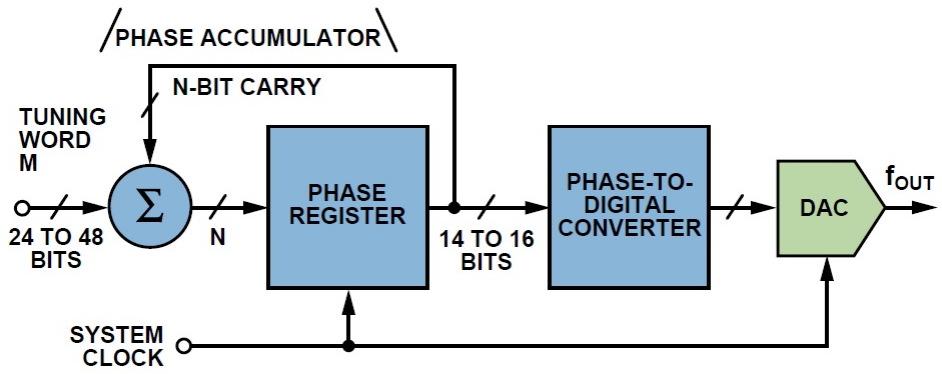

Figure 4.3: A block diagram of a commonly used DDS scheme. Reprinted with permission from [10]. Copyright (2012), Analog Devices Inc.

output to be phase stable. The sine lookup table contains digital amplitude information for a full cycle of a sine wave in individual memory locations. The lookup table may contain amplitude information for any arbitrary waveform, but a sine wave was chosen for simplicity of this example. For every clock cycle, the address counter sequentially steps to the next memory address. The digital amplitude information in this address is then sent to a digital-to-analog converter (DAC), which converts the digital amplitude information into an analog amplitude. The output from the DAC is then passed through a low-pass filter. This low-pass filter is primarily used to suppress noise (image frequencies) introduced by aliasing [10]. Since the DDS relies on sampling the lookup table, it suffers from all the issues that arise from sampling including the previously mentioned aliasing, quantization noise, etc. [70]. The simplicity of this example makes it easy to understand the theoretical principles of a DDS; however, it does not lend itself to being a good configuration of a DDS in practice. The simple model suffers from the issue that to change the output frequency, f_{out}, either the sine lookup table has to be changed or the clock frequency, f_C, has to be adjusted. Thus a more advanced scheme is needed since these two operations are not convenient in real-world applications. One such scheme is shown in Fig. 4.3. The three main components are the phase accumulator, the phase-to-digital converter and the DAC. The phase accumulator plays the role of the address counter controlling the sampling of the sine lookup table (implemented by the phase-to-digital converter). The phase register contains a digital value of the current phase of the waveform (from $0° - 360°$). For each clock pulse, the phase accumulator adds the frequency tuning word to the previous phase register value. The new value is then truncated and sent on to the phase-to-digital converter. This truncation of the phase value (usually $10 - 22$ bits) is done to reduce the size of the lookup table while avoiding any loss in frequency resolution [70]. The value of the frequency tuning word is set by the user and can be easily adjusted. By varying this tuning word the output frequency of the DDS can be adjusted. This can easily be seen in Fig. 4.4. As the phase

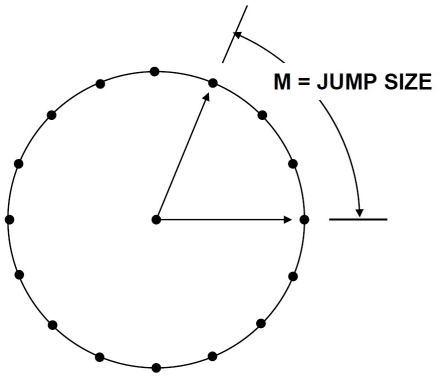

Figure 4.4: A visual representation of how the phase register advances with each clock cycle. Once around the circle corresponds to one complete cycle (i.e. $0^o \rightarrow 360^o$). The jump size M is set by the frequency tuning word. Reprinted with permission from [70]. Copyright (2009), Analog Devices Inc.

step size M (ie. the tuning word), is increased, the output frequency is also increased. The resolution of the phase accumulator determines the frequency resolution of the DDS. The resolution of a DDS is given by the following equation

$$f_{Resolution} = \frac{f_C}{2^N}, \tag{4.1}$$

where N is how wide the phase accumulator is in bits. Most DDSs have a phase accumulator between 24 and 32 bits wide [70]. The output frequency, f_{out}, is given by

$$f_{out} = \frac{M \cdot f_C}{2^N}. \tag{4.2}$$

If one wishes to change the output frequency of the DDS, all one has to do is change the tuning word. Since this change will be immediately seen on the output of the DDS, ignoring the time to programmatically implement the change, the phase of the DDS is said to be *phase-continuous* [10] (i.e there is no sudden jump in the output waveform). The phase-to-digital converter contains the lookup table for the given waveform that is to be synthesized. It is common practice not to store the full 360 degrees of phase-amplitude information to limit the amount of memory needed by the lookup table. For example, a sine wave will only contain 90 degrees of phase-amplitude information due to a sine wave's inherent quadrature nature (i.e. it appears to have the same shape repeating every 90 degrees) [70]. Thus in the case of a sine wave, the first two most significant bits (MSBs) contain the quadrature data. Generally, all of these different components are integrated within a single chip that is surface-mounted onto a printed circuit board (PCB). A synthesizer is considered to be agile if the synthesizer can switch between different frequency profiles quickly. A DDS is digital, which allows it to switch between different profiles quickly - within a few clock cycles -

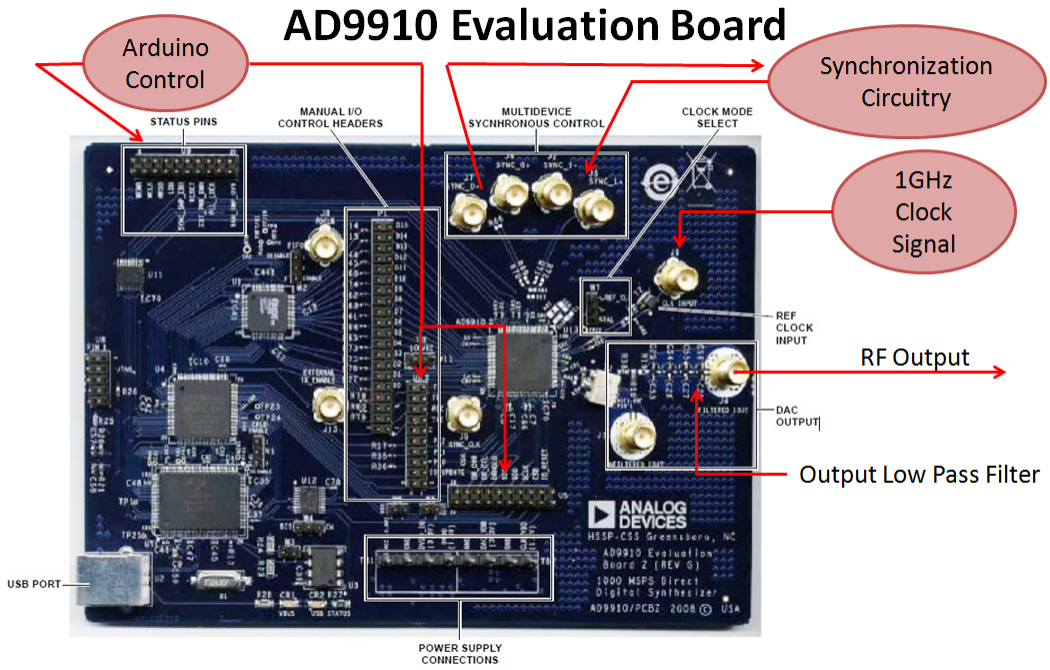

Figure 4.5: A picture of the AD9910 evaluation board. Modified with permission from [13]. Copyright (2010), Analog Devices Inc.

using digital processing, making a DDS very agile. Furthermore, the number of profiles one device can contain is purely limited by the amount of memory within the device.

4.5 Multi-Channel Direct Digital Synthesizer Design

At the heart of our Multi-Channel Direct Digital Synthesizer are four AD9910 development boards (see Fig. 4.5). Each board consists of an AD9910, interface electronics and a low-pass filter on the RF output. The AD9910 is a surface-mount DDS core, which contains eight frequency profiles in its memory. Each profile contains its own frequency, phase, and amplitude information that the DDS can express on its output. There are two ways of interfacing with the AD9910, both of which are available on the evaluation board. The first way is via parallel communication. This allows for full fast control for example via an FPGA interface card, as seen in the systems designed by the previously mentioned groups [36, 52]. In this case, the FPGA provides the memory to store the various synthesizer profiles and the large number of pins to drive the parallel interface. The second way is SPI three-wire programming of (an albeit limited number of) profiles saved in the AD9910's DDS core together with fast switching between them via three dedicated profile switching inputs. By using a development board, it eliminates a lot of the hardships that come from not only assembling surface-mount components but also eliminates having to worry about satisfying timing and RF circuitry requirements for on-board components.

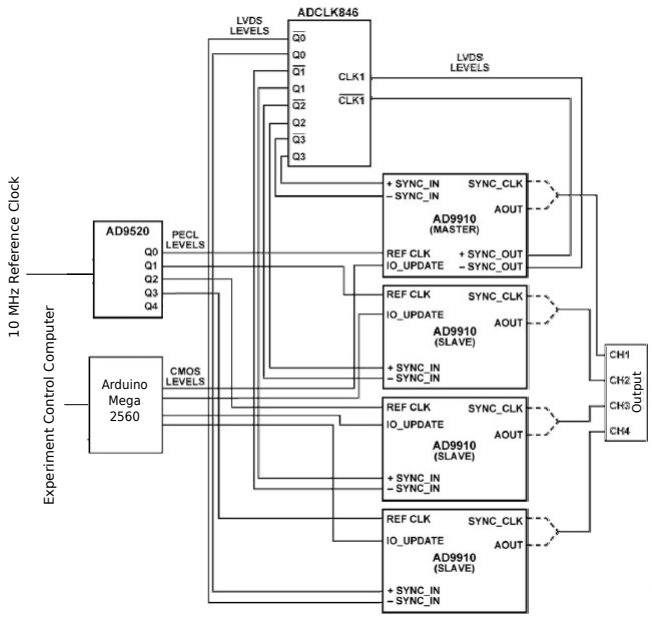

Figure 4.6: A block diagram of the synchronization circuitry setup used for our Multi-Channel Synthesizer. Modified with permission from [15]. Copyright (2009), Analog Devices Inc.

For the Raman laser beams, the AOMs operate near 200 MHz; thus, the AD9910 was chosen to satisfy this need. The AD9910 has a system clock of 1 GHz, which gives it an output of up to 500 MHz without much spurious noise [14]. A set of four synthesizers should be sufficient for the immediate needs in the experiment. Figure 4.6 shows the basic design adapted from [15] for a four-channel system, which is phase locked to a 10-MHz reference and phase synchronized between channels. The 1-GHz reference signal for the AD9910 is provided by an AD9520 development board. All four DDS development boards are directly clocked by the 1-GHz external clock provided by the AD9520 development board. The AD9520 is phase locked to a 10-MHz external frequency reference used by the other lab equipment in the experiment. Since the AD9520 has multiple outputs that are phase aligned, there is no need for a clock distribution board. The AD9520 is programmed via USB using the provided software from Analog Devices. The settings used by the AD9520 are programed only once during system initialization.

The outputs from all four of the evaluation boards must be synchronized for full system capabilities. The AD9910 evaluation board has built-in synchronization circuitry (shown in Fig. 4.5). The synchronization circuitry operates by designating one board to act as the *master*, and the other three boards to act as the *slaves*. The master board outputs a square-wave signal that is $\frac{1}{16}$ the frequency of the system clock (62.5 MHz for a 1-GHz system clock). This signal is then fanned out to the slaves and back to the master (see Fig. 4.6). Given

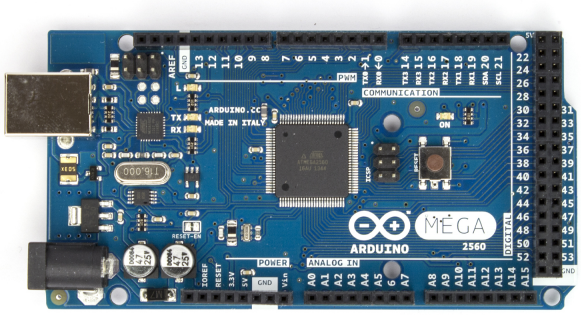

Figure 4.7: An image of the Arduino Mega 2560 micro-controller. Reprinted under Creative Commons license from [41].

that all boards share the same synchronization parameters and edge-aligned reference clock signal, then one can say that the internal clock states are synchronized.

All synchronization connections should have length-matched cables to prevent any phase delays within the circuit. However if the cables are not perfectly matched (manufacturing margins of error), then the AD9910's synchronization circuitry offers the ability to introduce delays on both the output of the synchronization signal as well as the input of the synchronization signal. These delays are controlled by user defined registry values and can be added in increments of ∼150 ps. While this synchronization circuitry does guarantee a synchronized clock state, this does not guarantee that two boards will have phase aligned outputs. For phase aligned outputs, the phase accumulator of both devices must also be synchronously cleared via the serial update input (called an *I/O Update*). Both devices must receive this I/O update pulse within the same Sync_Clk period (Sync_Clk should not be confused with the synchronization signals). Sync_Clk is what the device uses to internally time serial communication as well as other control functionalities. Sync_Clk is derived from the system clock and is $\frac{1}{4}$ the system clock's frequency. The serial programming and synchronization will be discussed further in Sec. 4.7.1.

4.6 Arduino Interface

The AD9910 evaluation board comes with open-source software that is adequate for basic testing purposes; however, the USB interface hardware on the development board does not allow addressing of the profile switching pins through an external system such as our experiment control computer. Thus, there is a need to take full control of the development board with an external interface device. As discussed in Sec. 4.5, one scheme of interfacing with the AD9910 development board uses three-wire SPI communication. In addition to SPI communication, the interface device also has to send various digital control signals

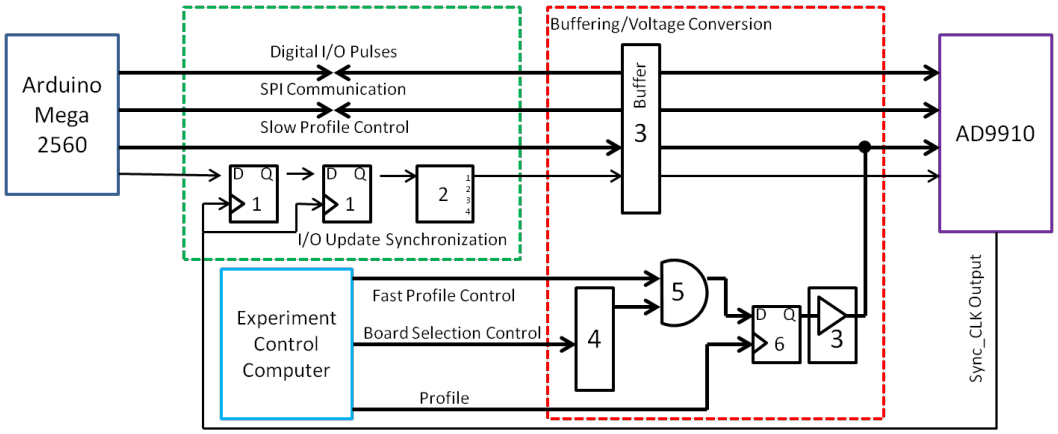

Figure 4.8: A block diagram of the circuitry used to control a single AD9910. The numbered components are given in Table 4.1.

to the AD9910. For four development boards this requires the device to have a sufficient number of digital pins. The National Instruments' USB8451 SPI controller, which was used in earlier stages of this project in our group, does not meet the pin-count needs for the new system design. An Arduino micro-controller was chosen as an inexpensive alternative to meet this need. The Arduino also has support for LabView, which will theoretically allow for easy integration with the LabView program that runs the experiment.

Figure 4.7 shows the Arduino Mega 2560 micro-controller that is used in this project and that is a favourite with hobbyists and amateur robotics designers. The Mega 2560 provides several features including 56 digital I/O pins, community-developed LabView VI libraries and low cost. The Arduino is interfaced to the computer via a USB connection. The Arduino is responsible for the "Slow Control" of the AD9910 Evaluation Boards as described above. The LabView VI Library used to communicate with the Arduino is called *Lynx*, which was independently developed by a National Instruments software engineer. The VIs provided in the Lynx library issue commands to the Arduino that it in turn executes. The Arduino is loaded with a custom firmware that is constantly checking for new commands from LabView and acting on them once they are received. The Arduino interfaces with the AD9910 evaluation boards via its digital I/O pins, which are accessed conveniently through a daughter board, which was designed to be a breakout board for ribbon connectors. To interface with four AD9910 evaluation boards, there are 46 digital I/O pins needed, which are for serial communication and digital control pulses. Since the AD9910 evaluation board utilizes 3.3-V logic (CMOS) whereas the Arduino utilizes 5-V logic, a buffer board was designed to provide not only 3.3 V to 5 V conversion (and vice versa) but also buffering of the inputs/outputs of both devices. There are also some chips on the buffer board that provide logic NOT and AND gates to provide the AD9910's required logic levels. Figure 4.8 shows the block diagram of the circuitry used to control a single AD9910 within the current system design. The components used in the circuitry are listed in

Component #	Component Type	Part Number
1	D-Type Flip Flop	ALVC574
2	1:4 Fanout	551MLF
3	Octal Buffer/ Driver	SN74LVC244AN
4	Demultiplexer	SN74AHC139
5	AND Gate	SN74AHC08N
6	D-Type Flip Flop	SN74LVC374AN

Table 4.1: A table of the components used for the Arduino-AD9910 interface shown in Fig. 4.8.

Table 4.1. The signals from the Arduino are all passed through buffer chips (component (3) in Fig. 4.8). The I/O update synchronization is handled by a D-type flip-flop synchronizer with a fan-out chip to distribute the synchronized I/O update to the four AD9910s. A D-type flip-flop synchronizer, utilizing two back-to-back D-type flip-flops, will synchronize the pulse at the input of the first flip-flop with the clocking signal provided to both D-type flip flops [47]. In this case the clocking signal is the Sync_CLK provided by one of the AD9910s. Therefore the timing of the I/O update signal relative to the Sync_CLK signal can be kept constant, which provides a necessary requirement for generating phase-aligned RF outputs from the four boards, as discussed above. When choosing the components for this I/O update synchronization circuit, one must be careful that the total delay in the I/O update synchronization circuit is not a multiple of the sync clock period to avoid ambiguity of the I/O update pulse being expressed by the AD9910s. The board selection circuitry in Fig. 4.8 allows the experiment control computer to activate profiles stored on any one of the AD9910 boards. A D-type flip flop is used in this circuitry as primitive memory for the fast profile switching while a demultiplexer is used to reduce the hardware requirements for addressing four AD9910 boards. As shown in Fig. 4.8, the AD9910's profiles can be chosen both by the experiment control computer or the Arduino; however, when integrated with the trapped ion experiment, the fast control will be primarily used.

4.7 Serial Programming and LabView Code

4.7.1 Serial Peripheral Interface (SPI)

There are several different schemes for serial programming. The scheme used by the AD9910 DDS chip is SPI, which uses a master/slave structure where the Arduino acts as a master and the AD9910 acts as a slave. SPI communication can be run in either two-wire or three-wire mode. In two-wire mode, receiving and sending information is done using the same digital pin. In the three-wire mode used in our design, sending and receiving information is done on two separate digital pins. In a system with multiple slave devices there is also

a need for there to be a dedicated slave-select (chip-select) line for each slave device. Thus there are generally four pins needed on each slave device for SPI communication: master-out slave-in (MOSI) for master-to-slave communication, master-in slave-out (MISO) for receiving information from the slave, serial clock (SCLK), and slave select (SS). The serial clock pin is used by the master device to send the communication clock cycles to the slave devices to maintain synchronization during communication. In our DDS system, our master (which is the Arduino) provides three dedicated SPI lines fanned out to the various DDS boards and provides a separate slave select for each board.

The structure of an SPI communication sequence can be broken down into two main parts: the communication instructions and the information being transmitted. For our AD9910 and Arduino pairing, the communication instruction byte is fairly simple. The most significant bit determines whether the communication cycle will be a read or a write operation. The next two most significant bits are filler and do not contain any instructions. The last 5 bits contain the registry address that will be written to or read from on the AD9910. When a write sequence is selected, the AD9910 takes the information stream and places the information into its serial buffer. The serial buffer is basically a temporary storage location for information before it gets shifted out to the AD9910's registries. Once a pulse comes in on the AD9910's *I/O Update* pin, the information gets shifted out from the buffer and into its intended registry location. With the AD9910, the number of bytes sent during a write operation must *exactly* match the number of bytes in the registry that is being written to. If the number of bytes do not match, the AD9910's serial port controller will be out of sequence for the next write operation (unless a reset is performed). During a read operation, the AD9910 will shift out the bytes of the chosen register during the information transfer part of the communication cycle.

4.7.2 LabView Code

Figure 4.9 shows the LabView *block diagram* of the program controlling the Arduino that interfaces with the AD9910 development board. A LabView program is known as a *Virtual Instrument* or VI for short. The VIs utilized by *Lynx* for Arduino control use hexadecimals and SCPI (Standard Commands for Programmable Instruments) to control the Arduino.

The LabView program that runs the Arduino interface is comprised of two main components. The first main component (contained within the flat sequence structure) is comprised of a sequence of sub-VIs that set up and configure both the Arduino and the AD9910. This sequence is only run once at system start-up and configures the AD9910 for unsynchronized operation. The second component of the program is the main program loop. Within this while loop there is an event structure for controlling the AD9910 through the front panel (see description in the next section). This while loop controls the digital pulses that run the AD9910 and program its control registries. The control registries contain the settings used by the AD9910 like the power-down settings. The programming sequence shown in Fig. 4.9

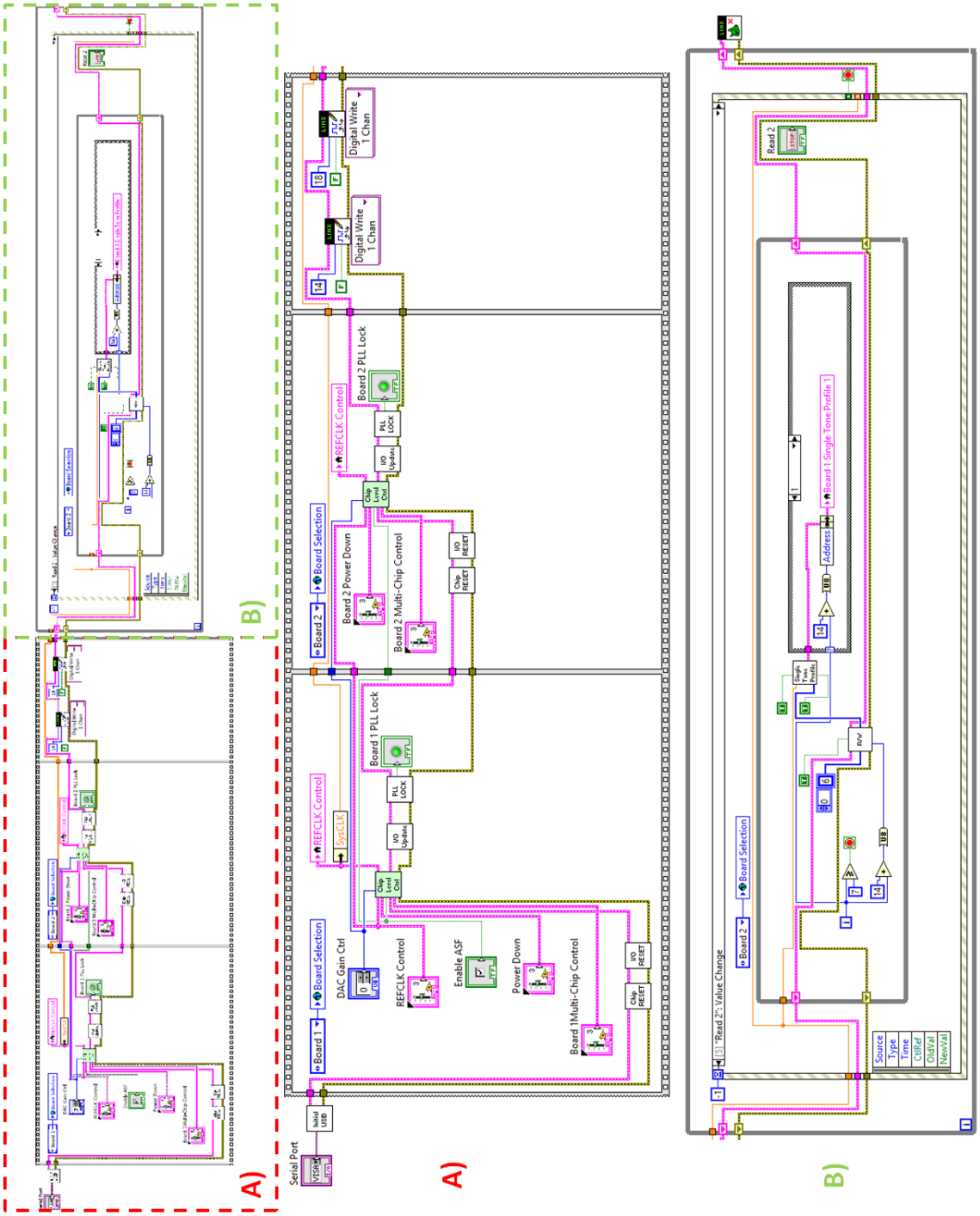

Figure 4.9: A screen capture of the LabView DDS program's block diagram. The event structure shown is a read command for the AD9910 development board. The structure is executed whenever the read button is pressed on the front panel shown in Fig. 4.10.

updates the control registries of the AD9910 whenever there is a change on the front panel for the Multi-Chip Control or the Accumulator Control. There are similar sequences that perform operations for other registries like changing the frequency, phase, or amplitude of a frequency profile.

The basic program structure used for the Arduino/AD9910 LabView interface program was created by my predecessor Jixin Liang to interface an NI8451 and the AD9959 DDS development board. However, most of the previous sub-VIs required modification due to the programming differences between the NI8451 and the Arduino Mega 2560.

4.8 User Interface

As previously mentioned, a LabView VI is used as the software that controls the operations of the four DDS development boards through the use of an Arduino that acts as an SPI and Digital I/O interface device. The user interface for a LabView program is provided by the *front panel*. The front panel is where multiple controls and indicators are located for the various variables in the LabView VI.

The front panel used to control two AD9910 evaluation boards can be seen in Fig. 4.10. On the front panel, the control groups (controls within an indented section) and buttons serve to access the control registries of the AD9910. For two boards this layout is sufficient to operate two AD9910 development boards; however, for four development boards a stacked control front panel will provide a much tidier user interface. Frequency profiles can be written, read, and accessed, as can other control functions like the power-down controls. Several of these control groups will not be available for the user to adjust when the final version of the system is integrated with the trapped ion experiment like the *REFCLK Control* and the *Multi-Chip Control*. These controls were made available on this iteration of the LabView program for testing purposes.

Basic Control Instructions

The basic steps needed to program and enable the use of a single AD9910 were expanded from earlier software versions to work with multiple development boards. The operation of the current two-board setup is straight-forward and requires little knowledge of the appropriate settings needed to use the AD9910. The power-down parameters, communication parameters (like enabling three-wire SPI communication), and clock parameters are all default values that are set as part of the initialization of the LabView program. However, during the operation of the devices, if a user needs to adjust any of the parameters set during initialization, except the SPI parameters, then those parameters can be freely adjusted from the front panel. Once the initialization has been completed, the frequency, phase, and amplitude information can be entered into the profiles. Once all the profile information has been entered, the profiles can be selected by choosing the bubble beside the profile the user

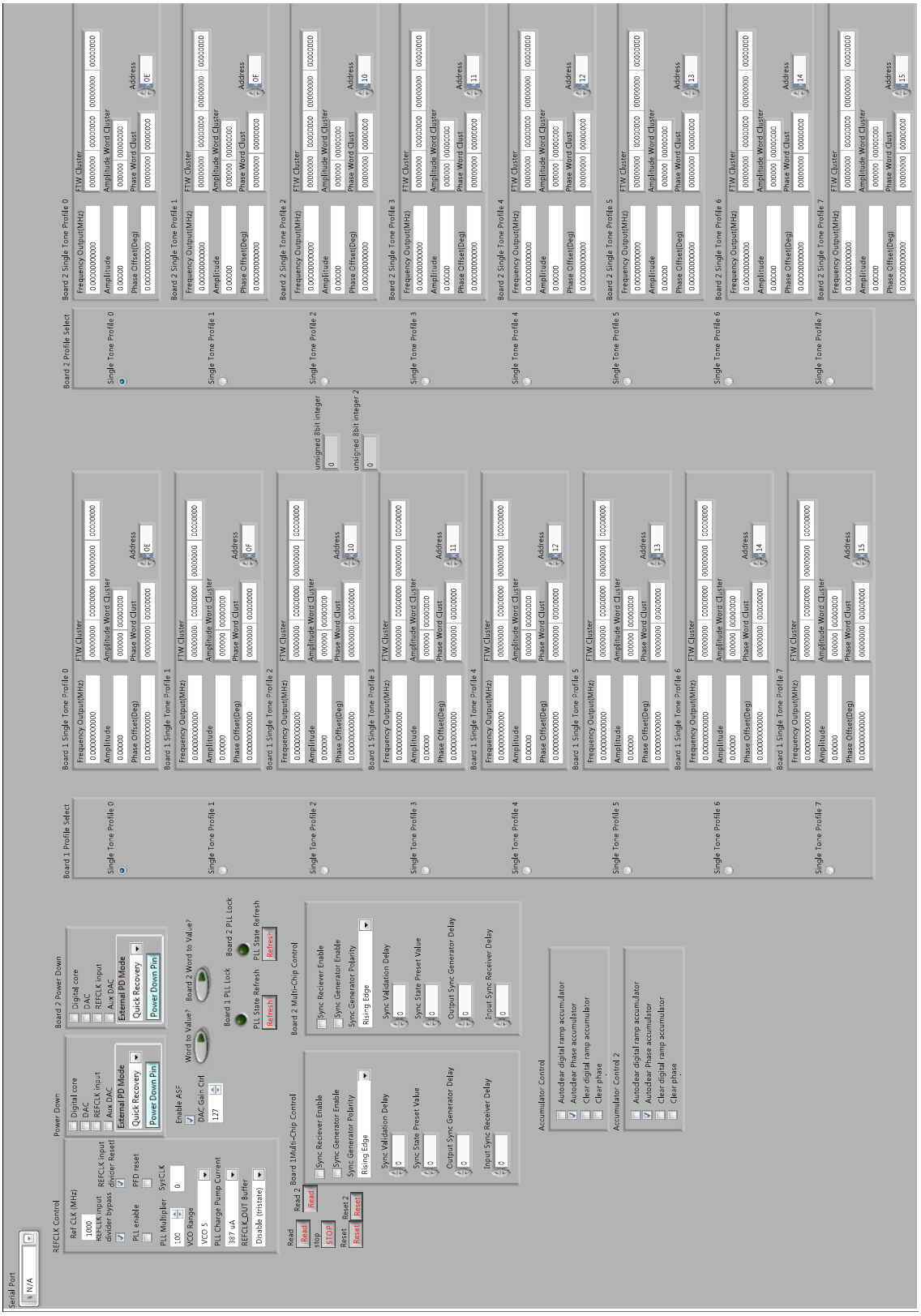

Figure 4.10: A screen capture of the LabView DDS program front panel.

wishes for the AD9910 to output. If the user is using multiple boards, then the user must adjust the Multi-Chip control to activate the multi-chip synchronization by selecting "Sync Receiver Enable" and "Sync Generator Enable" on the master board and "Sync Receiver Enable" on the slave boards.

Remote Interface

The above discussion has described the manual front-panel control, but this will ultimately need to be integrated with the trapped-ion control setup. The trapped-ion experiment program is in LabView, which would make integrating the Arduino interface with the experiment program relatively straightforward in principle. However, an alternative method which mirrors the current GPIB interface used by the other synthesizers (and which has some advantages as discussed below) would be a remote interface between the experiment control computer and a stand-alone computer controlling the Arduino. This was demonstrated in principle via a TCP (Transmission Control Protocol) connection.

TCP uses a "client" and "sever" based setup to communicate between networked computers. The server computer waits for incoming connection requests from the client computer. Data is then sent back and forth between the client and server computers until the connection is closed. For the Arduino interface the computer that controls the Arduino would act as the server computer and the computer that would remotely control the Arduino interface would be the client computer. For testing purposes the computer controlling the Arduino was connected to the client computer with a physical connection via a router. The client computer was running a simple LabView program that sends simple command strings to the server computer. The server program was a modified version of the Arduino interface with a special front panel control to switch between remote or local control. The server program in remote mode parses and acts upon incoming command strings. This test setup lacked two-way communication but in principle this would be a simple addition. Two-way communication would allow the Arduino interface to relay its current settings to the server computer as well as the Arduino interface's current error state.

4.9 AD9910 Performance Characteristics

Separate from interface issues, a few preliminary tests were performed to determine if the RF output from an AD9910 development board is suitable for our needs. The first two tests discussed below, relating to output amplitude flatness and spurious spectral features, are motivated from prior experience with an AD9959 evaluation board. For the tests on spurious spectral features and narrowband phase noise, the performance characteristics of the AD9910 evaluation board are also compared to those of an HP 8642A synthesizer. The HP 8642A is currently used in our lab for driving Raman transitions.

4.9.1 Low-Pass Filter Response of the AD9910 Development Board

The transfer function of the low pass filter included on the AD9910 evaluation board was measured and the results are shown in Fig. 4.11 as a function of the output frequency of the AD9910.

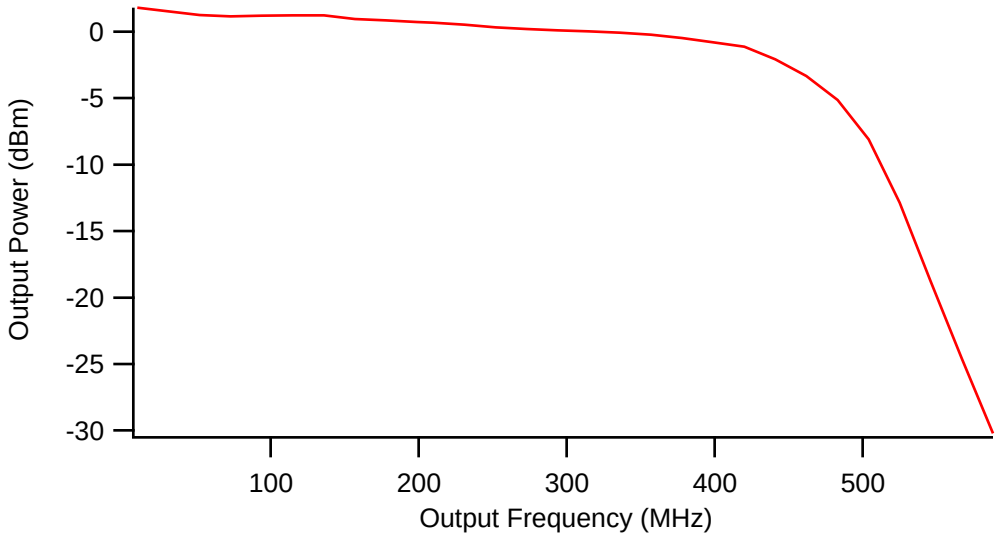

Figure 4.11: A graph showing the AD9910 evaluation board's measured power output as a function of output frequency.

The output power remains mainly flat for frequencies up to ~ 400 MHz. Therefore the 200-MHz region where the experiment operates is far away from the roll-off of the low-pass filter. One may notice that the output curve, while flat up to ~ 400 MHz, does exhibit a sloping characteristic. However, the slope is $\sim 0.0057 \frac{\text{dBm}}{\text{MHz}}$. Since our frequency scans rarely exceed a 400-kHz sweep, the power output will not vary by more than ~ 0.0023 dBm and the AOM-related variations are more important.

4.9.2 Spurious Signals

Spurious signals are an important consideration for a synthesizer that will be used for an ion trap experiment. In our lab, the bandwidth of the AOMs ($\sim$ 10 MHz) suppresses the signals outside of the operational frequency range. However, spurious signals close to the desired signal may also drive the AOMs and lead to unexpected Raman couplings. Figure 4.12(a) and Fig. 4.12(b) show the wideband spectrum of the AD9910 and the HP 8642A, respectively, acquired with a Signal Hound USB-SA44B spectrum analyzer. Both the AD9910 and the HP synthesizer have their carrier frequency set to 203.4 MHz. This frequency was chosen because it is around our normal operating frequency used in the experiment and it is not a perfect multiple of 10 MHz, which is what the HP synthesizer and DDS use as a reference. The unlabeled features seen in both wideband scans are not

real spurious features but are artifacts of the spectrum analyzer's signal processing.[1] The AD9910 does not exhibit any significant spurious signals. By comparison, the wideband scan of the previously used AD9959 DDS is shown in Fig. 4.13. The AD9959 exhibits many more (albeit relatively small) spurious features than the AD9910 due to the lower DDS clock frequency (i.e. the AD9910 is an improvement in this regard).

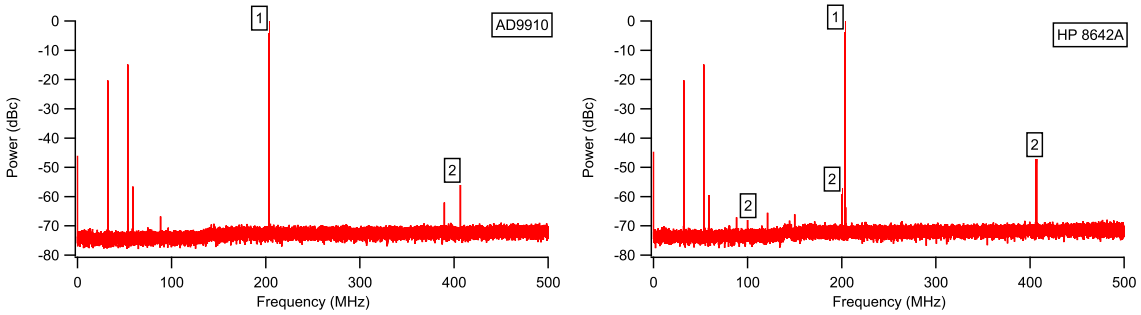

(a) (b)

Figure 4.12: Figure (a) shows the wideband spectrum of the AD9910 while Figure (b) shows the wideband spectrum of the HP 8642A generator. The main spurious signals are labeled "2" with the carrier frequency labeled as "1" in both figures. The peak seen at close to 0 MHz in both figures is simply the line noise and its harmonics. The unlabeled peaks seen in both figures are artifacts due to the spectrum analyzer used. Both scans were performed at 30-kHz resolution bandwidth and 30-kHz video bandwidth, an input power of 0 dBm, and an input frequency of 203.4 MHz.

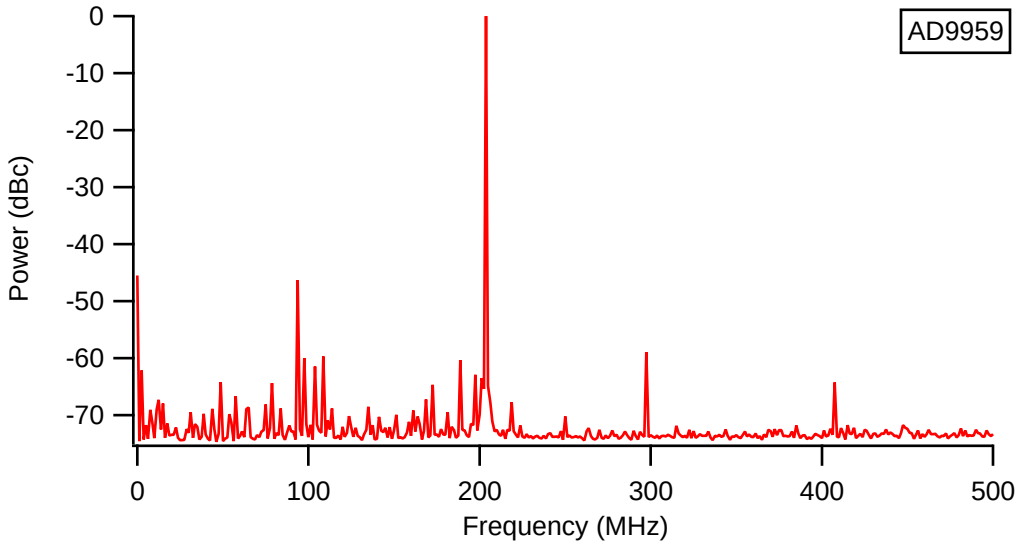

Figure 4.13: Wideband scan of the AD9959 output at 203 MHz. One can observe that there are many more spurious signals than in the AD9910 wideband scan.

[1]To verify the artifacts are indeed artifacts of the spectrum analyzer's post processing software and are not spurious features, a zoom in of each artifact was done. Once the span was less than 1MHz, the artifacts disappeared from the spectrum.

4.9.3 Narrowband Performance

Perhaps more important than the wideband performance is the narrowband performance. The narrowband spectrum considers the noise close to the carrier signal. Figure 4.14(a)

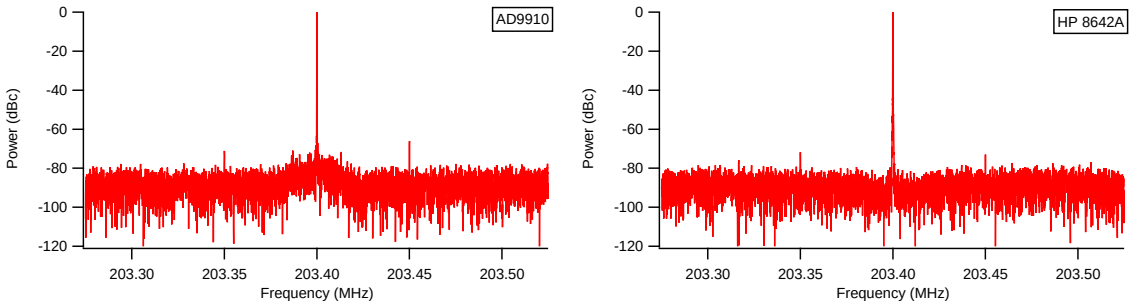

(a) (b)

Figure 4.14: Figure (a) shows the narrowband spectrum of the AD9910 at a span of 250 kHz while Figure (b) shows the narrowband spectrum of the HP 8642A over the same 250 kHz span. The resolution bandwidth and video bandwidth were both set to 100 Hz and an input power of -22 dBm was used in both (a) and (b).

and Fig. 4.14(b) show the narrowband spectrum at a span of 250 kHz for the AD9910 and the HP 8642A respectively. Both narrowband spectra appear to be fairly similar at this span. However, the AD9910 exhibits some excess broadband phase noise (~ -75 dBc) out to $\sim$ 20 kHz from the carrier signal, which is not a major issue for current experiments. Finally, Fig. 4.15(a) and Fig. 4.15(b) show the narrowband spectrum at a span of 25 kHz

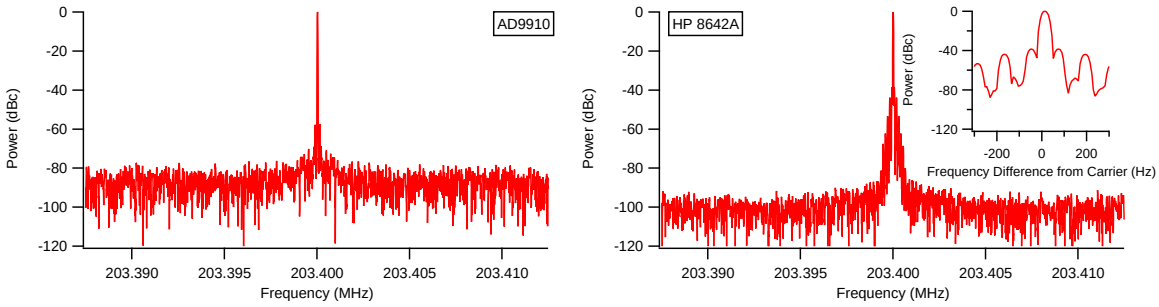

(a) (b)

Figure 4.15: Figure (a) shows the narrowband spectrum of the AD9910 at a span of 25 kHz while Figure (b) shows the narrowband spectrum of the HP 8642A at the same 25-kHz span with an inset zoomed in around the carrier frequency. In both (a) and (b), the resolution bandwidth and video bandwidth were set to 30 Hz and an input power of -22 dBm was used.

for the AD9910 and the HP 8642A respectively. Interestingly, there is a very noticeable difference between the AD9910 and the HP generator at this narrowband span. The HP signal appears to be wider than the AD9910's signal. A zoom-in of the HP generators

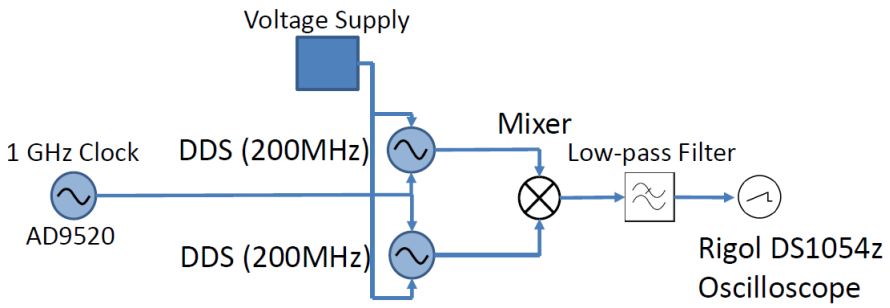

Figure 4.16: A simple block diagram showing the setup used to measure the phase stability between two AD9910s.

narrowband spectrum around the carrier signal is shown as an inset in Fig. 4.15(b). These spurious peaks appear to be caused by line noise and its odd harmonics; however, this is still within specifications for the HP 8642A. In conclusion, at least cursorily, the AD9910 appears to be suitable for use in the ion trap experiment, and does not show any dramatically poor behaviour compared to existing synthesizers in use. Additional measurements will need to be considered in the future with the final design, including online tests driving transitions in ions.

4.9.4 Relative Phase-Lock Stability

Phase stability is important to consider when coherent operations are involved in an ion-trap experiment. To assess long term phase drift between two AD9910s, they were initially phase aligned using an edge-aligned I/O update pulse applied to both AD9910s. The output from both AD9910s were then combined in a mixer. A mixer's output can be thought of as the product of the two input signals, which for cosinusoidal functions is

$$\begin{aligned} V_{Mixer} &= \alpha V_1 V_2 \cos(\omega_1 \cdot t + \phi_1) \cdot \cos(\omega_2 \cdot t + \phi_2) \\ &= \frac{\alpha V_1 V_2}{2} \left[\cos((\omega_1 + \omega_2)t + (\phi_1 + \phi_2)) + \cos((\omega_1 - \omega_2)t + (\phi_1 - \phi_2))\right], \end{aligned} \tag{4.3}$$

where α is some constant. Equation 4.3 is the general case for two different frequencies. However, in our case we are interested in relative phase stability; thus, both AD9910s were set to output the same frequency (200 MHz for this test). Therefore Eqn. 4.3 reduces to

$$V_{Mixer} = \frac{\alpha V_1 V_2}{2} \left[\cos(2\omega t + (\phi_1 + \phi_2)) + \cos(\phi_1 - \phi_2)\right]. \tag{4.4}$$

In this case we see in Eqn. 4.4 that the mixer output has a high frequency term and an approximately constant term that depends on the phase difference of the two input signals. Therefore, we used a low-pass filter to isolate the constant term.

The measurement setup is shown in Fig. 4.16. The signal from the low-pass filter was measured by a Rigol DS1054z oscilloscope and saved to a file for later analysis. The mixer's $dV/d\phi$ sensitivity was calibrated by setting one AD9910 to be a few Hertz higher than the second AD9910 and measuring the peak-to-peak amplitude of the oscillation. An overnight measurement was taken to assess the amount of relative phase drift between two AD9910 development boards. The results of this measurement are shown in Fig. 4.17. As can be seen in Fig. 4.17, the relative phase varied by less than 0.4° on either side of the initial phase alignment. This amount of phase drift is more than acceptable for our immediate needs.

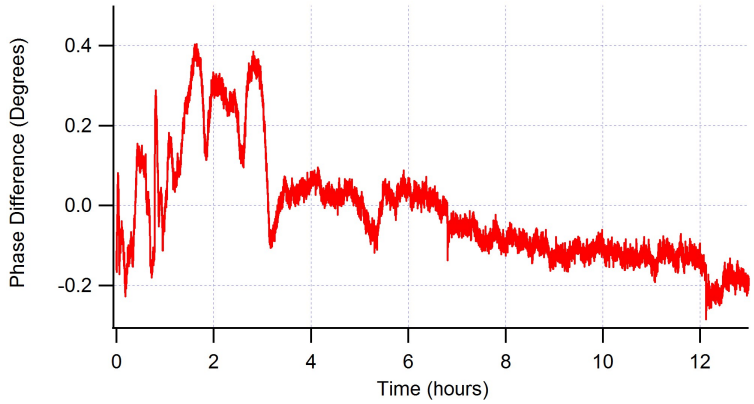

Figure 4.17: Long-term relative phase drifts of two AD9910s clocked by phase-locked clock signals. The sample rate was 0.5 s^{-1}.

4.10 Technical Issues

We conclude by addressing some of the technical issues discovered with the project. The design of the synthesizer interface as currently conceived has several technical issues that add a level of complication to the overall system design. The first issue lies with the Arduino interface to LabView. *Lynx*, the LabView VI library that interfaces LabView with the Arduino, is not an officially supported National Instruments VI library. National Instruments did create their own VI library called *LIFA* (LabView Interface For Arduino); however, it was not well supported and lacked some basic functionalities of the Arduino. The largest issue with *Lynx* is the control loop used to check for new commands from LabView. It tends to hang when the Arduino connection is closed and reopened again, as well as occasionally hanging after the firmware is loaded onto the Arduino. The only solution that fixes this is re-flashing the firmware onto the Arduino. This issue causes a problem when one wants to integrate the Arduino's LabView program with the experiment

control LabView program. Since the Arduino's LabView program will occasionally hang, the main experiment control program would have to be restarted to clear the hang if the Arduino's program is integrated into the experiment control program. This is problematic and not practical for experimental purposes. If the Arduino LabView program was operated semi-autonomously as discussed above, then only the Arduino system would have to be reset to continue operating the synthesizer, but this is probably not a long-term solution.

Another technical issue arises from the fact that the Arduino is quite "slow". The Arduino has an on-board 16-MHz crystal oscillator that it uses as its system clock. This essentially sets the time scale that the Arduino operates on (on the order of tens of nanoseconds). For the AD9910 the system executes commands using a clock (known as *Sync Clock*) with the period of four nanoseconds ($\frac{1}{4}$ the AD9910's system clock). However, due to how *Lynx* operates, commands are acted upon on the scale of tens of *microseconds*. To edge-align two AD9910s, they must receive two I/O update pulses within the same clock cycle of the sync clock. However, since the Arduino is operating on a much slower time scale a synchronization circuit is needed to send a synchronized I/O update pulse to each board. This synchronization circuit was implemented as discussed above but it adds an extra complication to the Arduino-based setup.

4.11 Future of the Project

The project has come a long way but it does have quite a ways to go before it is a "finished product." One of the next steps will need to be a version two of the buffer board and the Arduino daughter board. The buffer board will need permanent fixes for logic issues that were fixed externally for testing and will need to include a few more pieces of logic necessary for synchronized I/O update pulses. The daughter board for the Arduino will also need I/O update pulse synchronization circuitry added as well. The issue with the Arduino freezing comes down to one of design. The control loop used by the Lynx firmware is not as robust as our design needs it to be. A solution may be to change from using an LabView-based program for the Arduino to one based on the Arduino native programming language. The matter of interfacing the Arduino with the experiment's LabView program is still a technical hurdle that needs to be overcome. If Lynx is dropped as previously mentioned, one can use the Arduino as a USB or Ethernet device, which will be a much simpler interface to the experiment program.

The issue of providing synchronized I/O update pulses to all of the boards is solved by the synchronization circuit previously described; however, this is not the only solution. The Arduino could simply be put aside for a faster device that can be externally clocked. The likely candidate is the pulser board developed by Paul Pham [52] and curated currently as an open-source project[2]. The pulser board utilizes an FPGA, which is much faster than the

[2]https://sourceforge.net/p/pulse-sequencer/dds-vhdl/ci/master/tree/

Arduino. An FPGA offers many digital pins as well as excellent high-speed timing, which will allow the I/O update synchronization issue to easily be solved. Since an FPGA can be very fast, the multi-board synchronization can also be handled by the FPGA, which will eliminate the need for the additional hardware currently required to achieve multi-board synchronization in the Arduino based synthesizer design. Since the software to operate the pulser board is also open source, this will address the issue with interfacing the pulser board's software with the experiment program.

While a LabView-controlled, Arduino-based system initially appeared to offer a simpler route to interface with the AD9910 evaluation boards and can be suitable for some applications, the FPGA-based design provides a solution to the several issues currently faced by the Arduino setup. Furthermore, the hardware and software complexities of the FPGA-based design are considerably offset by the open-source project. On the hardware side, the FPGA pulser board has already been debugged and successfully used to control several DDS development boards. In comparison, our Arduino setup's hardware has yet to fully function with four boards and there still may be hidden technical issues for the project to encounter. The story is more or less the same on the software side. The pulser board offers a tested open-source software that other ion-trap groups have used to integrate the pulser board with their experimental setups. The Arduino setup still requires additional software revisions before it could be integrated with the experimental program. Thus one can conclude that the FPGA-based design represents a less complex solution with greater functionality than the current Arduino-based one. Pursuing an FPGA design will most likely be the best option.

Chapter 5

Stabilizing Secular Trap Frequencies in a Linear RF Paul Trap

5.1 Introduction

As discussed in Sec. 2.7, to be able to measure and control the quantum dynamics of the intrinsic double well near the linear-zigzag transition's critical point, a high level of control and stability is needed. In particular, 10 ppm stability in the secular trap frequencies is an initial goal to achieve a tunneling oscillation with reasonable fidelity [22]. Ideally, such stability would be maintained over a one-hour time frame for convenience of experimentation. Equation 2.4 gives an approximate relationship between a given secular frequency and the trapping parameters - trap size, trap frequency and trapping voltages. Prior work has shown that the stability of the trap RF voltage needs to be improved [22], and the stability of the DC voltages bears investigation as well. A brief discussion of improvements made to our setup in an effort to stabilize the trap potential was already given in Chp. 3, with greater detail to be provided elsewhere [77]. This chapter will focus on the measurement technique for assessing the level of stability achieved in the trap potential and the preliminary results obtained with stabilizing the ion-trap voltages.

This chapter begins with a discussion of optical Raman spectroscopy, which was used to measure the transverse and the axial secular trap frequencies. This will be followed by a description of the experimental procedure and data analysis used to obtain the measured frequencies. Next, measurements of the secular trap frequency as a function of time in the axial and transverse directions will be presented using a single trapped ion, both before and after improvements were made to correct instabilities in the trap potential. Finally, this chapter will conclude with a discussion of the next steps required to achieve sufficient

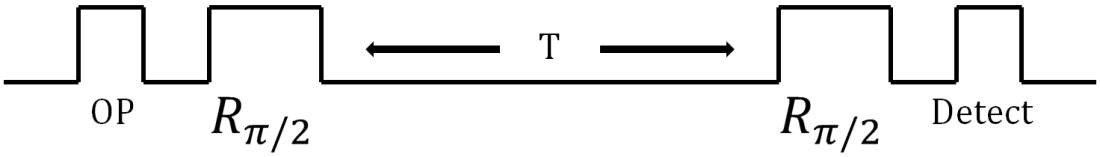

Figure 5.1: A basic diagram of the pulse sequence used for Ramsey spectroscopy of the $|\downarrow\rangle \rightarrow |\uparrow\rangle$ transition in a single trapped ion. First optical pumping (OP) is used to prepare the ion in the $|\downarrow\rangle$ state followed by two $\frac{\pi}{2}$-pulses ($R_{\pi/2}$) separated by a time T. Finally, fluorescence state detection is used to detect the ion's spin state.

stability of the trap potential in advance of the planned experiments near the linear-zigzag transition's critical point.

5.2 Secular Trap Frequency Measurement using Motional Sideband Spectroscopy

The secular trap frequencies can be measured using stimulated optical Raman transitions between spin-motion levels on the transition between $|\downarrow\rangle = {}^2S_{1/2}\,|F=0, m_F=0\rangle$ and $|\uparrow\rangle = {}^2S_{1/2}\,|F=1, m_F=0\rangle$, as discussed in Chp. 2. Specifically, the secular trap frequency for a given principal trap axis can be determined from the frequency separation between the motion-sensitive carrier transition ($|\downarrow, n\rangle \rightarrow |\uparrow, n\rangle$) at $\sim \omega_{HF}$ and the first blue sideband ($|\downarrow, n\rangle \rightarrow |\uparrow, n+1\rangle$) at $\omega_{HF} + \omega_{trap}$. To achieve the necessary measurement precision, the Ramsey technique was used [58]. The major benefit of Ramsey spectroscopy is the long interrogation times, which improve the precision of the measurement of the secular trap frequency, while effects seen in Rabi spectroscopy such as spontaneous emission and ac Stark shifts are greatly suppressed. This suppression is due to the Raman laser beams being off for most of the time in the Ramsey experimental sequence. In the following sections the simple theory of the Ramsey spectroscopic technique for a coupled two-level system (e.g. in the case of microwave coupling between $|\downarrow\rangle$ and $|\uparrow\rangle$ in a single ion) will be discussed, and then some brief comments will be made on additional effects arising in our specific application of optical Raman sideband spectroscopy of a trapped ion.

5.2.1 Basic Ramsey Theory

We consider a two-level system $\{|g\rangle, |e\rangle\}$ with coherent oscillatory coupling as introduced in Sec. 2.4. For example, we consider the case of $|g\rangle = |\downarrow\rangle$ and $|e\rangle = |\uparrow\rangle$ in a single trapped ion driven by microwaves. A basic diagram of the Ramsey experiment sequence is shown in Fig. 5.1. Ramsey spectroscopy consists of three steps: First is the state initialization via optical pumping to prepare the ion in the $|\downarrow\rangle$ state. Next is the two-pulse sequence consisting of a $\frac{\pi}{2}$-pulse to create a superposition of $|\downarrow\rangle + |\uparrow\rangle$, followed by a waiting period T that allows the ion's state to evolve freely in time, and finally after this free-evolution

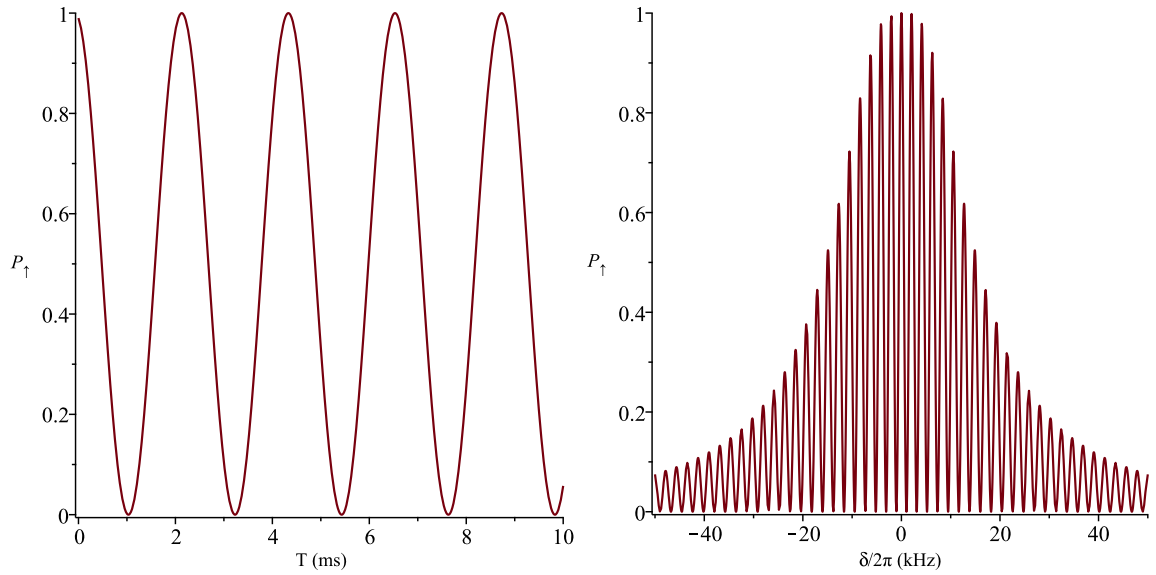

Figure 5.2: Figure (a) shows Eqn. 5.5 as the free-evolution time, T, is varied. Figure (b) shows the Ramsey lineshape from Eqn. 5.5 as the drive frequency is varied near resonance. Both figures use a Rabi frequency of $\frac{\Omega}{2\pi} = 4.55$ kHz and detuning of $\delta = 0.46$ kHz. The frequency scan has a free-evolution time of $T = 1$ ms.

period, a second $\frac{\pi}{2}$-pulse. The last step is fluorescence state detection to read out the final spin state of the ion.

The outcome of the Ramsey experiment can be calculated for a simple two-level system, as follows, for a pure initial state and in the absence of decoherence. In the reference frame rotating with the driving field (under the rotating-wave approximation), the two Ramsey pulses can be expressed as (see Sec. 2.4 for details)

$$R(\Omega,\delta) = \begin{bmatrix} \cos\frac{\theta}{2} - i\frac{\delta}{\Omega'}\sin\frac{\theta}{2} & -i\frac{\Omega^*}{\Omega'}\sin\frac{\theta}{2} \\ -i\frac{\Omega}{\Omega'}\sin\frac{\theta}{2} & \cos\frac{\theta}{2} + i\frac{\delta}{\Omega'}\sin\frac{\theta}{2} \end{bmatrix}, \tag{5.1}$$

where $\theta = \Omega' t$ contains the dependence on the pulse time, $\Omega' = \sqrt{|\Omega|^2 + \delta^2}$ is the generalized Rabi frequency, $\Omega = |\Omega| e^{i\phi}$ is the Rabi coupling including the phase of the driving field, and $\delta = \omega - \omega_o$ is the detuning. The two "$\frac{\pi}{2}$-pulses" in a typical Ramsey setup correspond to $\theta = \frac{\pi}{2}$ on resonance ($\delta = 0$). The free-evolution matrix in the frame rotating with the driving field is given by

$$F(T) = \begin{bmatrix} e^{\frac{i}{2}\delta T} & 0 \\ 0 & e^{-\frac{i}{2}\delta T} \end{bmatrix}. \tag{5.2}$$

The final state for the Ramsey experiment is given by

$$|\psi_f\rangle = R(\Omega,\delta)F(T)R(\Omega,\delta)\,|g\rangle\,, \tag{5.3}$$

where the phase of the driving field is taken to be the same for the two Ramsey pulses for simplicity. Therefore one can determine the probability of transitioning from the ground state to the excited state from the expectation value as follows:

$$P_e = |\,\langle e|\,R(\Omega,\delta)F(T)R(\Omega,\delta)\,|g\rangle\,|^2. \tag{5.4}$$

The value of P_e is independent of ϕ; therefore, the Rabi frequency, Ω, is taken to be real ($\phi = 0$) for simplicity in subsequent expressions. Nevertheless, the result from Eqn. 5.4 is in general quite complicated. If we consider the special case of $\Omega t = \frac{\pi}{2}$ (i.e. $\frac{\pi}{2}$ on resonance), we find that Eqn. 5.4 can be expressed as

$$P_e(\delta,T) = \frac{\Omega^2}{\Omega'^4}\left(\delta^2 - \delta\Omega'\sin(\delta T) + \Omega^2\cos^2(\frac{\delta T}{2})\right). \tag{5.5}$$

In the limit where the detuning is small ($\Omega \gg \delta$), Eqn. 5.5 reduces to

$$P_e(\delta,T) \approx \frac{1}{2}\left(1+\cos\left(\delta T\right)\right), \tag{5.6}$$

where the free-evolution time, T, is typically much longer than the pulse time ($T \gg t$). Figure 5.2 shows a plot of Eqn. 5.5 for the typical parameters encountered in our experiment. In Fig. 5.2(a), the oscillations with T occur at frequency $\sim \delta/2\pi$ as expected from the dependence in Eqn. 5.6, and the resolution improvement is easy to see in the spectroscopic lineshape in Fig. 5.2(b). The overall envelope of the lineshape is due to the $\pi/2$-pulse width, and the narrow fringes are separated by $\sim \frac{1}{T}$.

5.2.2 Extension of Ramsey Theory to Two-Photon Raman Sideband Transitions

We now briefly highlight several effects beyond the above theory that arise in the Ramsey spectroscopy of a motional sideband transition using a two-photon Raman technique. In order of presentation below, we discuss the ac Stark shift due to the Raman laser beams, the distribution of initial motional states following laser cooling, and motional decoherence.

The Raman laser beams create a residual ac Stark shift that affects the resonance of the blue sideband transition [75]. One advantage of Ramsey spectroscopy over Rabi spectroscopy in this case is that the resonance measured with Ramsey spectroscopy is largely insensitive to the ac Stark shift; however, it does affect the Ramsey lineshape [31], which complicates the location of the resonance. The effect of the ac Stark shift, δ_{ac}, can be accounted for in the theory of the previous section by replacing δ with $\delta - \delta_{ac}$ in the Rabi rotation shown in Eqn. 5.1 (i.e. $R = R(\Omega, \delta - \delta_{ac})$). This leads to a shift in the

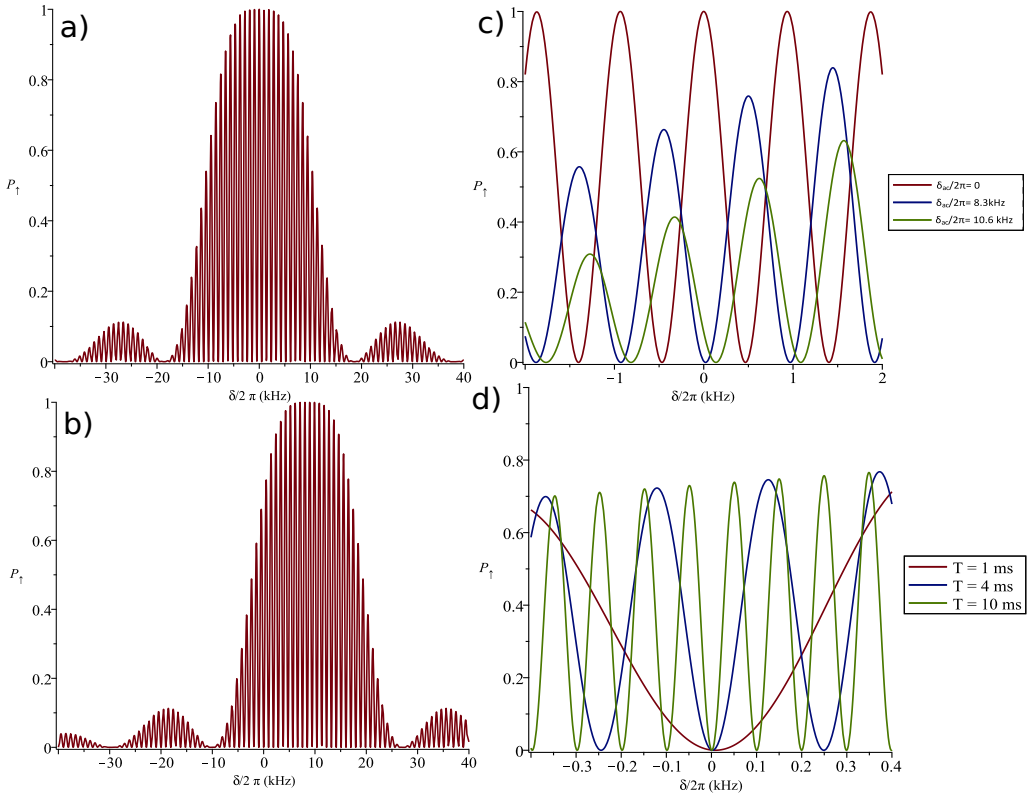

Figure 5.3: Calculated effect of the ac Stark shift on the Ramsey line shape for an optical Raman transition. (a) Ramsey line shape with no ac Stark shift. (b) Ramsey line shape with an ac Stark shift of $\delta_{ac}/2\pi = 8.5$ kHz, showing a shift in the center of the envelope from resonance. (c) Horizontal shift in the Ramsey fringe pattern near resonance for three values of δ_{ac}. All plots with a free-evolution time of $T = 1$ ms. (d) Ramsey fringe pattern near resonance for three typical free-evolution times and with typical ac Stark shift, $\delta_{ac}/2\pi = 8.5$ kHz, in the experiment. Note the same value of $P_\uparrow$ on the resonance for all T, and the shift of the pattern to near a minimum on resonance. All plots have a Rabi frequency of $\Omega_o/2\pi = 4.8$ kHz.

center of the envelope of the Ramsey fringe pattern from resonance (compare Fig. 5.3(a) and 5.3(b)) since the Ramsey rotation pulses are tuned to the ac Stark shifted resonance ($\delta = \delta_{ac}$). Thus the fringe contrast is reduced near $\delta = 0$ and the shift in the envelope center also results in a contrast gradient around $\delta = 0$. In principle, the full contrast can be recovered by measuring a Ramsey fringe a known integer number away from resonance, but the resonance location then acquires a dependence on the stability of the clock determining the Ramsey time, T, according to $\Delta\delta = \delta_{ac}\ \Delta T/T$. In our experiment, the timing board's internal clock is specified at 100 ppm, which would give drifts of $\Delta\delta/2\pi \sim 1$ Hz. Since the internal clock cannot be externally referenced, we avoid T-sensitivity by measuring the Ramsey fringe near resonance.

The ac Stark shift also leads to a horizontal shift of the fringes under the envelope, where the shift as a fraction of the fringe period depends on the ratio δ_{ac}/Ω_o (see Fig. 5.3(c) and

Fig. 5.3(d)). In the end, however, for the tests of interest here we are not concerned with the accuracy of where the resonance is but rather its stability. To understand the stability theoretically, we consider the effect of variations in the ac Stark shift on the resonance for typical experimental parameters. Given a pessimistic 10% variation in laser intensity on the ion, the Ramsey fringe pattern near the resonance is shifted over a range of ~ 40 Hz for $T = 1$ ms and ~ 11 Hz for $T = 4$ ms. This places a lower limit on the sensitivity of our resonance measurements, that is, an upper limit on the stabilities that can be measured. The effect of this limitation can be reduced by using a longer free-evolution time T, or ultimately by detuning the Raman beams further to reduce the ac Stark shift.

In experiments discussed in this thesis where the trapped ion is Sisyphus laser cooled [24, 22], the initial motional state is not in a pure state but rather a thermal distribution of motional n-levels with $\bar{n} \sim 1 - 2$, which leads to a number of consequences. First, the Raman Rabi frequency has a dependency on the initial motional state $|n\rangle$ of the ion [75]. The effect of the Ramsey pulses, given by the Rabi rotation R in Eqn. 5.1, is therefore n-dependent, and in particular it is not possible to have a perfect $\frac{\pi}{2}$-rotation for all values of n. As a result, the contrast of the Ramsey fringes will always be less than unity for $\bar{n} \neq 0$, even at short times where decoherence effects are negligible. From simulations, the short-time contrast is expected to be ~ 0.8 for the typical value of $\bar{n} = 1 - 2$ in our experiment. At longer times, the contrast will decrease due to decoherence sources such as motional heating, interferometric instabilities between the Raman beams, and spontaneous emission from leakage light [33, 69]. From the theory of [69], a rate of heating for the transverse center-of-mass (COM) mode of $\dot{\bar{n}} = 15$ s^{-1} for our trap [22] gives an expected decrease in contrast by 50% after $T \approx 20$ ms. This places a rough upper limit on possible free-evolution times, T, in our experiment.[1]

5.2.3 Measuring Secular Trap Frequencies

This section will provide a brief overview of the procedure and considerations for measuring the secular trap frequencies with a single trapped ion. Typically before data collection, the experimental procedure consists of optimizing the alignment on the ion of the laser beams, such as the Raman beams and the Sisyphus cooling beams. This is performed *in situ* by measuring the ac Stark shift induced on the $|\downarrow\rangle \rightarrow |\uparrow\rangle$ transition. Discriminated detection efficiencies, $\zeta_\downarrow$ and $\zeta_\uparrow$ for $|\downarrow\rangle$ and $|\uparrow\rangle$ respectively, are measured for later use in data analysis, and the Sisyphus cooling performance is checked.

The experimental sequence for Ramsey spectroscopy consists of 6.6 ms of Doppler cooling, 6 ms of Sisyphus cooling, spin-state initialization to $|\downarrow\rangle$ with 50 μs of optical pumping, followed by the Ramsey sequence, and 0.4 ms of fluorescence state detection. The duration of the Ramsey pulses is dependent on the Raman transition being used and must also be

[1] The signal-to-noise ratio would also figure into the ultimate limiting factors on the usable Ramsey times.

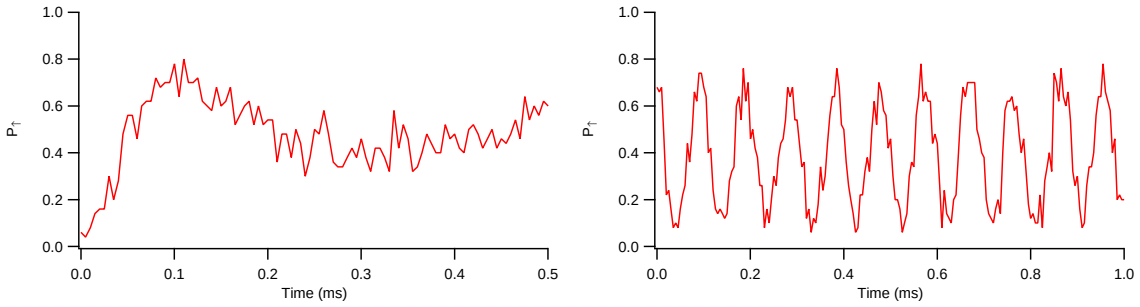

(a) (b)

Figure 5.4: (a) Rabi flopping on resonance for the transverse blue sideband with typical π-time for the transverse blue sideband of ~ 110 μs. (b) Ramsey oscillations as a function of free-evolution time for the transverse blue sideband at the Rabi resonance. The ac Stark shift due to the Raman laser beams is found from this time scan according $\delta_{ac}/2\pi = \frac{1}{\tau_{2\pi}}$. Both scans were performed with averaging of 50 experiments per point, a step size of 5 μs, detection efficiencies of $\zeta_{\downarrow} = 0.075$ and $\zeta_{\uparrow} = 0.93$, and $\bar{n} \approx 1 - 2$.

appropriately set. The first step for measuring a particular secular trap frequency involves locating the motional carrier and the first blue sideband resonances. For our experimental configuration, the two transverse blue sideband resonances corresponding to the trap axes, x and y, are within 20 kHz of each other. In this case the Raman laser power is chosen to be low enough to allow the sideband transitions to be resolved. The appropriate pulse time for the Ramsey pulses is chosen from a time scan of the Rabi oscillations on resonance (see Fig. 5.4(a)). In order to optimize the Ramsey fringe contrast, the time for each Ramsey pulse is chosen to be half the time to reach the peak of the first oscillation in Fig. 5.4(a).

The contrast of the Ramsey fringes and the spectroscopic resolution possible depend on the free-evolution time, which needs to be chosen appropriately. Figure 5.5 shows how the contrast of the Ramsey oscillations for the transverse blue sideband depends on the free-evolution time. As discussed above, the initial contrast is primarily limited by the initial $\bar{n}$ value and detection efficiencies (similar to the first peak shown in Fig. 5.4(a)). At longer times ($5 - 10$ ms), the contrast in the Ramsey oscillations is still substantial, but point-to-point jitter in the accumulated Ramsey phase leads to a loss of a clean oscillation. Some contrast loss can be attributed to motional heating as noted above (with typical estimated decoherence time of ~ 20 ms), but the jitter seen here is due to other effects, likely interferometric noise between the Raman beams, or possibly fluctuations in the resonance itself. For more experimental averaging per point as used in most of our data $-$ 100 repetitions per point compared to 50 per point shown here in Fig. 5.5 $-$ these fluctuations will convert to a contrast reduction, but the signal-to-noise ratio is still sufficient for a useful measurement certainly out to 10 ms. The choice of free-evolution time in practice is determined mostly by how quickly the resonance drifts, which requires updating the scan range. Typically in our experiment we use free-evolution times of $1-4$ ms with an averaging

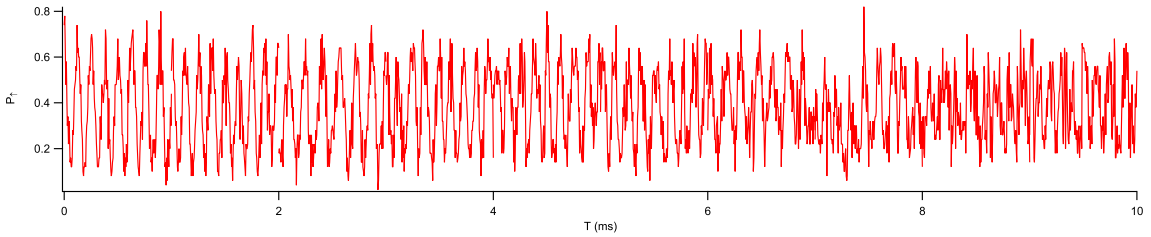

Figure 5.5: This shows the contrast of our Ramsey experiment as the free-evolution time is varied for the transverse blue sideband resonance. The detection efficiencies were $\zeta_\downarrow = 0.08$ and $\zeta_\uparrow = 0.95$, a 5 μs step size, and 50 experiments-per-point averaging.

of 100 experiments per data point. Occasionally, 10 ms is used to push the measurement resolution of the resonance down to a few Hertz.

In order to set up to monitor fluctuations of the secular trap frequencies in time, there are several steps. For the transverse direction, the axis with high secular frequency (x-axis) is chosen for monitoring the first blue sideband for technical reasons: the location of the free-evolution resonance is such that it minimizes cross-talk in the Ramsey fringes from the other (y-axis) blue sideband transition. After the Ramsey pulse times are set as discussed above, the next step is to locate the first blue-sideband transition's (free-evolution) resonance, which is shifted from the single-pulse Rabi resonance by the ac Stark shift (~ 10 kHz typically, determined as shown in Fig. 5.4(b)). The resonance location is confirmed by a Ramsey time-scan, which should reveal zero, or at least slow, oscillations. At this point, the experiment is ready to collect data, and a Ramsey frequency-scan can be collected and fit to extract the resonance location. The data collection of each scan takes ~ 3 minutes, which is mostly determined by the laser cooling time in the experimental sequence. The acquisition time is not an issue since we are focused in this preliminary set of measurements on slow fluctuations, corresponding to drifts over several minutes to hours. In the future, we also plan to measure a minimal number of Ramsey fringe points to increase the repetition rate of the experiment to consider faster fluctuations, as done by Johnson et al [33].

Once a monitoring experiment begins, the frequency is scanned repeatedly while the scan range is changed manually between scans to keep the scan range centered on the resonance. The span of a frequency scan is chosen such that two Ramsey fringes will be visible in the scan for sufficient range for subsequent curve fitting. Figure 5.6 shows an example of a frequency scan for the axial blue sideband as a function of the frequency, ν, of the synthesizer driving the double-pass Raman South AOM. From Fig. 5.3(d) and 5.6, one can see that the Ramsey fringe pattern is approximately a sinusoidal wave over a limited region where the contrast is fairly constant. Therefore, the fitting function used is an empirical formula as follows:

$$P_\uparrow(\nu) = (\zeta_\uparrow - \zeta_\downarrow)\left[A\sin^2(4\pi(\nu-\nu_o)T) + P_o\right] + \zeta_\downarrow. \tag{5.7}$$

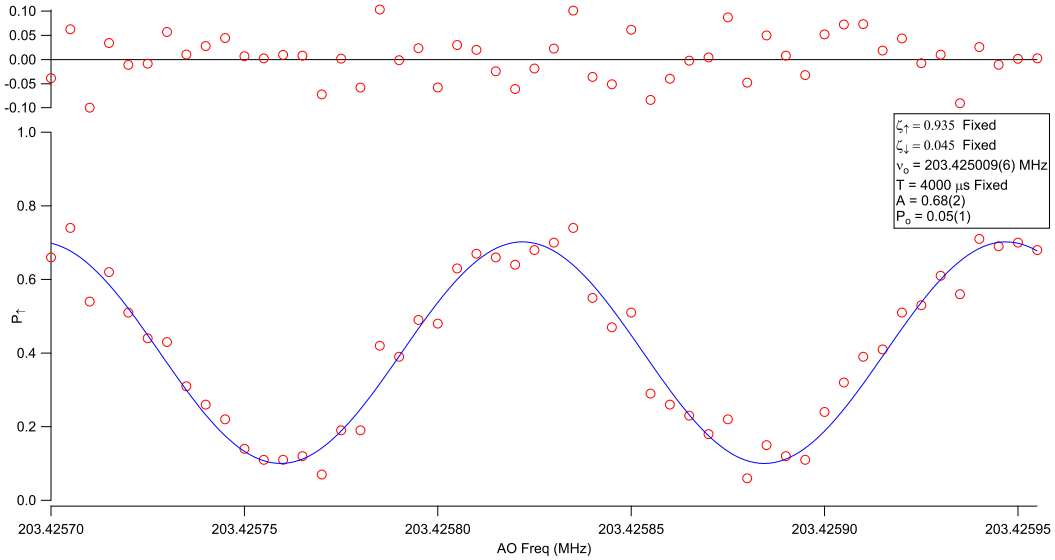

Figure 5.6: This figure shows an example of a Ramsey fringe data and fit used to monitor drifts in the resonance. The transition being scanned here is the axial first blue sideband. The red markers are the probability of measuring the $|\uparrow\rangle$ state versus the frequency of the scanning AOM, and the blue line is the empirical function, Eq. 5.7, fitted to the data. The top graph shows the residuals from the fit. The scanning AOM is in a double-pass configuration, therefore the fringe width seen here is half of the actual width. Experimental parameters include a free-evolution time of $T = 4$ ms, a pulse time of $\tau_{\pi/2} = 40$ μs, 100 experiments per point, and a step size of 5 Hz.

The fitting function assumes a $\sin^2$ form, which crudely accounts for the shift of the Ramsey fringes near resonance due to the ac Stark shift (see Fig. 5.3(d)). The main fit parameter extracted is the frequency, ν_o, of the minimum nearest to resonance. The fitting function has several other parameters that can be varied or held constant. The parameters $\zeta_\uparrow$ and $\zeta_\downarrow$, which account for the detection efficiencies, are assessed not to change over the duration of a data collection period and so are held constant in the fit. The free-evolution time T is held constant since the value is fixed for the data collection. The amplitude A and offset P_o, which together account for contrast loss and optical pumping effects, are taken as free fit parameters. From the fit value of frequency ν_o, which is given in AOM frequency, the secular trap frequency is calculated by

$$\nu_i = -2\left(\nu_{o,BSB} - \nu_{o,carrier}\right). \tag{5.8}$$

The factor of -2 in Eqn. 5.8 is due to the double pass configuration of the Raman tuning AOM and other Raman setup details (see Chp. 3 and [22]). The carrier resonance is in practice not measured each time to track changes in the secular frequency since the carrier resonance is more stable compared to the first blue sideband (as will be discussed later).

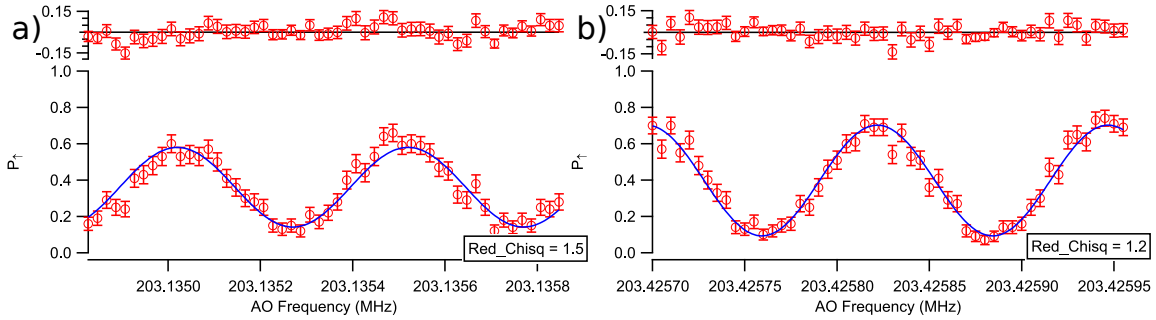

Figure 5.7: Figure (a) shows a frequency scan of the transverse blue sideband (with $T = 1$ ms), and Figure (b) shows a similar frequency scan for the axial blue sideband (with $T = 4$ ms). Figure (a) and (b) are fitted with the empirical fit function, Eqn. 5.7, and the error bars are statistical errors. The reduced χ^2 values for each plot are shown.

Just the variations in the blue sideband are monitored to infer variations in the secular frequency.

Fitting Function Performance

We now comment briefly on how well the empirical fitting function performs. Figure 5.7 shows fits for two typical Ramsey fringe scans for the blue sideband in the transverse and axial directions. For the purpose here the fits are weighted according to the estimated uncertainties due to the detection statistics, and the typical reduced χ^2 values obtained are 1.3 axially and 1.7 transversely. Two features omitted in the empirical fit function compared to Eqn. 5.5 are a gradient in the contrast, which becomes a more pronounced effect at shorter T (e.g. compare Fig. 5.7(a) and (b)), and a correction to the periodicity from the simple assumption of $1/T$. Other than these effects, it is also possible to acquire distortions in the measured scan if the resonance frequency drifts during the three-minute acquisition time of the scan. Overall the fits work reasonably well.

5.3 Carrier Stability

In order to place a limit on how well the blue sideband resonance at $\omega_{HF} + \omega_{trap}$ can act as a diagnostic of the secular trap frequency, ω_{trap}, we first investigate the stability of the carrier transition between $|\downarrow\rangle$ and $|\uparrow\rangle$ at ω_{HF}. This is done in two ways: using Raman laser beams to probe the motion-sensitive carrier along the direction of interest, and using microwaves. The latter allows the separation of optical Raman effects like ac Stark shifts from other measurement noise such as the stability of the reference oscillator for the synthesizers used to drive the transitions. For a single ion, measurements of the carrier using microwave Ramsey spectroscopy and axial Raman Ramsey spectroscopy were alternated every few minutes for two hours. Figure 5.8(a) shows the frequency variation of

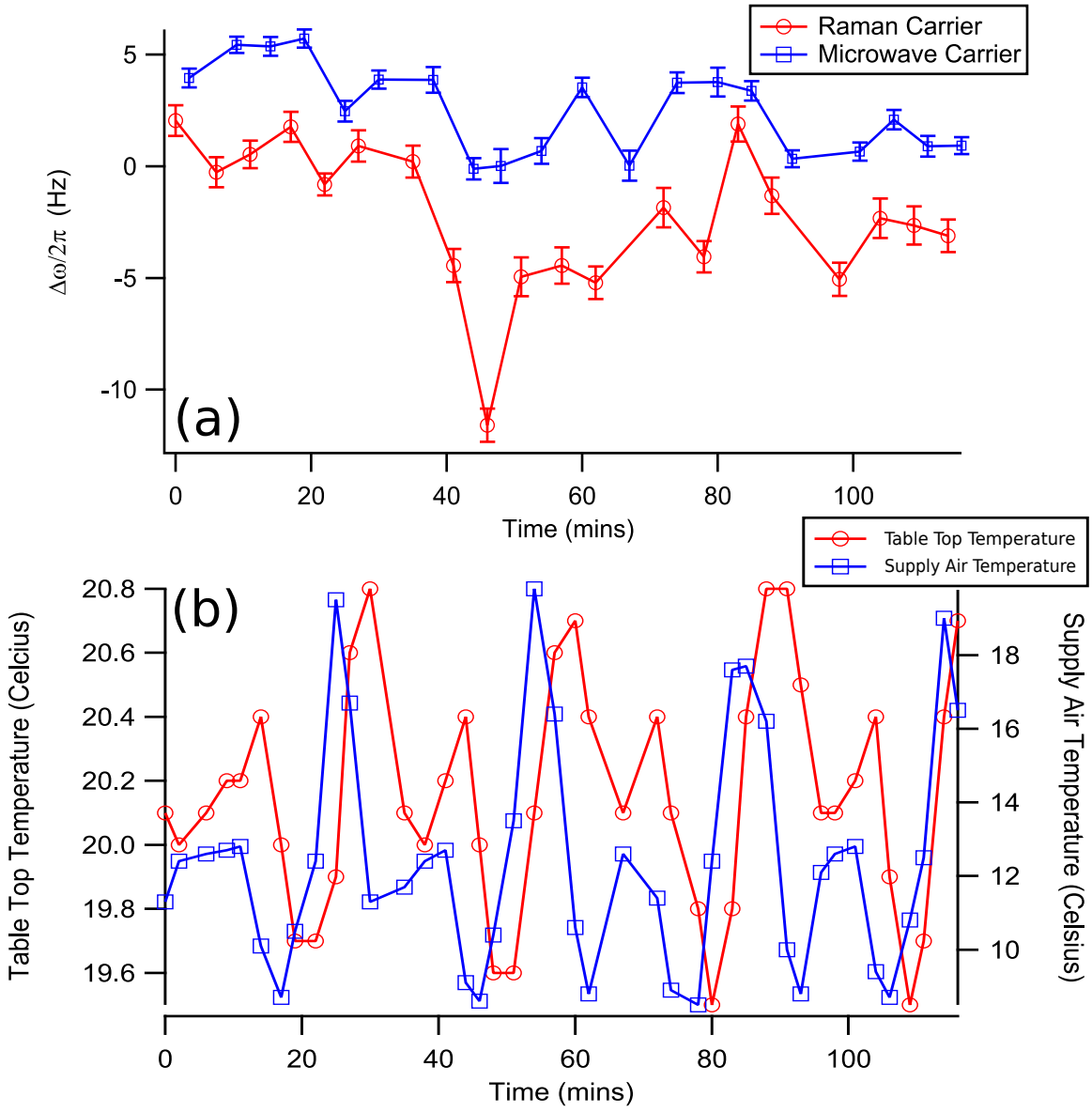

Figure 5.8: (a) Stability of the 12.6-GHz microwave and motion-sensitive carrier transitions for a single trapped $^{171}Yb^{+}$ ion. (b) Table-top temperature and supply-air temperature during the experiment. For the microwave carrier the experimental parameters are a pulse time of $\tau_{\pi/2} = 35$ μs, a free-evolution time of $T = 10$ ms, and 100 experiments-per-point averaging. For the Raman carrier the experimental parameters are a pulse time of $\tau_{\pi/2} = 45$ μs, a free-evolution time of $T = 4$ ms, and 100 experiments-per-point averaging.

the measured resonance versus time for both transitions. In Fig. 5.8(b), the temperature of the ambient air above the optical table ("table-top temperature") and the temperature of the air being supplied to the laboratory from the A/C unit ("supply-air temperature") are also shown over the same time frame. Both the microwave and the Raman carrier transition showed $\sim$ 6 Hz of variation over the two hours (if the one point with large excursion in the latter data set is neglected). The variations consist of fluctuations over several minutes, which may be due to the ambient temperature variations, and a slow drift over hours, which occurs for both measurements. One possible source of the measured frequency variations are variations in the magnetic bias coil's field of 5.9 G, at which the carrier transition's sensitivity is 3.6 Hz/mG. The stability of the Raman carrier resonance places a lower limit on the secular trap frequency instabilities that can be detected with the blue sideband measurements.

5.4 Axial Secular Trap Frequency Stability

On the same day as the carrier assessments of Fig. 5.8 were performed, the axial blue sideband resonance was monitored using the Ramsey technique over an hour with a typical secular trap frequency of $\omega_z/2\pi \approx 0.325$ MHz. Since these measurements, shown in Fig. 5.9, were performed prior to the improvements made to the voltage system noted in Chp. 3, they represent a benchmark to evaluate the effectiveness of the improvements, to be discussed in subsequent sections. In Fig. 5.9(a), the axial sideband resonance shows fluctuations on a time scale of several minutes, but more importantly, it also displays a linear drift of $\sim$ 22 Hz/hr over the one hour collection time. This frequency drift is much larger than those seen for the carrier in Fig. 5.8(a) and thus can be ascribed to secular frequency changes. Figure 5.9(b) shows the variations in the table-top and supply-air temperatures during the measurements. From Fig. 5.9(a) and (b), there is no obvious correlation between temperature and frequency variations.

The 22-Hz change over one hour shown in Fig. 5.9(a) corresponds to 70 ppm in the axial secular trap frequency. This is much more than our target of 10 ppm over that time frame and led us to assess various sources of instability. We now outline some of these in the following discussion, which is not an exhaustive list.

The trap size, R, can be expected to vary with temperature and leads to variations in the ion-trap potential. This is not easy to estimate given the uncertainties in temperature variations of the trap, the range of temperature coefficients for different materials ($4.5 \times 10^{-6} K^{-1}$ for tungsten and $23.1 \times 10^{-6} K^{-1}$ for aluminum [30]), and the exact model of deformation. Nevertheless, changes in the trap size leading to secular trap frequency fluctuations on the order of 10 ppm or larger would not be surprising. The variations would not necessarily have an obvious temperature correlation to the ambient air temperature since the trap is attached to the thermal masses of the vacuum chamber and feedthroughs.

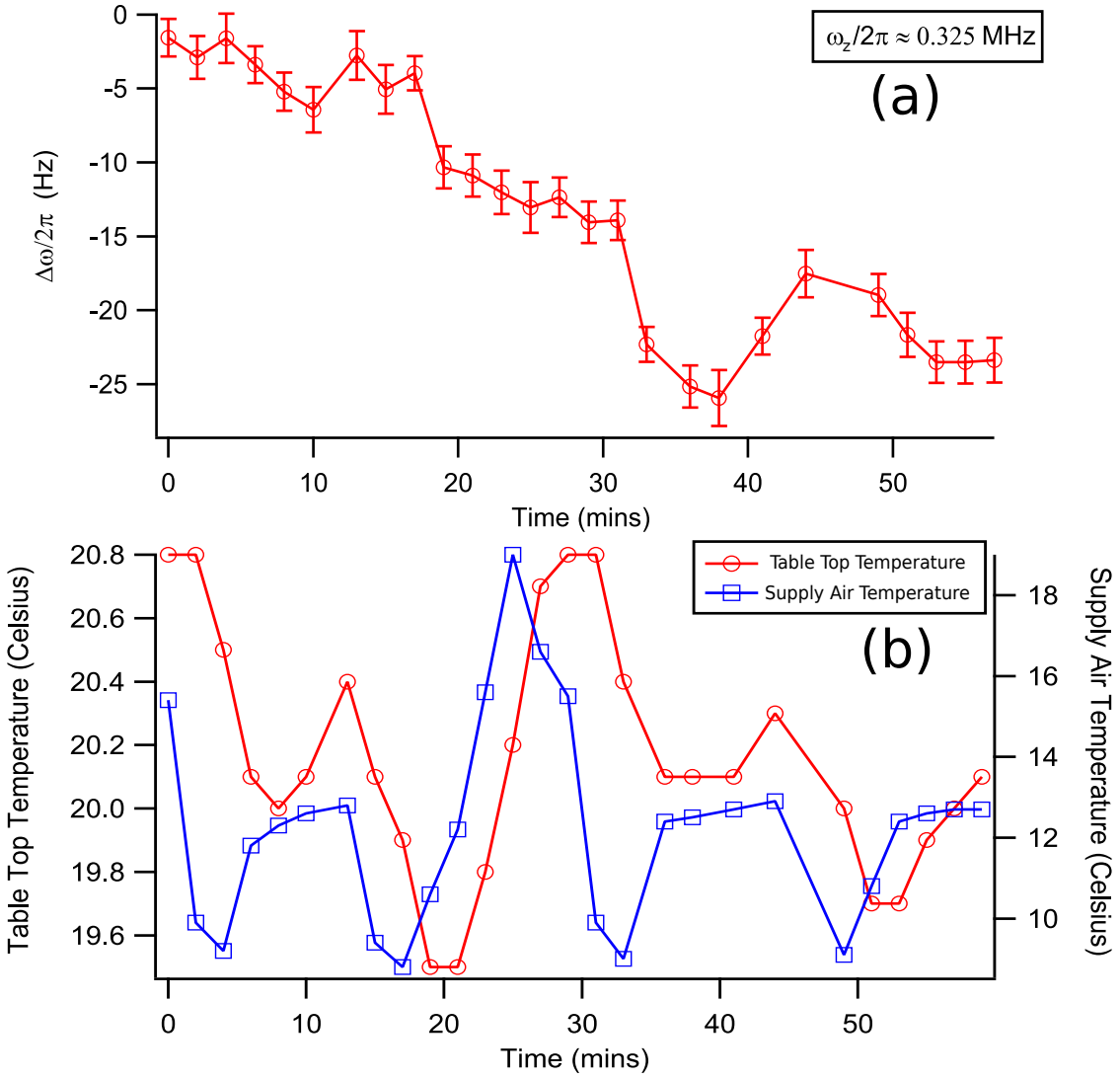

Figure 5.9: (a) Variation in the axial secular trap frequency, $\omega_z/2\pi \approx 0.325$ MHz, before improvements were made. Each data point is inferred from a measurement of the first axial blue sideband resonance. (b) Temperature variations over the same time as data set in (a). Experimental parameters include a Ramsey pulse time of $\tau_{\pi/2} = 20$ μs, a free-evolution time of $T = 4$ ms, and 100 experiments-per-point averaging.

In the end, we rule out thermal-mechanical instability in the initial consideration since, as will be seen, the secular frequencies in the transverse direction can show much better stability performance than that seen in Fig. 5.9.

Another obvious suspect is the DC power supply that supplies the voltage to the end caps. A frequency drift of 70 ppm corresponds to 140 ppm in the end-cap voltage of 78 V, or 11 mV. The Agilent E3612A DC power supply used has a specified temperature coefficient of $< (0.0002 \cdot V_{out} + 1 \text{ mV})/^\circ\text{C}$ [67]. For an output voltage of 78 V in our experiment, this corresponds to a maximum temperature coefficient of 17 mV/°C, which appears significant

even though an obvious temperature correlation was not seen in Fig. 5.9. An initial rough measurement of the stability of the output voltage also revealed that the DC power supply could be the cause of the axial secular trap frequency instabilities, and this motivated our stabilization of the end-cap voltage, as discussed further below. However, we note here in advance that with the later acquisition of a 6.5-digit multimeter, we revisited this measurement and found somewhat less sensitivity of the DC power supply to the ambient air temperature, on average ~ 2 mV/°C.

To a first order approximation, the four DC voltages applied to the rods average to act as the ground to the endcaps; therefore, the DC rod voltages are also important to consider as a source of the instability in the axial trap potential. The specified temperature coefficient of the PCI card (National Instruments PCI-6733) used as the source for the rod voltages is quite good at 6.5 ppm/°C [9]. The voltage outputs of the PCI card are passed through an amplifier to the trap rods (see Chp. 3). In an offline test, the DC voltages supplied to the rods (< 1 V) were monitored with a 6.5-digit multimeter (Keysight 34465a), and found to have variations of 100 μV over thirteen hours. This is too small to explain the changes seen in Fig. 5.9.

A few other sources of voltage instability might also be considered. The role of stray electric fields from the vacuum ion pump and gauge could be a possibility, but our micromotion compensation is relatively stable in time. Some other effects that we have considered are worth noting but more so in the context of the performance of the end-cap servo, since these effects are more relevant to obtaining a faithful sense voltage at the 1-V level. Issues that can cause instabilities in the sense voltage include, for example, temperature gradients in conductors (i.e. BNC cables) causing a potential gradient to form, temperature gradients between dissimilar conductors causing a potential difference (Seebeck Effect), and ground loops. The first two mentioned are on the order of a few microvolts per degree Celsius [34] and should be considered for the 1-V sensor signal used for servo-ing the end-cap voltage to 10 ppm. We also found several ground loops in the experiment setup, which were leading to offsets on the order of several millivolts. Functionally, one would see a transient of a DC level shift whenever a device is connected or disconnected (turned on and off). In this way, ground loops might be expected to cause sudden jumps or spikes in the axial secular trap frequency, as well as providing voltage offsets that can drift as well. As part of the servo setup, we acted to reduce voltage offsets in the ground return lines by eliminating ground loops where possible and by using instrumentation amplifiers for the lock sensor (see Chp. 3).

5.4.1 Axial Secular Trap Frequency Stability Following Upgrades to the End-cap Voltage System

Following the improvements described above, in particular the addition of an end-cap voltage servo, the axial secular trap frequency was monitored with sideband spectroscopy over

several hours on two successive days. The end-cap voltage remained locked with the servo continuously over the two days. The method of measuring the axial blue sideband resonance was similar to the previous measurements shown in Fig. 5.9. A single trapped ion was used that was Sisyphus cooled, and the Ramsey spectroscopy made use of a free-evolution time of $T = 10$ ms. In addition to recording the table-top temperature during the experiment, the setup included a 6.5-digit multimeter (Keysight 34465a) to log the sensor voltage, V_{sense}, that is derived from the end-cap voltage with a 100:1 divider and is used by the end-cap servo (see Chp. 3).

The results of the experiment are summarized in Fig. 5.10. Due to technical issues, the V_{sense} record is only available for the second day's run. There are occasional jumps in the axial blue sideband frequency that were observed; the cause of these jumps is unknown. The main feature observed are drifts that remain linear over time scales up to hours. On the first day, the frequency drifted by 23 Hz/hr (or 70 ppm/hr). On the second day, the first 120 minutes showed a frequency drift of 6 Hz/hr (or 19 ppm/hr), while the rest of the measurement saw a drift similar to the previous day of 23 Hz/hr (or 70 ppm/hr). Given the record of the table-top temperature over the two days shown in Fig. 5.10(b), there is clearly no correlation in behaviour. From Fig. 5.10(c), V_{sense} during the second day varied by ~ 25 μV, which can account for only 16 ppm of drift in the axial secular trap frequency, while over the same time the measured frequency drifted by more than 300 ppm. This suggests that the end-cap voltage is not the cause of the observed drifts. The frequency drift values shown in Fig. 5.10 are in fact comparable to the values obtained before the system improvements were installed, as seen in Fig. 5.9. This suggests that the addition of an end-cap voltage servo is not a sufficient solution to remove the drifts in the axial secular frequency.

One common feature of the drifts seen in Figs. 5.9 and 5.10 is that they all have a negative slope. To assess for diurnal effects, we show all data runs performed over several weeks, plotted according to the time of day in Fig. 5.11. The jumps seen between days are caused by slight differences in the end-cap voltage that was used for each of the days, and therefore they are of no consequence. There is no obvious correlation between the frequency drifts with the time of day (e.g. as a result of the building's A/C varying). In fact, notwithstanding the differences in the servo setups used for the data sets, Fig. 5.11 reveals the same common decreasing trend in the axial secular trap frequency. This is a trend that is seen in every single other measurement that has neen made in the pursuit of stabilizing the axial secular trap frequency. The drift on the days shown range between $\sim 15 - 32$ Hz/hr ($\sim 45 - 100$ ppm/hr), in other words $5 - 10$ times the goal we were seeking to achieve.

In conclusion, locking the end-cap voltages does not eliminate the secular trap frequency drifts in the axial direction as originally hoped. The drifts in the axial secular trap frequency do not seem to be correlated with the lab temperature variations. The cause of these drifts

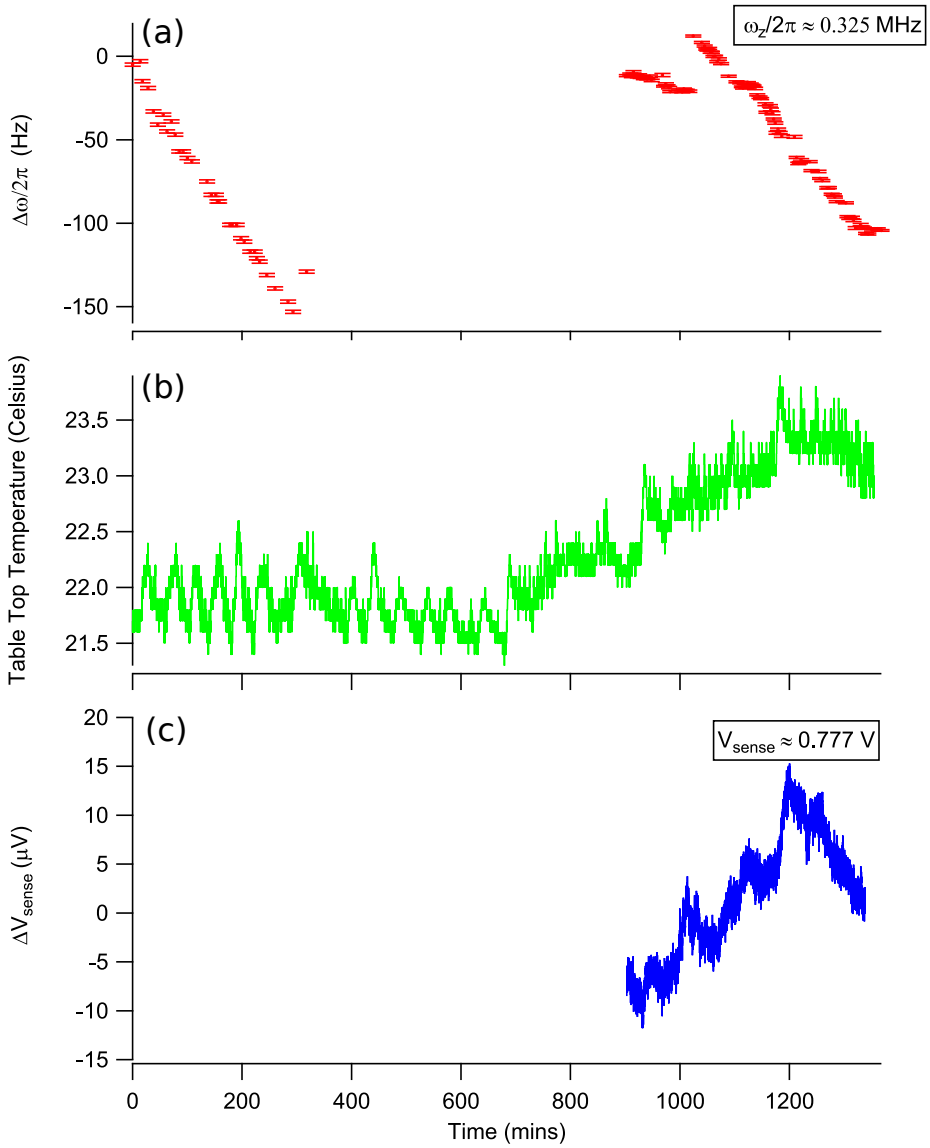

Figure 5.10: Monitor of the axial secular trap frequency over several hours on two successive days. (a) Measured variations in the axial secular trap frequency ($\omega_z/2\pi \approx 0.325$ MHz) inferred from the first axial blue sideband resonance. The error bars are statistical errors obtained from fitting. (b) Table-top temperature measurement. (c) V_{sense} measurement on the second day. Experimental parameters include a Ramsey pulse time of $\tau_{\pi/2} = 25$ μs, a free-evolution time of $T = 10$ ms and 100 experiments-per-point averaging.

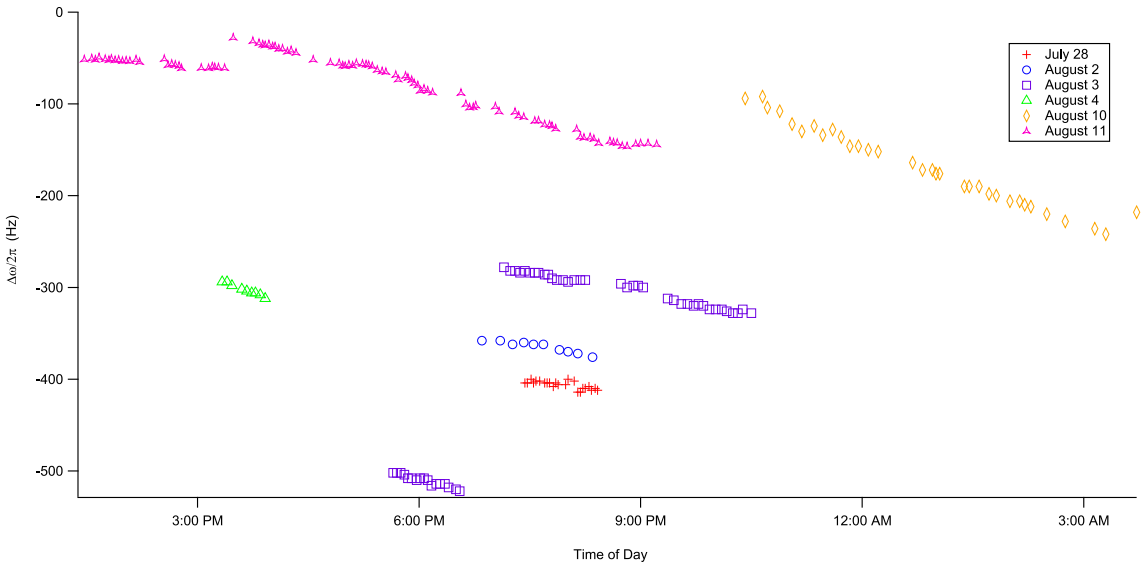

Figure 5.11: Drifts in the axial secular trap frequency ($\omega_z/2\pi = 0.325$ MHz) for several different days graphed against time of day. Frequency variations are inferred from the Ramsey spectroscopy of the axial first blue sideband. All data was taken with a free-evolution time of $T = 4$ ms or $T = 10$ ms and 100 experiments-per-point averaging.

seems to be downstream of the locking setup for the end-cap voltage, but the exact cause is still to be investigated.

5.5 Transverse Secular Trap Frequency Stability

In the last set of experiments we test the stability of the ion trap in the transverse direction. As discussed in Chp. 2, the transverse trapping potential has two principal axes, denoted x and y, with secular trap frequencies of about 0.90 MHz. For the tests, we operate near zero DC bias on the rods, for which the x and y secular trap frequencies differ by 20 kHz. Since most of the dependencies are common, in particular the dependence on the RF voltage V_o, we have focused on just the x-axis for the transverse stability assessments (and choose the x-axis in particular to minimize cross-talk between the x- and the y-axis sideband resonances). In the same way as for the axial trap direction, we first present the passive stability of the transverse secular frequency as a benchmark prior to the RF voltage servo improvements detailed in Chp. 3. The experimental procedure and sequence for monitoring the transverse secular trap frequency, inferred from the first blue Raman sideband, is the same as described in Sec. 5.2.3. The measured frequency variations are shown in Fig. 5.12 along with a record of the table-top temperature during the acquisition. Over a one-hour period the transverse secular trap frequency (~ 0.90 MHz) varied by ~ 1100 Hz (1200 ppm), which is a factor of nearly 120 higher fluctuation than our goal of 10 ppm. The sensitivity of the transverse

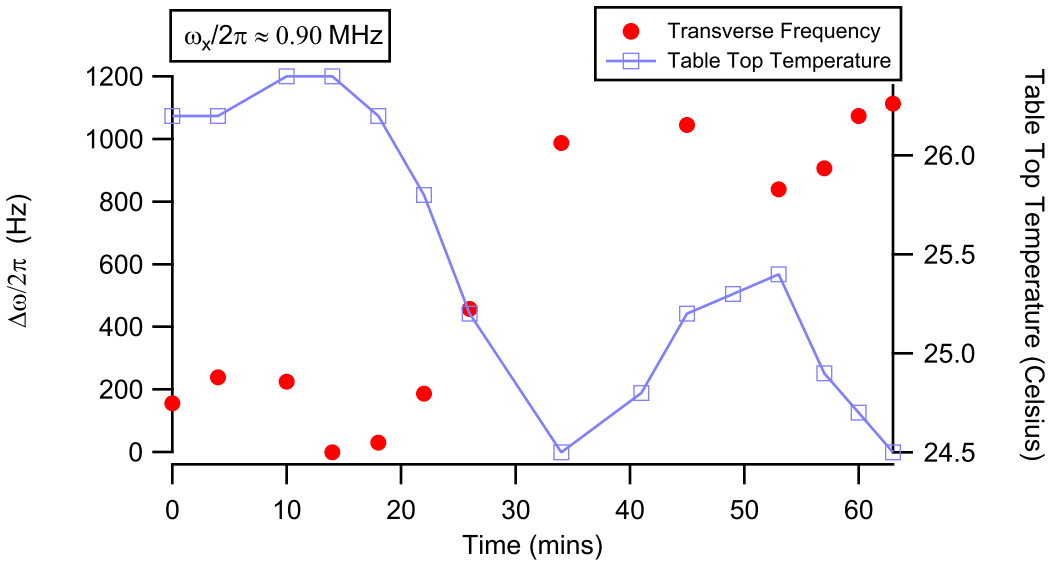

Figure 5.12: Passive stability of the transverse secular trap frequency ($\omega_x/2\pi = 0.90$ MHz) prior to upgrades in the trap RF setup. Frequency variations are inferred from the Ramsey spectroscopy of the transverse first blue sideband. Note that the error bars ($\sim \pm 10$ Hz) are smaller than the markers. Experimental parameters include a Ramsey pulse time of $\tau_{\pi/2} = 55$ μs, a free-evolution time of $T = 1$ ms, and an averaging of 100 experiments per point.

secular frequency to the ambient laboratory temperature, as previously described in [22], is evident in Fig. 5.12.

Following the discussion of Chp. 2, frequency variations in the transverse secular frequency can be due to instabilities in the RF voltage, the most likely cause of the variations seen in Fig. 5.12, but also instabilities in the RF frequency, DC voltage and trap electrode spacing. The frequency stability of the RF generator (HP 8640B) was measured to be ~ 200 Hz (or ~ 12 ppm) peak-to-peak over an hour, which is much too small to be the cause of the variations measured in Fig. 5.12. The DC rod voltages have a variation of ~ 100 μV (33 ppm) over a 13 hour period, as previously discussed, which corresponds to a variation of ~ 4 ppm in the transverse secular trap frequency. This is also much too stable for the fluctuations seen. Similar to the axial direction, the transverse trap potential can also vary if the trap size (R) varies with temperature, but the size of the observed variations makes this somewhat unlikely as the primary cause.

Previously, variations of the RF input power to the helical resonator were observed to be correlated with the laboratory temperature [22], but a servo of the input power was determined to be insufficient to stabilize the transverse secular frequency. This is likely due to additional instabilities in the resonator-trap system itself, and motivated the improvements to the RF servo outlined in Chp. 3. As discussed there, a new helical resonator was built to allow the RF voltages to be sampled and servo'ed at the output of the resonator,

in other words closer to the trap. The full details of this new resonator's construction are beyond the scope of this thesis and will be presented elsewhere [77]. The discussion in the following section is limited to preliminary results of the trap stability with the new setup.

5.5.1 Transverse Secular Trap Frequency Stability After System Improvements

Following the improvements to the RF servo setup, a set of tests were undertaken to assess the ion-trap stability in the transverse direction. The experimental procedure and sequence were performed as described in Sec. 5.2.3. Many parameters were monitored for these experiments including the resonator temperature, the resonator frequency, and the RF sampling voltages, V_{RF1} and V_{RF2}, corresponding to each of the bifilar helical resonator coils (see Chp. 3). The servo was locked to V_{RF2} while V_{RF1} was used as an independent monitor. Both voltages were logged together using a 6.5-digit multimeter. Figure 5.13(a) shows the transverse secular trap frequency variations with the servo locked and unlocked, as well as the corresponding temperatures and sensor voltages in each situation. Compared to the prior benchmark test, the servo improved the transverse secular trap frequency stability to ~ 300 Hz (~ 325 ppm) over a 90 minute period. This is nearly a factor of four improvement; however, the servo does not achieve 10 ppm stabilization of the transverse secular trap frequency over a long time. Furthermore, comparing these results to previous measurements with only the input power to the resonator servo'ed [22], we find (surprisingly) that there is only a fractional improvement (or perhaps a factor of two improvement when one considers timescales) in stability. From Fig. 5.13(c), the fluctuations of V_{RF2} are strongly reduced (since the servo is locked to it), but V_{RF1} still exhibits significant fractional variation that *exceeds* that of the transverse secular frequency. The source of the fluctuations on V_{RF1}, and why its mean value differs by a factor of two from V_{RF2}, is not clear and will be explored elsewhere.

The unlocked case shown in Fig. 5.13 shows the same negative correlation between the table-top temperature and the transverse secular frequency as seen with the benchmark tests performed with the old RF resonator (Fig. 5.12). In both cases, a $\sim$ 1100-Hz frequency variation is observed for a ~ 2°C variation of the table-top temperature. For the locked case in Fig. 5.13, there still appears to be a temperature correlation but now it is positive. This suggests that the RF sampling setup has a temperature sensitivity, or there is some other effect downstream from the monitoring location in the resonator. The former would be surprising (and somewhat disappointing) given that temperature-insensitive components were used for the capacitive RF sampling divider and a temperature-insensitive design was used for the RF power detector, per the setup detailed in [33]. Figure 5.14 shows the strong temperature correlation with a value of 167(9) Hz/°C. This suggests that without changing the experimental setup, a temperature stability of ~ 0.05 °C is needed in the lab to have a transverse secular frequency stability of 10 ppm.

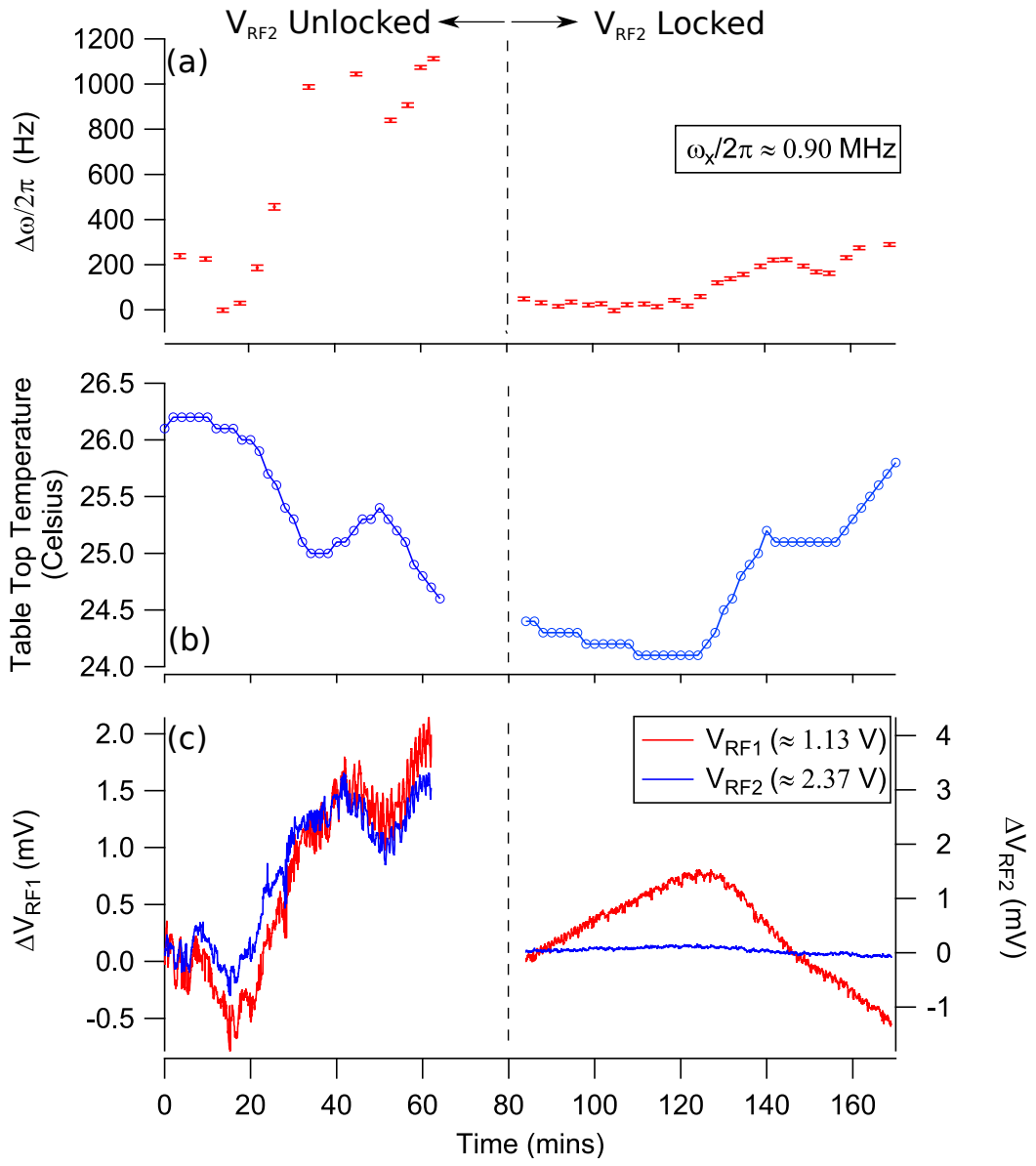

Figure 5.13: (a) Variations in the transverse secular trap frequency ($\omega_z/2\pi \approx 0.90$ MHz), inferred from measurements every ~ 3 minutes of the first transverse blue sideband resonance. Measurements with the trap RF voltage locked using the sense voltage V_{RF2}, and with the RF voltage unlocked, are shown. (b) Table-top temperature variations (measured at the same rate as the secular frequency). (c) V_{RF1} and V_{RF2} variations (measured once every two seconds). Vertical plot ranges for V_{RF1} (left axis) and V_{RF2} (right axis) are scaled approximately by the ratio of their mean values to show consistent fractional variation. Experimental parameters include a Ramsey pulse time of $\tau_{\pi/2} = 55$ μs, a free-evolution time of $T = 1$ ms, and an averaging of 100 experiments-per-point.

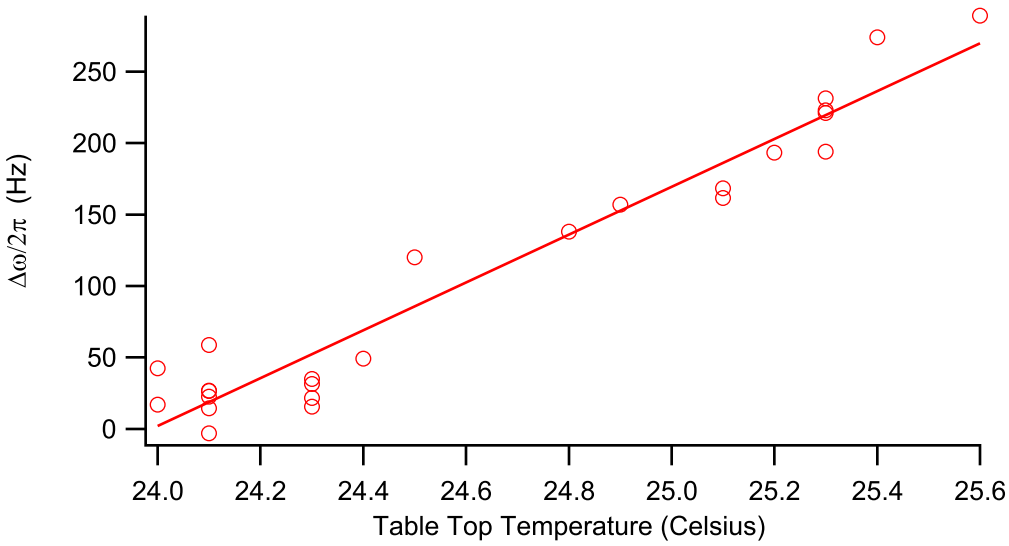

Figure 5.14: Correlation between the fluctuations in the transverse secular trap frequency ($\omega_x/2\pi = 0.90$ MHz) and the table-top temperature for the data in Fig. 5.13. Also shown is a linear fit with a slope of 167(9) Hz/°C.

The climate control of our lab cycles the supply air such that cold drafts are blown on to the optical table. To mitigate this, the RF resonator was insulated with foam. It should be noted that the insulation will not help with slow ambient lab temperature variations. Another set of measurements were taken, shown in Fig. 5.15, using the same experimental procedure as used for Fig. 5.13. For the new set of measurements, the resonator temperature was also monitored using a National Instruments thermocouple (NI USB-TC01). Furthermore, the time of day for the experiment was chosen to take advantage of very stable lab temperatures due to no A/C compressor cycling. From Fig. 5.15(a) for the unlocked measurement, the transverse secular trap frequency varied by ~ 350 Hz (380 ppm) peak-to-peak over two hours. Given that the variations do not have a significant linear trend, we also quote a standard deviation of 98 Hz for the variations.[2] The locked transverse secular trap frequency varied by $\sim$ 60 Hz (65 ppm) over 80 minutes with a standard deviation of 14 Hz (15 ppm). The locked stability represents an improvement by nearly a factor of five over the previous uninsulated, locked measurement (Fig. 5.13(a)), and an improvement by nearly a factor of twenty overall from the initial measurement before the setup improvements (Fig. 5.12). The improvement in secular frequency stability is aided just by having more stable laboratory temperatures (a factor of three or more stable), as can be seen by comparing the *unlocked* behavior in Fig. 5.13(a) and 5.15(a). In Fig. 5.15(a), the passive stability of the unlocked secular frequency is already better than that shown in Fig. 5.13(a) by a factor of about three, or by a factor of six if the outliers corresponding to rapid changes are omitted.

[2]If the outliers are omitted, the standard deviation is 54 Hz ($\sim$ 60 ppm).

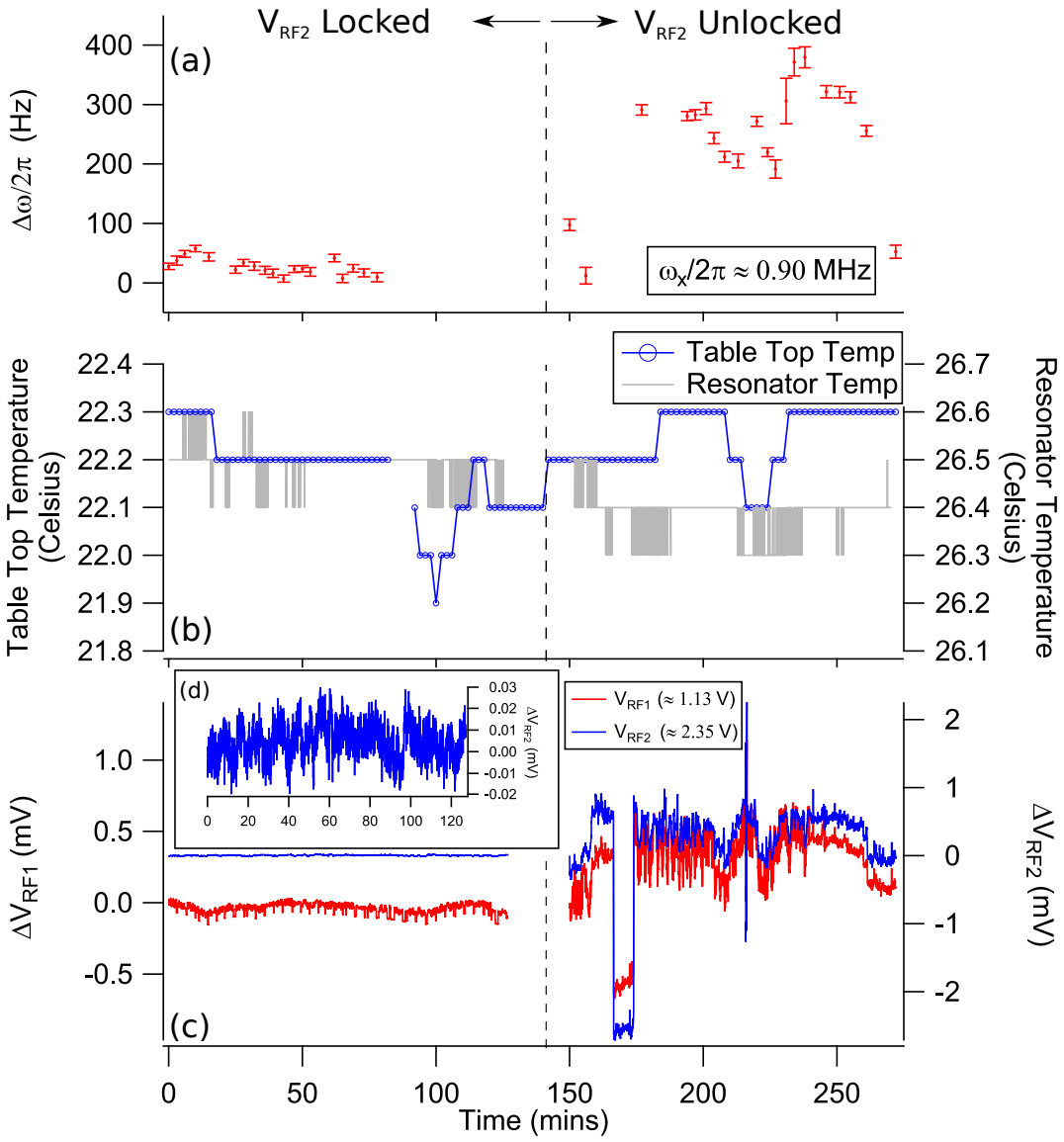

Figure 5.15: (a) Variations in the transverse secular trap frequency ($\omega_x/2\pi \approx 0.90$ MHz) with the helical resonator insulated against air currents. Variations are inferred from the first transverse blue sideband resonance, measured every ~ 3 minutes. (b) Table-top temperature variations (measured every two minutes) and the resonator temperature variations (measured every second). (c) V_{RF1} and V_{RF2} (measured every two seconds) for the locked and unlocked measurements. Vertical plot ranges for V_{RF1} (left axis) and V_{RF2} (right axis) are scaled approximately by the ratio of their mean values to show consistent fractional variation. (d) For the locked measurement, the inset graph shows a zoom-in of the V_{RF2}. Experimental parameters include a Ramsey pulse time of $\tau_{\pi/2} = 55$ μs, a free-evolution time of $T = 1$ ms, and an averaging of 100 experiments per point.

A natural question is what limits the observed stability of the locked case seen in Fig. 5.15. The frequency variations are still larger than those for the carrier transition in Fig. 5.8 so they can still be ascribed primarily to variations in the transverse trapping potential. As part of the measurements, the RF frequency was recorded, but the contribution of a few Hertz change to the transverse secular frequency fluctuations does not entirely explain these fluctuations. Another possibility could be residual temperature variations of the RF resonator. Comparing the table-top and resonator temperatures shown in Fig. 5.15(b), the insulation does help to smooth out the fast lab temperature fluctuations by perhaps a factor of two. The resonator temperature measurements are limited by the thermocouple's resolution of 0.1 °C; however, during the 80 minute period, we can say that the temperature during the locked measurement, as shown in Fig. 5.15(b), varied by less than 0.2 °C. According to the linear correlation obtained from Fig. 5.14, this temperature fluctuation should give a transverse secular trap frequency stability of < 34 ppm. The measured peak-to-peak instability is as much as a factor of two larger, which might indicate that there is another source of fluctuations. Figure 5.15(c) show the V_{RF1} and V_{RF2} variations for the locked and unlocked measurements. Both V_{RF1} and V_{RF2} appear more stable compared to the previous experiment shown in Fig. 5.13. Figure 5.15(d) shows a zoom-in of V_{RF2} while the servo is locked and gives some insight on how the servo is performing. The variations measured around the lock point are < 50 μV (< 22 ppm) peak-to-peak. This is not the primary contribution to the stability of the transverse secular frequency, but V_{RF2} variations and servo performance may need to be considered in the future. V_{RF1} is stable to ~ 0.1 mV (four times larger fractionally) when the servo is locked. Again, it is not clear why V_{RF1} is not as stable as V_{RF2}, but this will be explored in the future.

5.6 What is next?

Neither the axial nor the transverse secular trap frequencies have shown the desired stability level to make the planned experiments involving the linear-zigzag transition convenient. However, there have been significant improvements in the transverse secular trap frequency and the stability is approaching the original goal of 10 ppm over one hour.

For the transverse secular trap frequency, a stability level of ~ 60 Hz (~ 65 ppm) peak-to-peak was achieved over 80 minutes with a standard deviation of 14 Hz (15 ppm). The performance of a new servo system for the trap RF voltage was found to be limited by an unexpected residual temperature sensitivity in the lock setup. Without further improvements in the lock setup, measurements suggest that a stringent temperature stability of ~ 0.05 °C in the laboratory, or simply in the resonator-trap system, would be required to achieve 10 ppm stability in the transverse secular frequency. Other sources of instabilities may also exist at this level. Further investigations into the transverse secular trap frequency instabil-

ities will need to be conducted; however, the immediate experimental focus is on the drifts in the axial secular trap frequency, which are currently limiting our trap's performance.

For the axial trap direction, stabilization of the end-cap voltage was found to be insufficient to stabilize the secular frequency. The primary feature of the remaining frequency instability is a long-term drift that has no correlation with the ambient lab temperature. There must be some other cause of the drifts besides the DC voltage system; however, it is not apparent at the moment what the cause may be. A recent piece of evidence obtained by the group shows that a stability of < 20 ppm is achievable with tighter confinement in the axial direction. Tests are ongoing as of writing this thesis.

Chapter 6

Conclusion & Outlook

This thesis work has focused on two technological developments required for our ion-trap setup to explore the linear-zigzag transition in the quantum regime: enhanced RF synthesizer capabilities and improved stability in the ion-trap potential. To satisfy the need for a large number of stable RF sources to drive various optical Raman operations in an ion string, a solution was pursued based on readily available DDS development boards from Analog Devices along with an Arduino micro-controller as an interfacing device. The programming of the Arduino was done in the visual programming environment of LabView, which is also used in the main experimental control program for our group's ion trap system. Preliminary tests of the RF output of the AD9910 development board showed that it should have suitable performance for our needs in terms of user control, bandwidth, phase noise, spurious performance, and phase locking. The Arduino interface, however, was found to be not as simple and straightforward to implement as was first hoped. While LabView programming of the Arduino was hoped to make it simple to integrate into the existing experimental control program, the LabView interface to the Arduino was found to have insufficient reliability for our purposes. Moreover, phase synchronization of multiple development boards controlled by an Arduino interface was found to be inconveniently complicated.

It was originally assumed that it would be easier to develop an Arduino-based system than to build an existing open-source FPGA-based system detailed in [52]. The complications in practice with using the Arduino make it a less attractive solution in comparison. Future work for the digital synthesizer project will likely involve changing the interfacing scheme used to control the AD9910 development boards to one based on the FPGA design (or similar). The open-source nature of the FPGA design and the fact that similar setups are used by other ion-trap groups should hopefully speed the debugging.

The second portion of this thesis work consisted of preliminary results on stabilizing the secular trap frequencies in our group's linear RF Paul trap. Ramsey spectroscopy of the motional Raman sidebands was implemented to assess variations in the secular frequencies with time. In an attempt to improve the stability of the axial trap potential, various

improvements to the trap setup were made, in particular the implementation of a servo for the endcap voltages. However, there remains a persistent drift in the axial secular frequency of about 23 Hz/hr (70 ppm/hr) that is of unknown origin. More investigation is needed to determine what the source of the drift is as well as how to deal with it in future experiments. Recent experiments in our lab have already shown that a tighter trap confinement can increase the axial secular trap frequency stability to < 20 ppm over an hour, with further tests underway.

In the transverse axis of the ion trap, variations on a time scale of minutes in the secular trap frequency were reduced to a peak-to-peak range of roughly 60 Hz (65 ppm) over 80 minutes, and a standard deviation of 14 Hz (15 ppm), through a combination of passive and active stabilization. This represents a factor of roughly twenty improvement over the prior measured ambient stability, which was limited by a strong sensitivity of the trap RF voltage system to the laboratory temperature. The active stabilization was provided by a newly installed servo setup for the RF voltage, which is sampled at the output of the RF resonator. The locked setup was found to have a significant residual temperature sensitivity that remains to be resolved. In the interim, reaching the stated stability in the transverse secular frequency with the current setup requires a laboratory temperature control on the order of a tenth of a degree.

To achieve a set goal of 10 ppm stability in the secular frequencies, some further investigations are required to identify the remaining sources of instability. In the future, a faster readout of the secular trap frequencies will be implemented to investigate variations on a time scale on the order of seconds, similar what was done in [33]. Once sufficient stability in the ion-trap potential is achieved, our next experimental goal will be to investigate the behavior of ion strings close to the critical point of the linear-zigzag transition, including decoherence rates due to motional heating. The technologies being developed will also be of more general utility for future experiments including quantum information applications with strings of trapped ions.

Bibliography

[1] J. M. Amini, J. Britton, D. Leibfried, and D. J. Wineland. Microfabricated chip traps for ions. *arXiv preprint in arXiv:0812.3907v1*, Dec 2008. [Online]. Available from: https://arxiv.org/abs/0812.3907.

[2] J. D. Baltrusch, C. Cormick, G. De Chiara, T. Calarco, and G. Morigi. Quantum superpositions of crystalline structures. *Phys. Rev. A*, 84:063821, Dec 2011. [Online]. Available from: http://link.aps.org/doi/10.1103/PhysRevA.84.063821.

[3] J. D. Baltrusch, C. Cormick, and G. Morigi. Quantum quenches of ion coulomb crystals across structural instabilities. *Phys. Rev. A*, 86:032104, Sep 2012. [Online]. Available from: http://link.aps.org/doi/10.1103/PhysRevA.86.032104.

[4] A. Bauch, D. Schnier, and C. Tamm. Collisional population trapping and optical de-excitation of Ytterbium ions in a radiofrequency trap. *Journal of Modern Optics*, 39(2):389–401, Jul 1991. [Online]. Available from: http://dx.doi.org/10.1080/09500349214550381.

[5] D. J. Berkeland, J. D. Miller, J. C. Bergquist, W. M. Itano, and D. J. Wineland. Minimization of ion micromotion in a paul trap. *J. Appl. Phys. Journal of Applied Physics*, 83(10):5025, Feb 1998. [Online]. Available from: http://aip.scitation.org/doi/abs/10.1063/1.367318.

[6] G. Birkl, S. Kassner, and H. Walther. Multiple-shell structures of laser-cooled 24 Mg^+ ions in a quadrupole storage ring. *Nature*, 357(6376):310–313, May 1992. [Online]. Available from: http://www.iap.tu-darmstadt.de/fileadmin/apq/publications/crystals_nature.pdf.

[7] H. Cantor-Cooke. Construction of an agile, controllable radio frequency source. B.Sc. Thesis, College of William and Mary, 2014. [Online]. Available from: https://www.wm.edu/as/physics/documents/seniorstheses/class2014theses/cantor_cooke_h.pdf.

[8] J. I. Cirac and P. Zoller. Quantum computations with cold trapped ions. *Phys. Rev. Lett.*, 74:4091–4094, May 1995. [Online]. Available from: http://link.aps.org/doi/10.1103/PhysRevLett.74.4091.

[9] National Instruments Corporation. *Specification Sheet: NI 6731/6733*. [Online]. Available from: http://www.ni.com/pdf/manuals/371232b.pdf.

[10] B. Cronin. DDS devices generate highquality waveforms simply, efficiently, and flexibly. *Analog Dialogue*, 46, Jan 2012. [Online]. Available from: http://www.analog.com/library/analogdialogue/archives/46-01/DDS_devices.pdf.

[11] G. De Chiara, A. del Campo, G. Morigi, M. B. Plenio, and A. Retzker. Spontaneous nucleation of structural defects in inhomogeneous ion chains. *New Journal of Physics*, 12(11):115003, Nov 2010. [Online]. Available from: http://stacks.iop.org/1367-2630/12/i=11/a=115003.

[12] A. del Campo, G. De Chiara, G. Morigi, M. B. Plenio, and A. Retzker. Structural defects in ion chains by quenching the external potential: The inhomogeneous Kibble-Zurek mechanism. *Phys. Rev. Lett.*, 105:075701, Aug 2010. [Online]. Available from: http://link.aps.org/doi/10.1103/PhysRevLett.105.075701.

[13] Analog Devices. *Evaluation Board User Guide UG-207*. [Online]. Available from: http://www.analog.com/media/en/technical-documentation/user-guides/UG-207.pdf.

[14] Analog Devices. *Specification Sheet: AD9910*. [Online]. Available from: http://www.analog.com/media/en/technical-documentation/data-sheets/AD9910.pdf.

[15] Analog Devices. *Synchronizing Multiple AD9910 1 GSPS Direct Digital Synthesizers*. [Online]. Available from: http://www.analog.com/media/en/reference-design-documentation/reference-designs/CN0121.pdf.

[16] F. Diedrich, E. Peik, J. M. Chen, W. Quint, and H. Walther. Observation of a phase transition of stored laser-cooled ions. *Phys. Rev. Lett.*, 59:2931–2934, Dec 1987. [Online]. Available from: http://link.aps.org/doi/10.1103/PhysRevLett.59.2931.

[17] J. Drees and W. Paul. Beschleunigung von elektronen in einem plasmabetatron. *Zeitschrift für Physik*, 180(4):340–361, Aug 1964. [Online]. Available from: http://dx.doi.org/10.1007/BF01380519.

[18] C. C. Drennan. VME-DDS frequency and phase control module, Jun 2011. [Online]. Available from: http://beamdocs.fnal.gov/AD-public/DocDB/ShowDocument?docid=3891.

[19] D. H. E. Dubin. Theory of structural phase transitions in a trapped coulomb crystal. *Phys. Rev. Lett.*, 71:2753–2756, Oct 1993. [Online]. Available from: http://link.aps.org/doi/10.1103/PhysRevLett.71.2753.

[20] D. H. E. Dubin and T. M. O'Neil. Trapped nonneutral plasmas, liquids, and crystals (the thermal equilibrium states). *Rev. Mod. Phys.*, 71:87–172, Jan 1999. [Online]. Available from: http://link.aps.org/doi/10.1103/RevModPhys.71.87.

[21] S. Ejtemaee. A fluorescence study of single trapped ytterbium ions for quantum information applications. M.Sc. thesis, Simon Fraser University, 2010. [Online]. Available from: http://summit.sfu.ca/item/12155.

[22] S. Ejtemaee. Dynamics of trapped ions near the linear-zigzag structural phase transition. Ph.D. thesis, Simon Fraser University, 2015. [Online]. Available from: http://summit.sfu.ca/item/16248.

[23] S. Ejtemaee and P. C. Haljan. Spontaneous nucleation and dynamics of kink defects in zigzag arrays of trapped ions. *Phys. Rev. A*, 87:051401, May 2013. [Online]. Available from: http://link.aps.org/doi/10.1103/PhysRevA.87.051401.

[24] S. Ejtemaee and P.C. Haljan. 3-D sisyphus cooling of trapped ions. *arXiv preprint in arXiv:1603.01248*, Mar 2016. [Online]. Available from: https://arxiv.org/abs/1603.01248.

[25] D. G. Enzer, M. M. Schauer, J. J. Gomez, M. S. Gulley, M. H. Holzscheiter, P. G. Kwiat, S. K. Lamoreaux, C. G. Peterson, V. D. Sandberg, D. Tupa, A. G. White, R. J. Hughes, and D. F. V. James. Observation of power-law scaling for phase transitions in linear trapped ion crystals. *Phys. Rev. Lett.*, 85:2466–2469, Sep 2000. [Online]. Available from: http://link.aps.org/doi/10.1103/PhysRevLett.85.2466.

[26] S. Fishman, G. De Chiara, T. Calarco, and G. Morigi. Structural phase transitions in low-dimensional ion crystals. *Phys. Rev. B*, 77:064111, Feb 2008. [Online]. Available from: http://link.aps.org/doi/10.1103/PhysRevB.77.064111.

[27] N. Freitas, E. A. Martinez, and J. P. Paz. Heat transport through ion crystals. *arXiv preprint in arXiv:1312.6644v5*, Dec 2015. [Online]. Available from: https://arxiv.org/pdf/1312.6644.pdf.

[28] M. J. Frick. Numerical modelling of ion traps and comparison to experiment. B.Sc. Hon. Thesis, Simon Fraser University, 2016.

[29] Z.-H. Gong, G.-D. Lin, and L.-M. Duan. Temperature-driven structural phase transition for trapped ions and a proposal for its experimental detection. *Phys. Rev. Lett.*, 105:265703, Dec 2010. [Online]. Available from: http://link.aps.org/doi/10.1103/PhysRevLett.105.265703.

[30] W. M. Haynes. *CRC Handbook of Chemistry and Physics*. CRC Press/Taylor and Francis, 97 edition, 2016.

[31] P. R. Hemmer, M. S. Shahriar, V. D. Natoli, and S. Ezekiel. Ac stark shifts in a two-zone raman interaction. *J. Opt. Soc. Am. B*, 6(8):1519–1528, Aug 1989. [Online]. Available from: http://josab.osa.org/abstract.cfm?URI=josab-6-8-1519.

[32] M. Johanning, A. F. VarÃşn, and C. Wunderlich. Quantum simulations with cold trapped ions. *Journal of Physics B: Atomic, Molecular and Optical Physics*, 42(15):154009, Jul 2009. [Online]. Available from: http://stacks.iop.org/0953-4075/42/i=15/a=154009.

[33] K. G. Johnson, J. D. Wong-Campos, A. Restelli, K. A. Landsman, B. Neyenhuis, J. Mizrahi, and C. Monroe. Active stabilization of ion trap radiofrequency potentials. *Review of Scientific Instruments*, 87(5), Apr 2016. [Online]. Available from: http://scitation.aip.org/content/aip/journal/rsi/87/5/10.1063/1.4948734.

[34] M. L. Kidd. Watch out for those thermoelectric voltages! *Metrology 101*, 19(2):18–21, Apr 2012. [Online]. Available from: http://www.callabmag.com/watch-out-for-those-thermoelectric-voltages/.

[35] H. Landa, S. Marcovitch, A. Retzker, M. B. Plenio, and B. Reznik. Quantum coherence of discrete kink solitons in ion traps. *Phys. Rev. Lett.*, 104:043004, Jan 2010. [Online]. Available from: http://link.aps.org/doi/10.1103/PhysRevLett.104.043004.

[36] C. E. Langer. High fidelity quantum information processing with trapped ions. M.Sc. thesis, University of Colorado, 2006. [Online]. Available from: https://www.nist.gov/sites/default/files/documents/pml/div688/grp10/langer_phdthesis.pdf.

[37] J. Ledford. Development of an eight channel waveform generator for beamforming applications. M.Sc. thesis, University of Kansas, 2008. [Online]. Available from: https://kuscholarworks.ku.edu/bitstream/handle/1808/4354/Ledford_ku_0099M_10032_DATA_1.pdf?sequence=1&isAllowed=y.

[38] Z. S. Li, S. Svanberg, P. Quinet, X. Tordoir, and E. Biémont. Lifetime measurements in Yb II with time-resolved laser spectroscopy. *Journal of Physics B: Atomic, Molecular and Optical Physics*, 32(7):1731, Dec 1999. [Online]. Available from: http://stacks.iop.org/0953-4075/32/i=7/a=014.

[39] J. Liang. Unpublished work for ad9959 based synthesizer.

[40] J. Liang and P. C. Haljan. Hopping of an impurity defect in ion crystals in linear traps. *Phys. Rev. A*, 83:063401, Jun 2011. [Online]. Available from: http://link.aps.org/doi/10.1103/PhysRevA.83.063401.

[41] Arduino LLC. Specification sheet: Arduino mega 2560. [Online]. Available from: https://www.arduino.cc/en/Main/ArduinoBoardMega2560.

[42] Photonics Technologies Ltd. Specification sheet: Versatile frequency generator V.F.G. 150, 2015. [Online]. Available from: http://www.photonicstechnologies.com/index.php/versatile-frequency-generator-vfg-150.html.

[43] F. G. Major, V. N. Gheorghe, and G. Werth. *Charged Particle Traps*. Springer Berlin Heidelberg, Berlin, Heidelberg, 2005. [Online]. Available from: http://www.springer.com/gp/book/9783540220435.

[44] M. McAllister and P. Schindler. Haeffner lab DDS controller, Jul 2015. [Online]. Available from: https://github.com/haeffnerlab/dds_controller.

[45] H. J. Metcalf and P. Van der Straten. *Laser cooling and trapping*. Springer, 2002.

[46] M. Mielenz, J. Brox, S. Kahra, G. Leschhorn, M. Albert, T. Schaetz, H. Landa, and B. Reznik. Trapping of topological-structural defects in coulomb crystals. *Phys. Rev. Lett.*, 110:133004, Mar 2013. [Online]. Available from: http://link.aps.org/doi/10.1103/PhysRevLett.110.133004.

[47] A. Mohit. *The art of hardware architecture: design methods and techniques for digital circuits*. Springer, 2012.

[48] E. Mount, D. Gaultney, G. Vrijsen, M. Adams, S. Baek, K. Hudek, L. Isabella, S. Crain, A. van Rynbach, P. Maunz, and et al. Scalable digital hardware for a trapped ion quantum computer. *arXiv in preprint arXiv:1504.00035v3*, pages 1 – 19, Sep 2015. [Online]. Available from: https://arxiv.org/pdf/1504.00035.pdf.

[49] W. Neuhauser, M. Hohenstatt, P. E. Toschek, and H. Dehmelt. Localized visible ba^+ mono-ion oscillator. *Phys. Rev. A*, 22:1137–1140, Sep 1980. [Online]. Available from: http://link.aps.org/doi/10.1103/PhysRevA.22.1137.

[50] S. Olmschenk, K. C. Younge, D. L. Moehring, D. N. Matsukevich, P. Maunz, and C. Monroe. Manipulation and detection of a trapped Yb^+ hyperfine qubit. *Phys. Rev. A*, 76:052314, Nov 2007. [Online]. Available from: http://link.aps.org/doi/10.1103/PhysRevA.76.052314.

[51] C. Ospelkaus, U. Warring, Y. Colombe, K. R. Brown, J. M. Amini, D. Leibfried, and D. J. Wineland. Microwave quantum logic gates for trapped ions. *Nature Letters*, 476:181–184, 2011. [Online]. Available from: http://dx.doi.org/10.1038/nature10290.

[52] P. T. T. Pham. A general-purpose pulse sequencer for quantum computing. M.Sc. thesis, Massachusetts Institute of Technology, 2005. [Online]. Available from: https://dspace.mit.edu/bitstream/handle/1721.1/32106/62367587-mit.pdf?sequence=2.

[53] G. Piacente, I. V. Schweigert, J. J. Betouras, and F. M. Peeters. Generic properties of a quasi-one-dimensional classical wigner crystal. *Phys. Rev. B*, 69:045324, Jan 2004. [Online]. Available from: http://link.aps.org/doi/10.1103/PhysRevB.69.045324.

[54] M. B. Plenio and A. Retzker. Ion traps as a testbed of classical and quantum statistical mechanics. *Annalen der Physik*, 525(10-11):A159–A162, Nov 2013. [Online]. Available from: http://dx.doi.org/10.1002/andp.201300740.

[55] J. D. Prestage, G. J. Dick, and L. Maleki. New ion trap for frequency standard applications. *Journal of Applied Physics*, 66(3):1013, Apr 1989. [Online]. Available from: http://aip.scitation.org/doi/abs/10.1063/1.343486.

[56] K. Pyka, J. Keller, H. L. Partner, R. Nigmatullin, T. Burgermeister, D. M. Meier, K. Kuhlmann, A. Retzker, M. B. Plenio, W. H. Zurek, A. del Campo, and T. E. Mehlstaubler. Topological defect formation and spontaneous symmetry breaking in ion coulomb crystals. *Nature Communications*, 4, Aug 2013. [Online]. Available from: http://www.nature.com/articles/ncomms3291.

[57] M. G. Raizen, J. M. Gilligan, J. C. Bergquist, W. M. Itano, and D. J. Wineland. Ionic crystals in a linear paul trap. *Phys. Rev. A*, 45:6493–6501, May 1992. [Online]. Available from: http://link.aps.org/doi/10.1103/PhysRevA.45.6493.

[58] N. F. Ramsey. Experiments with separated oscillatory fields and hydrogen masers. *Rev. Mod. Phys.*, 62:541–552, Jul 1990. [Online]. Available from: http://link.aps.org/doi/10.1103/RevModPhys.62.541.

[59] A. Retzker, R. C. Thompson, D. M. Segal, and M. B. Plenio. Double well potentials and quantum phase transitions in ion traps. *Phys. Rev. Lett.*, 101:260504, Dec 2008. [Online]. Available from: http://link.aps.org/doi/10.1103/PhysRevLett.101.260504.

[60] A. Ruiz, D. Alonso, M. B. Plenio, and A. del Campo. Tuning heat transport in trapped-ion chains across a structural phase transition. *Phys. Rev. B*, 89:214305, Jun 2014. [Online]. Available from: http://link.aps.org/doi/10.1103/PhysRevB.89.214305.

[61] J. P. Schiffer. Phase transitions in anisotropically confined ionic crystals. *Phys. Rev. Lett.*, 70:818–821, Feb 1993. [Online]. Available from: http://link.aps.org/doi/10.1103/PhysRevLett.70.818.

[62] P. Schindler. Frequency synthesis and pulse shaping for quantum information processing with trapped ions. M.S.c thesis, University of Innsbruck, 2008. [Online]. Available from: http://www.quantumoptics.at/images/publications/diploma/diplom_schindler.pdf.

[63] R. Schmied, T Roscilde, V. Murg, D Porras, and J. I. Cirac. Quantum phases of trapped ions in an optical lattice. *New Journal of Physics*, 10(4):045017, Apr 2008. [Online]. Available from: http://stacks.iop.org/1367-2630/10/i=4/a=045017.

[64] E. Shimshoni, G. Morigi, and S. Fishman. Quantum zigzag transition in ion chains. *Phys. Rev. Lett.*, 106:010401, Jan 2011. [Online]. Available from: http://link.aps.org/doi/10.1103/PhysRevLett.106.010401.

[65] P. Silvi, G. De Chiara, T. Calarco, G. Morigi, and S. Montangero. Full characterization of the quantum linear-zigzag transition in atomic chains. *Annalen der Physik*, 525(10-11):827–832, Jul 2013. [Online]. Available from: http://dx.doi.org/10.1002/andp.201300090.

[66] J. D. Siverns, L. R. Simkins, S. Weidt, and W. K. Hensinger. On the application of radio frequency voltages to ion traps via helical resonators. *Applied Physics B*, 107(4):921–934, 2012. [Online]. Available from: http://dx.doi.org/10.1007/s00340-011-4837-0.

[67] Agilent Technologies. *Specification Sheet: Agilent E361XA 30W Bench Series DC Power Supplies.* [Online]. Available from: http://sites.fas.harvard.edu/~phys191r/Bench_Notes/A1/agilent_e3610a.pdf.

[68] N. Timoney, I. Baumgart, M. Johanning, A. F. Varón, M. B. Plenio, A. Retzker, and Ch. Wunderlich. Quantum gates and memory using microwave-dressed states. *Nature Letters*, 476:185–188, 2011. [Online]. Available from: http://dx.doi.org/10.1038/nature10319.

[69] Q. A. Turchette, C. J. Myatt, B. E. King, C. A. Sackett, D. Kielpinski, W. M. Itano, C. Monroe, and D. J. Wineland. Decoherence and decay of motional quantum states of a trapped atom coupled to engineered reservoirs. *Phys. Rev. A*, 62:053807, Oct 2000. [Online]. Available from: http://link.aps.org/doi/10.1103/PhysRevA.62.053807.

[70] Analog Devices Tutorials. Fundamentals of direct digital synthesis (DDS). [Online]. Available from: http://www.analog.com/media/en/training-seminars/tutorials/MT-085.pdf.

[71] S. Ulm, J. Robnagel, G. Jacob, C. Degunther, S. T. Dawkins, U. G. Poschinger, R. Nigmatullin, A Retzker, M. B. Plenio, F. Schmidt-Kaler, and K. Singer. Observation of the Kibble−Zurek scaling law for defect formation in ion crystals. *Nature Communications*, 4, Aug 2013. [Online]. Available from: http://www.nature.com/articles/ncomms3290.

[72] H. Walther. From a single ion to a mesoscopic system - crystallization of ions in paul traps. *Physica Scripta*, 1995(T59):360, Jan 1995. [Online]. Available from: http://stacks.iop.org/1402-4896/1995/i=T59/a=049.

[73] G. Werth, V. N. Gheorghe, and F. G. Major. *Charged Particle Traps II.* Springer Berlin Heidelberg, Berlin, Heidelberg, 2009. [Online]. Available from: http://www.springer.com/gp/book/9783540922605.

[74] D. J. Wineland, J. C. Bergquist, Wayne M. Itano, J. J. Bollinger, and C. H. Manney. Atomic-ion coulomb clusters in an ion trap. *Phys. Rev. Lett.*, 59:2935–2938, Dec 1987. [Online]. Available from: http://link.aps.org/doi/10.1103/PhysRevLett.59.2935.

[75] D. J. Wineland, C. Monroe, W. M. Itano, D. Leibfried, B. E. King, and D. M. Meekhof. Experimental issues in coherent quantum-state manipulation of trapped atomic ions. *J. Res. Natl. Inst. Stand. Technol. Journal of Research of the National Institute of Standards and Technology*, 103(3):259, May 1998. [Online]. Available from: http://tf.boulder.nist.gov/general/pdf/1275.pdf.

[76] W. Wolfgang. Specification sheet: Flexible multi-channel phase-coherent RF source, 2011. [Online]. Available from: http://www.wieserlabs.com/prod/e/rf/flexdds/WL-FlexDDS-docu-r2c.pdf.

[77] J. Zhang. Ph.D. thesis in preparation.